Navigation Analysis and Design for Mars Entry

by

Rudy Avi Boehmer

B.S. Aerospace Engineering
The University of Arizona, 1996

Submitted to the Department of Aeronautics and Astronautics in
partial fulfillment of the requirements for the degree of

Master of Science in Aeronautics and Astronautics

at the

MASSACHUSETTS INSTITUTE OF TECHNOLOGY

February 1999

Signature of Author .....
Department of Aeronautics and Astronautics
October 1998

Certified by .....
Professor John J. Deyst, Jr.
Department of Aeronautics and Astronautics
Thesis Supervisor

Accepted by .....
Jaime Peraire
Department of Aeronautics and Astronautics
Chair, Graduate Office

Navigation Analysis and Design for Mars Entry

by

Rudy Avi Boehmer

Submitted to the Department of Aeronautics and Astronautics on
October 20, 1998, in partial fulfillment of the requirements for the
degree of Master of Science in Aeronautics and Astronautics

Abstract

This thesis presents a navigation system design for a lander module during entry at Mars. The system estimates the state vector with an extended Kalman filter, which utilizes update information provided by the following measurement types: two-way range with orbiting satellites, two-way Doppler with orbiting satellites, two-way range with surface beacons, two-way Doppler with surface beacons, altitude, and relative surface velocity.

Filter performance of the navigation design is analyzed using a computer simulation of such a spacecraft during Mars entry. Simulation results are presented to evaluate the effectiveness of the filter using each of the individual measurement types. In addition, the sequence in which the measurements are filtered that yields the most favourable results is determined. Using this optimal sequence, the simulation produces a final standard deviation of 105.25 m for the lander position and 0.168 m/s for the lander velocity, compared to final standard deviations of 1218.85 m and 3.700 m/s for a case where no measurements are processed.

Thesis Supervisor: John J. Deyst, Jr.
Title: Professor, Department of Aeronautics and Astronautics

Acknowledgments

I would like to thank the people who have helped to make this thesis possible and who have made my days at MIT and in the Boston/Cambridge area so rewarding. I hope I will never forget the incredible time I spent here.

First of all, I would like to thank my thesis advisor, Professor John Deyst, for the guidance and support without which I could never have completed this research. I would also like to thank the Draper Laboratory, especially Christopher D'Souza and Peter Neirinckx, for providing me the opportunity to come to MIT and to pursue this area of research. I will always appreciate the knowledge and guidance I received at the CSDL as well as the introduction to the field of navigation and estimation.

A shout out to the guys (and DLF's) who made these two years such a blast with their crazy and kooky shenanigans: Tony, Simon, Miguel, Chris, Beau, Gordon, Ted, Varun, George, Ben, Chad, Ramses, Cory, Dave, Andy, Steve, Mike, Matt, Ed, Nhut, Pat et al. To the Hurley St. crew, Simon and Miguel, who over the course of a year became from roommates to friends, une verre de cava vers l'avenir! À Simon, mes felicitations pour ton marriage. À Miguel, bonne chance à ton recherche d'un bon travail. To Tony, where would I begin? You'll have to come to LA, then we'll do the lunch thing and talk about starting that 5th floor dance hall. To Chris, fellow Wildcat! There is only one way to settle this Kentucky vs. Arizona debate and that is in a no-holds-barred cage match. I'll see you there. To all the guys, I just want to say that it was fun and hopefully will be again sometime in the future.

The most important thanks must go to my family: my parents, Ahron and Nessia, my sisters, Karen and Sharon, and my grandmother Hanna. Even though you were on the other side of the country, your support, faith, and understanding always seemed near. I hope you got to enjoy the "hub of the universe" while you were here and I will see you all really soon! Toda raba.

This thesis will self-destruct when the Vancouver Canucks win the Stanley Cup.

Table of Contents

List of Figures

List of Tables

Chapter 1

Introduction

1.1 Background

With the success of the recent Pathfinder mission to Mars, there is much renewed interest in the exploration of the Red Planet. In addition, it is intriguing to envision the possibilities of a future manned mission to Mars. Such a mission would indeed present numerous technological obstacles to overcome, such as trajectory design and autonomous navigation. Furthermore, these obstacles would be existent in all mission phases, which include take-off from Earth, interplanetary orbit from Earth to Mars (or cruise phase), entry into the Mars atmosphere, landing on the planet surface, and the eventual return back to Earth.

1.2 Objectives

During the entry phase of the mission studied here, the lander module must undergo an appropriate transition from orbital cruise to the proper state in preparation for the landing phase. This phase is particularly significant since it is here where the spacecraft first encounters the planet Mars, as well as its gravity and atmosphere. Considering that it is continually susceptible to perturbations, tracking the lander during the entry phase can be a daunting task. In dealing with a manned mission, the presence of an effective autonomous navigation scheme on board the lander is extremely significant.

The primary objective of this research is to design and analyze an on-board navigation system for a lander module during Mars entry. This system will be responsible for accurately estimating a number of variables, including the lander position and velocity, in the presence of various uncertainties. These uncertainties can include initial perturbations in

the position and velocity estimates as well as any biases and noises that may exist in system models. The main elements of the navigation scheme are a number of on-board sensors and an on-board Kalman filter. These sensors take a variety of measurements, which are then individually processed in the filter to produce improved state estimates.

1.2.1 Previous Research

Past concepts and designs for Mars entry navigation using external measurements with a Kalman filter have been analyzed and discussed in a number of papers.

Reference [9] details one such navigation analysis for Mars entry and landing. This design, planned by the European Space Agency (ESA), is to be purely autonomous, i.e. it will contain no external guidance. The most relevant concept to this thesis is that range and Doppler measurements are taken from the lander module to a series of beacons located on the surface of Mars. These measurements will then be processed in a Kalman filter to estimate the state.

A similar design for Mars entry navigation is presented in [17]. Range and Doppler measurements are again taken with surface beacons, as well as with a network of communication satellites in orbit. Of course, the navigation systems in both papers assume that such a series of satellites and surface beacons at Mars have already been arranged during prior missions.

These two navigation schemes are quite different compared to the approach presented in [16]. This paper discusses trajectory analysis for the Mars Pathfinder at Mars atmospheric entry, descent, and landing. Though this design does not use a Kalman filter with any external measurements, it is representative of a scheme that has been applied in practicality and actually sent to Mars.

1.2.2 Navigation Design

This navigation system for Mars entry incorporates an assumed conglomeration of orbiting satellites and surface beacons previously put into place. In addition, it incorporates four on-board sensors: two-way range radio, two-way Doppler radio, radar altimeter, and surface radar velocimeter. The two-way range will take range measurements from the lander module to each of the satellites and beacons, provided they are within sight. The two-way Doppler will take delta-range measurements with the same satellites and beacons. The altitude of the lander with respect to the Martian surface directly below is determined by the radar altimeter. The surface radar velocimeter takes velocity measurements of the lander relative to the surface. These measurements will be processed by the Kalman filter in such a sequence as to provide the most nearly optimal results. This sequence will be determined empirically.

The system will be responsible for the estimation of a number of states. These state variables include the positions and velocities of the lander and of all satellites and beacons. The system also accounts for various biases, drifts, and misalignments of the sensors, as well as of the inertial measurement unit (IMU), which consists of on-board gyroscopes and accelerometers.

1.3 Thesis Overview

The complete design and analysis of the proposed navigation algorithm contained in this thesis is partitioned into the following chapters as follows:

Chapter 2, "Navigation System Design," presents the models in the navigation system design. The filter states are defined, and all state and state error dynamics models are described in detail. The algorithm of the extended Kalman filter (EKF) is also described, in addition to all measurement models that will be used.

Chapter 3, "Simulation Description," describes the computer simulation used to evaluate the proposed navigation system. The complete flow of the program algorithm is discussed, and all initial conditions and constants used in the simulation are presented.

Chapter 4, "Covariance Analysis," presents and discusses the filter performance results of the navigation algorithm. This is done for a series of measurement profiles, each of which represents an individual measurement type. The measurement types are then sequenced to determine the most favourable results. Nominal trajectories of the lander and all satellites and beacons are also displayed.

Chapter 5, "Conclusion," summarizes the results of this research and provides suggestions for future analysis in this topic.

Chapter 2

Navigation System Design

2.1 Introduction

This chapter describes the proposed navigation system for a Mars entry. The first section of this chapter details the algorithm of the extended Kalman filter (EKF), which performs the estimation in this design based on a series of measurements. The filter states are then defined, in addition to the state dynamics model, for the purpose of state propagation. The next section details the dynamics required for covariance propagation, in particular the system dynamics matrix and the various error or disturbance statistics. The last section describes the models of the four measurement types used in this filter.

2.2 Filter Description

The Kalman filter is an algorithm to calculate the minimum variance estimate of a vector of time-variant system states, $\underline{x}(t)$, using state-dependent measurements to update the state estimate. However, the standard Kalman filter requires a linear system. For this proposed system, while the state dynamics can be properly linearized, the models for the measurements will be nonlinear. Therefore, the extended Kalman filter will be used as it has the ability to deal with nonlinear measurement models, as well as nonlinear dynamics.

2.2.1 State and Covariance Propagation

First, the state process and measurement models of the system will be defined. The state process model consists of continuous nonlinear dynamics:

$$\dot{\underline{x}}(t) = \underline{f}(\underline{x}(t), t) + \underline{g}(\underline{x}(t), t)\underline{w}(t) \tag{2.1}$$

while the discrete nonlinear measurement model is:

$$\underline{z}_k = \underline{h}(\underline{x}(t_k), t_k) + \underline{v}_k . \tag{2.2}$$

$\underline{f}(\underline{x}(t), t)$ and $\underline{g}(\underline{x}(t), t)$ represent the model of the state dynamics while $\underline{h}(\underline{x}(t_k), t_k)$ models the measurement dynamics. Noises are represented by $\underline{w}(t)$ and $\underline{v}_k$. The white process noise $\underline{w}(t)$ is zero mean and has an intensity denoted by $\underline{Q}(t)$ (which is also known as the power spectral density). The noise covariance is defined as:

$$E[\underline{w}(t)\underline{w}^T(\tau)] = \underline{Q}(t)\delta(t-\tau) \tag{2.3}$$

where $\delta(t)$ is the Dirac delta function. The discrete measurement noise $\underline{v}_k$ is also zero mean and has an intensity denoted by the discrete matrix $\underline{R}_k$ (which is known as the measurement covariance):

$$E[\underline{v}_k \underline{v}_k^T] = \underline{R}_k . \tag{2.4}$$

In addition, the two noise vectors are assumed to have no cross correlation:

$$E[\underline{w}(t)\underline{v}_k^T] = \underline{0} . \tag{2.5}$$

Additionally, the error covariance matrix $\underline{P}(t)$ of the state provides a description of the errors in the estimation of the state. One important aspect of the covariance matrix is that the square root of its $n^{\underline{th}}$ diagonal entry represents the standard deviation of the $n^{\underline{th}}$ state variable. If the true reference state vector is defined as $\underline{x}(t)$ and the filter estimated state as $\hat{\underline{x}}(t)$, this covariance matrix is defined as:

$$\underline{P}(t) = E[\tilde{\underline{x}}(t)\tilde{\underline{x}}^T(t)] \tag{2.6}$$

where the estimation error $\tilde{\underline{x}}(t)$ is:

$$\tilde{\underline{x}}(t) = \underline{x}(t) - \hat{\underline{x}}(t) \tag{2.7}$$

With state and covariance models in first-order continuous differential form, a standard fourth-order Runge-Kutta algorithm is used to propagate the state estimate and cova-

riance, given initial conditions for both. Indeed, the state model is already of this form in Equation 2.1. For the covariance matrix, such a dynamics model looks like:

$$\dot{\underline{P}}(t) = \underline{F}(\hat{\underline{x}}(t), t)\underline{P}(t) + \underline{P}(t)\underline{F}^T(\hat{\underline{x}}(t), t) + \underline{Q}(t) \tag{2.8}$$

where the linearized system dynamics matrix $\underline{F}(\hat{\underline{x}}(t), t)$ is defined as:

$$\underline{F}(\hat{\underline{x}}(t), t) = \left.\frac{\partial \underline{f}(\underline{x}(t), t)}{\partial \underline{x}(t)}\right|_{\underline{x}(t) = \hat{\underline{x}}(t)}. \tag{2.9}$$

The system dynamics matrix is also used to create a first-order continuous differential model of the error estimate:

$$\dot{\tilde{\underline{x}}}(t) = \underline{F}(t)\tilde{\underline{x}}(t) + \underline{G}_x(t)\underline{w}(t) \tag{2.10}$$

where

$$\underline{G}_x(t) = \left.\frac{\partial \underline{g}(\underline{x}(t), t)}{\partial \underline{x}(t)}\right|_{\underline{x}(t) = \hat{\underline{x}}(t)}. \tag{2.11}$$

This development is discussed in further detail in Section 2.4 along with the power spectral density matrix $\underline{Q}(t)$. [7]

2.2.2 State and Covariance Update

Once the state estimate and covariance have been propagated for a time step, they are ready to be updated by incorporating measurements taken at that time step. For the sake of notation, it should be mentioned that the estimated state before and after the filter update are denoted as $\hat{\underline{x}}^-$ and $\hat{\underline{x}}^+$, respectively, while the covariance before and after the filter update are $\underline{P}^-$ and $\underline{P}^+$, respectively.

The measurement $\underline{z}_k$ (representative of the actual measurement taken from the spacecraft sensors) at time t_k can be created using the measurement model in Equation 2.2 with the true state. This is necessary to calculate the updated state estimate as follows:

$$\hat{\underline{x}}_k^+ = \hat{\underline{x}}_k^- + \underline{K}_k(\underline{z}_k - \underline{h}(\hat{\underline{x}}_k^-(t_k), t_k)). \tag{2.12}$$

where the Kalman gain matrix $\underline{K}_k$ is:

$$\underline{K}_k = \underline{P}_k^- \underline{H}_k^T(\hat{\underline{x}}_k^-)[\underline{H}_k(\hat{\underline{x}}_k^-)\underline{P}_k^- \underline{H}_k^T(\hat{\underline{x}}_k^-) + \underline{R}_k]^{-1} \tag{2.13}$$

which uses the measurement sensitivity matrix $\underline{H}_k$ [14]:

$$\underline{H}_k(\hat{\underline{x}}_k^-) = \left.\frac{\partial \underline{h}(\underline{x}(t_k))}{\partial \underline{x}(t_k)}\right|_{\underline{x}(t_k) = \hat{\underline{x}}_k^-} \tag{2.14}$$

In addition, this filter uses the Joseph form of the covariance update to preserve the symmetry and ensure the positive definiteness of the covariance matrix [7]. The Joseph form looks like:

$$\underline{P}_k^+ = (\underline{I} - \underline{K}_k\underline{H}_k)\underline{P}_k(\underline{I} - \underline{K}_k\underline{H}_k)^T + \underline{K}_k\underline{R}_k\underline{K}_k. \tag{2.15}$$

2.3 State Variables and Dynamics

An analysis of the states that comprise $\underline{x}(t)$ for this system is presented. In brief, these states must account for the dynamics of all spacecraft involved with the navigation as well as the various biases in the sensors that may contaminate the measurements.

2.3.1 Lander States

The dynamics of the lander involve six states: lander position and velocity in three dimensions. The simulation uses an almost inertial (or Mars-centered, with the origin placed at the center of Mars) coordinate system. The dynamics are described as:

$$\frac{d\underline{R}_L}{dt} = \underline{V}_L \tag{2.16}$$

$$\frac{d\underline{V}_L}{dt} = \underline{g}_M + \underline{a}_c + \underline{b}_a \tag{2.17}$$

where $\underline{g}_M$ is the Martian gravitational acceleration and $\underline{a}_c$ is non-gravitational acceleration (commanded thrust, atmospheric drag). The accelerometer bias $\underline{b}_a$ is introduced to the lander state model from the IMU state model (Section 2.3.4) to simulate unmodeled lander

dynamics. Additionally, the gravitational force, including J_2 and J_3 contributions, can be described as: [12]

$$\underline{g}_M = -\begin{bmatrix} \frac{\mu_M x}{|\underline{R}_L|^3}\left\{1+\frac{3J_2}{2}\left(\frac{R_{eq}}{|\underline{R}_L|}\right)^2\left[1-5\left(\frac{z}{|\underline{R}_L|}\right)^2\right]+\frac{5J_3}{2}\left(\frac{R_{eq}}{|\underline{R}_L|}\right)^3\left(\frac{z}{|\underline{R}_L|}\right)\left[3-7\left(\frac{z}{|\underline{R}_L|}\right)^2\right]\right\} \\ \frac{\mu_M y}{|\underline{R}_L|^3}\left\{1+\frac{3J_2}{2}\left(\frac{R_{eq}}{|\underline{R}_L|}\right)^2\left[1-5\left(\frac{z}{|\underline{R}_L|}\right)^2\right]+\frac{5J_3}{2}\left(\frac{R_{eq}}{|\underline{R}_L|}\right)^3\left(\frac{z}{|\underline{R}_L|}\right)\left[3-7\left(\frac{z}{|\underline{R}_L|}\right)^2\right]\right\} \\ \frac{\mu_M z}{|\underline{R}_L|^3}\left\{1+\frac{3J_2}{2}\left(\frac{R_{eq}}{|\underline{R}_L|}\right)^2\left[1-5\left(\frac{z}{|\underline{R}_L|}\right)^2\right]\right\}+\frac{\mu_M J_3}{2}\left(\frac{R_{eq}}{|\underline{R}_L|}\right)^3\left\{30\left(\frac{z}{|\underline{R}_L|}\right)-35\left(\frac{z}{|\underline{R}_L|}\right)^4+3\right\} \end{bmatrix} \tag{2.18}$$

where μ_M, R_{eq}, J_2, and J_3 are constants and $|\underline{R}_L|$ is the magnitude of the lander position vector. [12]

2.3.2 Navigation Satellite States

A number of navigation satellites will be assumed to be in orbit around Mars for the lander to take range and Doppler measurements from. Thus, the motion of these satellites, which will be based on gravitational force, must be accounted for. For a satellite, this model will look like such [3]

$$\frac{d\underline{R}_S}{dt} = \underline{V}_S \tag{2.19}$$

$$\frac{d\underline{V}_S}{dt} = \frac{\mu_M}{|\underline{R}_S|^3}\underline{R}_S. \tag{2.20}$$

These dynamics are repeated for each satellite in use.

2.3.3 Navigation Surface Beacon States

Surface beacons can also be used to take range and Doppler measurements. These beacons are assumed to be stationary on the surface of Mars, so the actual motion described by the dynamics model is in fact governed by the purely rotational motion of the planet Mars. The position $\underline{R}_{Bj}$, at time t_j, given a position $\underline{R}_{Bi}$ at some time t_i, is [3]

$$\underline{R}_{Bj} = \underline{R}_{Bi} + (\sin\alpha)\underline{i}_P \times \underline{R}_{Bi} + (1-\cos\alpha)\underline{i}_P \times (\underline{i}_P \times \underline{R}_{Bi}) \tag{2.21}$$

where the angle of rotation α is defined as

$$\alpha = \left|\underline{\omega}_M\right|(t_j - t_i). \tag{2.22}$$

$\underline{\omega}_M$ is the assumed rotational rate of Mars, and $\underline{i}_P$ is a unit vector in the direction of the planetary pole, or more simply, the axis of planetary rotation.

As the coordinate system in use is Mars-centered, the velocity of the beacon is purely rotational. Velocity is determined by:

$$\underline{V}_{Bj} = \underline{\omega}_M \times \underline{R}_{Bj}. \tag{2.23}$$

Since the planetary rotational rate of Mars is assumed to be constant, the velocity at any time step can always be determined from the position at the same time step. Therefore, the velocity does not need to be estimated and thus, each beacon in use requires three states for the position in the three dimensions. A complete beacon position and velocity profile can be obtained by calculating the beacon position of a time step from the position of the previous time step and repeating this for all time steps. The beacon states are the only set of states to use this analytical propagation scheme rather than numerical integration. In addition, there is no process noise added to the beacon states in the simulation.

2.3.4 Inertial Measurement Unit States

The on-board inertial measurement unit (IMU) consists of three gyroscopes and three accelerometers. Each gyroscope measures the angular rate about an axis (the three axes are orthogonal to comprise a coordinate system) while the accelerometers measure the specific force components along these axes [6]. Six states are needed to account for the three-dimensional misalignment bias $\underline{b}_g$, and drift $\underline{d}_g$, of the gyroscopes and another three states are used to estimate biases $\underline{b}_a$ in the accelerometers. As will be the case with most of the sensor bias states, these IMU states will be modeled as exponentially correlated random processes. In addition, since the gyroscope bias represents a position misalignment

and the gyroscope drift is a velocity misalignment, the drift can be assigned as the time derivative of the gyroscope bias. Thus, the time derivatives become:

$$\frac{d}{dt}\underline{b}_g = \underline{d}_g \tag{2.24}$$

$$\frac{d}{dt}\underline{d}_g = -\beta_g \underline{d}_g + \underline{w}_g \tag{2.25}$$

$$\frac{d}{dt}\underline{b}_a = -\beta_a \underline{b}_a + \underline{w}_a \tag{2.26}$$

with β_g and β_a denoting the inverse time constants associated with the dynamics of the gyroscopes and accelerometers and $\underline{w}_g$ and $\underline{w}_a$ representing the process noises of the gyroscopes and accelerometers.

The type of exponentially correlated random process (ECRV) shown in Equations 2.25 and 2.26 is called a first-order Markov process (FOMP) [15]. Most other bias states will be first-order Markov processes and will have similar state dynamics.

2.3.5 Two-Way Range States

The lander should have the capability to take range (distance) measurements from each of the orbiting satellites and surface beacons. Therefore, the lander will have an associated range bias which represents possible errors in the range measurements due to the sensors. In addition, because this range measurement is two-way, all satellites and beacons that will be used for taking measurements will also have a range bias. The range bias will be represented as b_ρ in the state and is also modeled as a first-order Markov process, like the IMU states. With the inverse time constant β_ρ associated with the range exponential correlation and the range process noise w_ρ, the range dynamics become:

$$\frac{d}{dt}b_\rho = -\beta_\rho b_\rho + w_\rho . \tag{2.27}$$

2.3.6 Two-Way Doppler States

The lander can also use these orbiting satellites and surface beacons to take Doppler measurements, i.e. the rate of change of the distance between the lander and a satellite or beacon. The Doppler measurement can also be viewed as the velocity of the lander relative to the satellite or beacon. The lander, as well as all satellites and beacons, will have a Doppler bias, b_d, that identifies possible errors in the measurement due to the instrumentation. The Doppler bias is modeled as a first-order Markov process and its state dynamics are:

$$\frac{d}{dt}b_d = -\beta_d b_d + w_d \tag{2.28}$$

where β_d is the inverse time constant associated with the Doppler process dynamics and w_d is the Doppler process noise.

2.3.7 Radar Altimeter States

The radar altimeter, which takes altitude measurements, utilizes five states to account for associated biases and misalignments. The radar altimeter bias, b_H, accounts for errors in the one-dimensional altitude measurement readings while the altimeter terrain first-order Markov process bias, b_{FOMP}, represents errors in the vertical terrain models approximated via a first-order Markov process. These biases require one state apiece. The three-dimensional terrain plane misalignment, $\underline{b}_{TP}$, takes up three states and represents uncertainties in the surface slope directly below the lander as well as in the altitude. This misalignment is in local (or LVLH: local vertical/local horizontal) coordinates and will modeled as a constant in all three dimensions, unlike the other two bias states, which will be modeled as first-order Markov processes. The dynamics of these five states are:

$$\frac{d}{dt}b_H = -\beta_H b_H + w_H \tag{2.29}$$

$$\frac{d}{dt}b_{FOMP} = -\beta^* b_{FOMP} + w_{FOMP} \tag{2.30}$$

$$\frac{d}{dt}\underline{b}_{TP} = \underline{0}_{3\times 1} \tag{2.31}$$

where β_H is the inverse time constant associated with the dynamics of the altimeter bias and β^*, accounting for angular momentum in the planetary rotation, is defined as [12]:

$$\beta^* = \beta_{FOMP} R_{eq} \left| \frac{\underline{R}_L \times (\underline{V}_L - \underline{\omega}_M \times \underline{R}_L)}{\underline{R}_L \cdot \underline{R}_L} \right|. \tag{2.32}$$

β_{FOMP} is a correlation distance associated with the altimeter and $\underline{\omega}_M$ is the planetary rotational rate of Mars. In addition, w_H and w_{FOMP} represent the respective altimeter bias and terrain FOMP bias process noises.

2.3.8 Surface Radar Velocimeter States

The surface radar velocimeter measures the velocity of the lander with respect to the surface of Mars. The surface radar velocimeter bias, $\underline{b}_{SR}$, represents the errors in the three-dimensional velocity measurement readings and takes up three states. In addition, since the measurement is taken in a different coordinate system than the one referenced by the lander (local rather than inertial), the misalignment between the two coordinate systems must be considered. This can be accomplished with the gyroscope misalignment bias (from the IMU states) and a velocimeter misalignment bias, $\underline{b}_{mSR}$, which requires another three states. Thus, the surface radar velocimeter requires six states in all. Modeled as first-order Markov processes, the dynamics of these states are:

$$\frac{d}{dt}\underline{b}_{SR} = -\beta_{SR}\underline{b}_{SR} + \underline{w}_{SR} \tag{2.33}$$

$$\frac{d}{dt}\underline{b}_{mSR} = -\beta_{mSR}\underline{b}_{mSR} + \underline{w}_{mSR}. \tag{2.34}$$

The inverse time constants associated with the dynamics of the velocimeter bias and the misalignment bias are β_{SR} and β_{mSR} while the velocimeter bias and misalignment bias process noises are denoted as $\underline{w}_{SR}$ and $\underline{w}_{mSR}$.

2.4 Covariance Dynamics

To propagate the covariance matrix over time, a model of the state error dynamics will be necessary. This is the system dynamics matrix $\underline{F}$ mentioned in the filter design. In addition, the power spectral density matrix $\underline{Q}$, which accounts for errors in the modeling of the state dynamics, is also essential for covariance propagation. Since there is limited cross-correlation in the dynamics between each set of states (i.e. lander states, beacon states, IMU states) in these two matrices, it is possible to calculate sub-matrices for each set of states that are incorporated into the $\underline{F}$ and $\underline{Q}$ matrices when the sets are incorporated into the full state.

2.4.1 Lander Covariance

The system dynamics matrix can be calculated from the derivatives of the state dynamics with respect to the state (Equation 2.9). Thus, the system dynamics sub-matrix $\underline{F}_L$ for the lander position and velocity errors is:

$$\underline{F}_L = \begin{bmatrix} \underline{0}_{3\times 3} & \underline{I}_{3\times 3} \\ \underline{G}(\underline{R}_L) & \underline{0}_{3\times 3} \end{bmatrix} \tag{2.35}$$

where $\underline{G}$ is a matrix of dimension 3x3 and is a function of the lander position [3]:

$$\underline{G}(\underline{R}_L) = \frac{\mu_M}{|\underline{R}_L|^5}(3\underline{R}_L\underline{R}_L^T - |\underline{R}_L|^2\underline{I}_{3\times 3}). \tag{2.36}$$

In addition, the accelerometer bias must be taken into account. Thus, the system dynamics submatrix can be expanded to include this state:

$$\underline{F}_{L/a} = \begin{bmatrix} \underline{F}_L & \begin{bmatrix} \underline{a}_c \times \\ \underline{I}_{3x3} \end{bmatrix} \\ \underline{0}_{3\times 6} & \underline{F}_a \end{bmatrix} \tag{2.37}$$

where $\underline{a}_c \times$ is a cross product operator that also takes the form of a skew-symmetric matrix:

$$\underline{a}_c \times = \begin{bmatrix} a_{cx} \\ a_{cy} \\ a_{cz} \end{bmatrix} \times = \begin{bmatrix} 0 & -a_{cz} & a_{cx} \\ a_{cz} & 0 & -a_{cy} \\ -a_{cy} & a_{cx} & 0 \end{bmatrix} \tag{2.38}$$

Since only the accelerometer bias has process noise, the power spectral density sub-matrix $\underline{Q}_L$ is a 6x6 dimensional zero matrix:

$$\underline{Q}_L = \underline{0}_{6\times 6} \tag{2.39}$$

2.4.2 Navigation Satellite Covariance

Since the motion of the navigation satellites is governed by similar gravitational laws as the motion of the lander (with the exception of J_2 and J_3 contributions), the following set of dynamics can be used for satellite system dynamics sub-matrix:

$$\underline{F}_S = \begin{bmatrix} \underline{0}_{3\times 3} & \underline{I}_{3\times 3} \\ \underline{G}(\underline{R}_S) & \underline{0}_{3\times 3} \end{bmatrix} \tag{2.40}$$

where the 3x3 matrix $\underline{G}$ is described in Equation 2.36. Likewise, the power spectral density sub-matrix $\underline{Q}_S$ is also a 6x6 dimensional zero matrix, as in Equation 2.39.

2.4.3 Navigation Surface Beacon Covariance

Since the surface beacon states are not propagated through integration like the other states, the error analysis of these states must be dealt with differently. In this case, it is assumed that the initial covariance sub-matrix of these states, and thus the knowledge of the errors in these states, does not change with the time propagation. In addition, a power spectral density sub-matrix does not exist for the beacon states, as there is no process noise associated with the beacon state dynamics.

2.4.4 Inertial Measurement Unit Covariance

Since the gyroscope drift is modeled as a first-order Markov process, the system dynamics sub-matrix of the gyroscope drift looks like:

$$\underline{F}_g = -\beta_g \underline{I}_{3\times 3}. \tag{2.41}$$

The accelerometer bias error is also a first-order Markov process, so after taking all the proper derivatives, the complete system dynamics sub-matrix of the IMU states becomes:

$$\underline{F}_{IMU} = \begin{bmatrix} \underline{0}_{3\times 3} & \underline{I}_{3\times 3} & \underline{0}_{3\times 3} \\ \underline{0}_{3\times 3} & -\beta_g \underline{I}_{3\times 3} & \underline{0}_{3\times 3} \\ \underline{0}_{3\times 3} & \underline{0}_{3\times 3} & -\beta_a \underline{I}_{3\times 3} \end{bmatrix}. \tag{2.42}$$

To model uncertainties in the dynamics, the gyroscope and accelerometer have power spectral density sub-matrices $\underline{Q}_g$ and $\underline{Q}_a$, respectively. The gyroscope dynamics are dependent on the drift states so the 3x3 PSD matrix enters in these states. The accelerometer PSD is also of dimension 3x3. [12]

With the initial standard deviations of the gyroscope drift and accelerometer bias states defined as:

$$\begin{bmatrix} \underline{\sigma}_{d_{g_0}} \\ \underline{\sigma}_{b_{a_0}} \end{bmatrix} = \begin{bmatrix} \sigma_{d_{g_{0x}}} \\ \sigma_{d_{g_{0y}}} \\ \sigma_{d_{g_{0z}}} \\ \sigma_{b_{a_{0x}}} \\ \sigma_{b_{a_{0y}}} \\ \sigma_{b_{a_{0z}}} \end{bmatrix} \tag{2.43}$$

these PSD sub-matrices can be expressed as such:

$$\underline{Q}_g = 2\beta_g \begin{bmatrix} (\sigma_{d_{g_{0x}}})^2 & 0 & 0 \\ 0 & (\sigma_{d_{g_{0y}}})^2 & 0 \\ 0 & 0 & (\sigma_{d_{g_{0z}}})^2 \end{bmatrix} \tag{2.44}$$

$$\underline{Q}_a = 2\beta_a \begin{bmatrix} (\sigma_{b_{a_{0x}}})^2 & 0 & 0 \\ 0 & (\sigma_{b_{a_{0y}}})^2 & 0 \\ 0 & 0 & (\sigma_{b_{a_{0z}}})^2 \end{bmatrix}. \tag{2.45}$$

Finally, the complete PSD of the IMU states looks like:

$$\underline{Q}_{IMU} = \begin{bmatrix} \underline{0}_{3\times3} & \underline{0}_{3\times3} & \underline{0}_{3\times3} \\ \underline{0}_{3\times3} & \underline{Q}_g & \underline{0}_{3\times3} \\ \underline{0}_{3\times3} & \underline{0}_{3\times3} & \underline{Q}_a \end{bmatrix}. \tag{2.46}$$

2.4.5 Two-Way Range Covariance

For the exponentially correlated one-dimensional range bias, the range system dynamics sub-matrix F_ρ is a scalar:

$$F_\rho = -\beta_\rho. \tag{2.47}$$

The range power spectral density, which models errors in the dynamics of this state, is:

$$\underline{Q}_\rho = 2\beta_\rho(\sigma_{b_{\rho_0}})^2 \tag{2.48}$$

where $\sigma_{b_{\rho_0}}$ is the initial standard deviation of the range bias state.

2.4.6 Two-Way Doppler Covariance

As Doppler bias errors can also be modeled as exponentially correlated processes, the Doppler system dynamics sub-matrix F_d (a scalar) is described as:

$$F_d = -\beta_d. \tag{2.49}$$

Using the initial standard deviation of the Doppler state bias, $\sigma_{b_{d_0}}$, the associated power spectral density of this state becomes

$$\underline{Q}_d = 2\beta_d(\sigma_{b_{d_0}})^2. \tag{2.50}$$

2.4.7 Radar Altimeter Covariance

The complete system dynamics submatrix $\underline{F}_{ALT}$ for the altimeter states is:

$$\underline{F}_{ALT} = \begin{bmatrix} -\beta_H & 0 & \underline{0}_{1\times 3} \\ 0 & -\beta^* & \underline{0}_{1\times 3} \\ \underline{0}_{3\times 1} & \underline{0}_{3\times 1} & \underline{0}_{3\times 3} \end{bmatrix}_{5\times 5} \tag{2.51}$$

The power spectral densities of the bias and terrain FOMP bias states, Q_H and Q_{FOMP} respectively, are:

$$Q_H = 2\beta_H(\sigma_{b_{H_0}})^2 \tag{2.52}$$

$$Q_{FOMP} = 2(\beta^*)(\sigma_{b_{FOMP_0}})^2 \tag{2.53}$$

where $\sigma_{b_{H_0}}$ and $\sigma_{b_{FOMP_0}}$ are the initial standard deviations of the altitude bias state and the terrain FOMP bias state, respectively. Since there is no process noise associated with the terrain plane misalignment state, the resulting power spectral density of this state is a 3x3 dimensional zero matrix.

Finally the complete power spectral density of the altimeter states becomes:

$$\underline{Q}_{ALT} = \begin{bmatrix} Q_H & 0 & \underline{0}_{1\times 3} \\ 0 & Q_{FOMP} & \underline{0}_{1\times 3} \\ \underline{0}_{3\times 1} & \underline{0}_{3\times 1} & \underline{0}_{3\times 3} \end{bmatrix}. \tag{2.54}$$

2.4.8 Surface Radar Velocimeter Covariance

The velocimeter bias error and misalignment bias error can be modeled as exponentially correlated processes so the velocimeter system dynamics sub-matrix $\underline{F}_{VEL}$ is:

$$\underline{F}_{VEL} = \begin{bmatrix} -\beta_{SR}\underline{I}_{3\times 3} & \underline{0}_{3\times 3} \\ \underline{0}_{3\times 3} & -\beta_{mSR}\underline{I}_{3\times 3} \end{bmatrix} \tag{2.55}$$

With the initial standard deviations of these bias states denoted as:

$$\begin{bmatrix} \underline{\sigma}_{b_{SR_0}} \\ \underline{\sigma}_{b_{mSR_0}} \end{bmatrix} = \begin{bmatrix} \sigma_{b_{SR_{0x}}} \\ \sigma_{b_{SR_{0y}}} \\ \sigma_{b_{SR_{0z}}} \\ \sigma_{b_{mSR_{0x}}} \\ \sigma_{b_{mSR_{0y}}} \\ \sigma_{b_{mSR_{0z}}} \end{bmatrix}, \tag{2.56}$$

the power spectral densities $\underline{Q}_{SR}$ and $\underline{Q}_{mSR}$ look like:

$$\underline{Q}_{SR} = 2\beta_{SR}\begin{bmatrix} (\sigma_{b_{SR_{0x}}})^2 & 0 & 0 \\ 0 & (\sigma_{b_{SR_{0y}}})^2 & 0 \\ 0 & 0 & (\sigma_{b_{SR_{0z}}})^2 \end{bmatrix} \tag{2.57}$$

$$\underline{Q}_{mSR} = 2\beta_{mSR}\begin{bmatrix} (\sigma_{b_{mSR_{0x}}})^2 & 0 & 0 \\ 0 & (\sigma_{b_{mSR_{0y}}})^2 & 0 \\ 0 & 0 & (\sigma_{b_{mSR_{0z}}})^2 \end{bmatrix} \tag{2.58}$$

and the complete power spectral density of the velocimeter states is:

$$\underline{\underline{Q}}_{VEL} = \begin{bmatrix} \underline{\underline{Q}}_{SR} & \underline{\underline{0}}_{3\times 3} \\ \underline{\underline{0}}_{3\times 3} & \underline{\underline{Q}}_{mSR} \end{bmatrix}. \tag{2.59}$$

2.5 Measurement Models

The four measurement types used in this design are two-way range, two-way Doppler, altitude, and surface velocity. Further description of these measurements, including their models as well as their partial derivatives, which are required for the measurement sensitivity matrix $\underline{H}_k$ (Equation 2.14) in the extended Kalman filter, is presented in the following paragraphs.

2.5.1 Two-Way Range Measurement

The distance between the lander and a navigation satellite or beacon is called the range. The equation for the two-way range measurement ρ from the spacecraft to a navigation satellite is:

$$\begin{aligned} \rho &= \sqrt{(\underline{R}_L - \underline{R}_S)^T(\underline{R}_L - \underline{R}_S)} + b_{\rho L} + b_{\rho S} + \nu_\rho \\ \rho &= h_\rho(\underline{x}(t), t) + \nu_\rho \end{aligned} \tag{2.60}$$

where $b_{\rho L}$ and $b_{\rho S}$ are the respective range biases for the spacecraft and the satellite and ν_ρ is the range error with zero mean and a range dependent variance V_ρ described by [12]:

$$V_\rho = (10^{-6} h_\rho \cdot \sigma_\rho)^2 \tag{2.61}$$

where σ_ρ is a constant.

The measurement partial derivatives for the measurement sensitivity matrix are:

$$\frac{\partial h_\rho(\underline{x}(t), t)}{\partial \underline{R}_L} = \underline{u}_R^T \tag{2.62}$$

$$\frac{\partial h_\rho(\underline{x}(t), t)}{\partial \underline{R}_S} = -\underline{u}_R^T \tag{2.63}$$

$$\frac{\partial h_\rho(\underline{x}(t), t)}{\partial b_{\rho L}} = 1 \tag{2.64}$$

$$\frac{\partial h_\rho(\underline{x}(t), t)}{\partial b_{\rho S}} = -1 \tag{2.65}$$

where $\underline{u}_R$ is the following unit vector:

$$\underline{u}_R = \frac{\underline{R}_L - \underline{R}_S}{|\underline{R}_L - \underline{R}_S|}. \tag{2.66}$$

In addition, for the range to a navigation surface beacon, the beacon position $\underline{R}_B$ is substituted for the satellite position $\underline{R}_S$ and the beacon range bias $b_{\rho B}$ is substituted for the satellite range bias $b_{\rho S}$. [12]

2.5.2 Two-Way Doppler Measurement

The Doppler measurement, or the rate of change of the range measurement, from the spacecraft to a satellite is designated as:

$$\dot{\rho} = \frac{\underline{r}^T \underline{v}}{|\underline{r}|} + b_{dL} + b_{dS} + \nu_d \tag{2.67}$$

$$\dot{\rho} = h_d(\underline{x}(t), t) + \nu_d$$

where:

$$\underline{r} = \underline{R}_L - \underline{R}_S \tag{2.68}$$

$$\underline{v} = \underline{V}_L - \underline{V}_S, \tag{2.69}$$

b_{dL} and b_{dS} are the respective Doppler biases for the lander and the satellite, and ν_d is the measurement noise with zero mean and range dependent variance V_d described by:

$$V_d = (10^{-6} h_\rho \cdot \sigma_d)^2 \tag{2.70}$$

where σ_d is a constant.

The partial derivatives for the measurement sensitivity matrix for Doppler measurements are:

$$\frac{\partial h_d(\underline{x}(t),t)}{\partial \underline{R}_L} = \frac{(\underline{r}\times\underline{v}\times\underline{r})^T}{|\underline{r}|^3} \tag{2.71}$$

$$\frac{\partial h_d(\underline{x}(t),t)}{\partial \underline{R}_S} = -\frac{(\underline{r}\times\underline{v}\times\underline{r})^T}{|\underline{r}|^3} \tag{2.72}$$

$$\frac{\partial h_d(\underline{x}(t),t)}{\partial \underline{V}_L} = \frac{\underline{r}^T}{|\underline{r}|} \tag{2.73}$$

$$\frac{\partial h_d(\underline{x}(t),t)}{\partial \underline{V}_S} = -\frac{\underline{r}^T}{|\underline{r}|} \tag{2.74}$$

$$\frac{\partial h_d(\underline{x}(t),t)}{\partial b_{dL}} = 1 \tag{2.75}$$

$$\frac{\partial h_d(\underline{x}(t),t)}{\partial b_{dS}} = 1 \tag{2.76}$$

Like the range measurements, Doppler measurements to a navigation surface beacon will require $\underline{R}_S$ to be substituted with $\underline{R}_B$ and b_{dS} substituted with the Doppler bias of that beacon b_{dB}. In addition, the partial derivative of beacon velocity (Equation 2.74) is removed since the velocity of the surface beacon is not estimated in the state. [12]

2.5.3 Altitude Measurement

The equation for the altitude measurement is:

$$\begin{aligned} H &= \sqrt{(\underline{R}_L - R_P\underline{u}_L - \underline{b}^I_{TP})^T(\underline{R}_L - R_P\underline{u}_L - \underline{b}^I_{TP})} + b_H + b_{FOMP} + \nu_H \\ H &= h_H(\underline{x}(t),t) + \nu_H \end{aligned} \tag{2.77}$$

where R_p is the planetary radius, $\underline{u}_L$ is the unit vector of the lander position $\underline{R}_L$, $\underline{b}^I_{TP}$ is the terrain plane misalignment in inertial coordinates (as opposed to the terrain plane misalignment state which is in LVLH coordinates), and ν_H is the altimeter measurement

noise. This noise is zero mean with an altitude based variance V_H described by:

$$V_H = (\sigma_0 + \sigma_H h_H)^2 \tag{2.78}$$

where σ_0 represents the altimeter noise constant and σ_H is the altimeter noise slope constant. In addition, the altimeter has a maximum altitude set that the lander must reach before it starts to take measurements. This conveniently sets a maximum for the altimeter noise variance as well.

The altitude measurement partial derivatives are:

$$\frac{\partial h_H(\underline{x}(t), t)}{\partial \underline{R}_L} = \underline{u}_L = \frac{\underline{R}_L}{|\underline{R}_L|} \tag{2.79}$$

$$\frac{\partial h_H(\underline{x}(t), t)}{\partial b_H} = 1 \tag{2.80}$$

$$\frac{\partial h_H(\underline{x}(t), t)}{\partial b_{FOMP}} = 1 \tag{2.81}$$

$$\frac{\partial h_H(\underline{x}(t), t)}{\partial \underline{b}_{TP}} = -(\underline{T}_I^L \underline{u}_L)^T \tag{2.82}$$

where $\underline{T}_I^L$ is the transformation matrix from inertial coordinates to planet-centered coordinates [12].

2.5.4 Surface Velocity Measurement

With the surface radar velocimeter, the velocity of the lander relative to the Martian surface directly beneath can be measured. The equation of this measurement, or surface radar velocity, can be expressed as:

$$\begin{aligned} \underline{V}_{rel}^P &= \underline{T}_I^P(\underline{V}_{rel}^I + \underline{b}_{SR}) + \underline{\nu}_{SR} = \underline{T}_I^P(\underline{V}_L - \underline{\omega}_M \times \underline{R}_L + \underline{b}_{SR}) + \underline{\nu}_{SR} \\ \underline{V}_{rel}^P &= \underline{h}_{SR}(\underline{x}(t), t) + \underline{\nu}_{SR} \end{aligned} \tag{2.83}$$

where $\underline{T}_I^P$ is the transformation matrix from inertial coordinates to planet surface coordinates (since attitude dynamics are not taken into account, this matrix will be assumed to be

an identity matrix), $\underline{b}_{SR}$ is the surface radar bias, and $\underline{v}_{SR}$ is the surface velocity measurement noise with zero mean and variance V_{SR}:

$$V_{SR} = (\sigma_{SR_0} + \sigma_{SR_v}|\underline{h}_{SR}|)^2 \tag{2.84}$$

To calculate the partial derivatives, the differential of the measurement must be calculated. First of all, the above transformation matrix must be established:

$$\delta \underline{T}_I^P = \underline{T}_I^P \delta \underline{\theta} \times \tag{2.85}$$

where $\delta\underline{\theta}$ is the change in position of the inertial frame with respect to the surface frame. In addition, it should be clarified that the cross product operator can also take the form of a skew symmetric matrix. The case of the planetary rotational rate looks like:

$$\underline{\omega}_M \times = \begin{bmatrix} \omega_{Mx} \\ \omega_{Mx} \\ \omega_{Mx} \end{bmatrix} \times = \underline{S}_\omega = \begin{bmatrix} 0 & -\omega_{Mx} & \omega_{Mx} \\ \omega_{Mx} & 0 & -\omega_{Mx} \\ -\omega_{Mx} & \omega_{Mx} & 0 \end{bmatrix} \tag{2.86}$$

Now the differential of the measurement becomes:

$$\begin{aligned} \delta \underline{V}_{rel}^P = & -\underline{T}_I^P(\underline{V}_L - R_P \underline{\omega}_M \times \underline{u}_L + \underline{b}_{SR}) \times (\delta \underline{b}_g + \delta \underline{b}_{mSR}) + \underline{T}_I^P \delta \underline{V}_L \\ & -\frac{R_P}{|\underline{R}_L|} \underline{T}_I^P \underline{\omega}_M \times (\underline{I}_{3\times 3} - \underline{u}_L \underline{u}_L^T) \delta \underline{R}_L + \underline{T}_I^P \delta \underline{b}_{SR} \end{aligned} \tag{2.87}$$

Without loss of generality in these equations, the transformation matrix is assumed to be an identity matrix in this differentiation, and the partial derivatives become:

$$\frac{\partial h_{SR}(\underline{x}(t), t)}{\partial \underline{R}_L} = \frac{R_P}{|\underline{R}_L|} \underline{S}_\omega (\underline{I}_{3\times 3} - \underline{u}_L \underline{u}_L^T) \tag{2.88}$$

$$\frac{\partial h_{SR}(\underline{x}(t), t)}{\partial \underline{V}_L} = \underline{I}_{3\times 3} \tag{2.89}$$

$$\frac{\partial h_{SR}(\underline{x}(t), t)}{\partial \underline{b}_g} = -(\underline{V}_L - R_P \underline{\omega}_M \times \underline{u}_L + \underline{b}_{SR}) \times \tag{2.90}$$

$$\frac{\partial h_{SR}(\underline{x}(t), t)}{\partial \underline{b}_{SR}} = \underline{I}_{3\times 3} \tag{2.91}$$

$$\frac{\partial h_{SR}(\underline{x}(t), t)}{\partial \underline{b}_{mSR}} = -(\underline{V}_L - R_P \underline{\omega}_M \times \underline{u}_L + \underline{b}_{SR}) \times \tag{2.92}$$

The cross products in these partial derivatives are to be treated as skew-symmetric matrices, as shown in Equation 2.86. [12]

Chapter 3

Simulation Description

3.1 Introduction

The computer program written to evaluate the performance of the proposed navigation algorithm is presented in this chapter. First, the general sequence of the program, including its flowchart form, is described. Next, further detail is given on major subroutines, including principal inputs and outputs. Finally, all initial conditions and constants used in the simulation are presented. This program, which simulates a spacecraft during the entry phase at Mars, was coded in MATLAB version 5.1. Since the code takes advantages of new features that MATLAB 5.0 has to offer over prior versions (e.g. MATLAB 4.2), it will run only on MATLAB version 5.0 or higher.

3.2 Program Simulation Description

The complete program can be seen as two separate simulations: a truth simulation and an estimation simulation. From given initial conditions, the truth simulation propagates the state and covariance without navigational errors or noises to create a 'truth,' or nominal, profile of the state and its variances. In contrast, the estimation simulation will output an estimated state and covariance profile from state and covariance propagation (using simulated errors and perturbed initial conditions) as well as measurement filtering. Different estimated profiles can be compared to the truth profile to test the performance of the filter with different measurements. Because the estimation simulation requires information from the truth simulation for the measurement filtering process, the truth simulation must be executed before the estimation simulation.

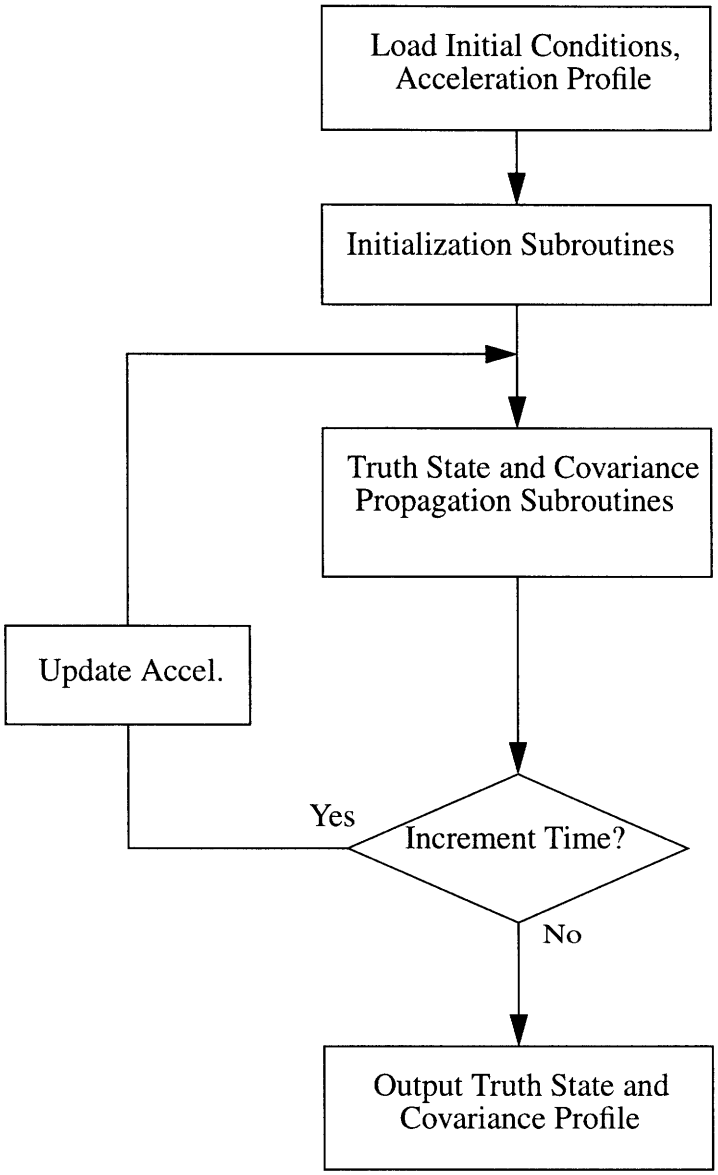

Figure 3.1: Truth Simulation Algorithm

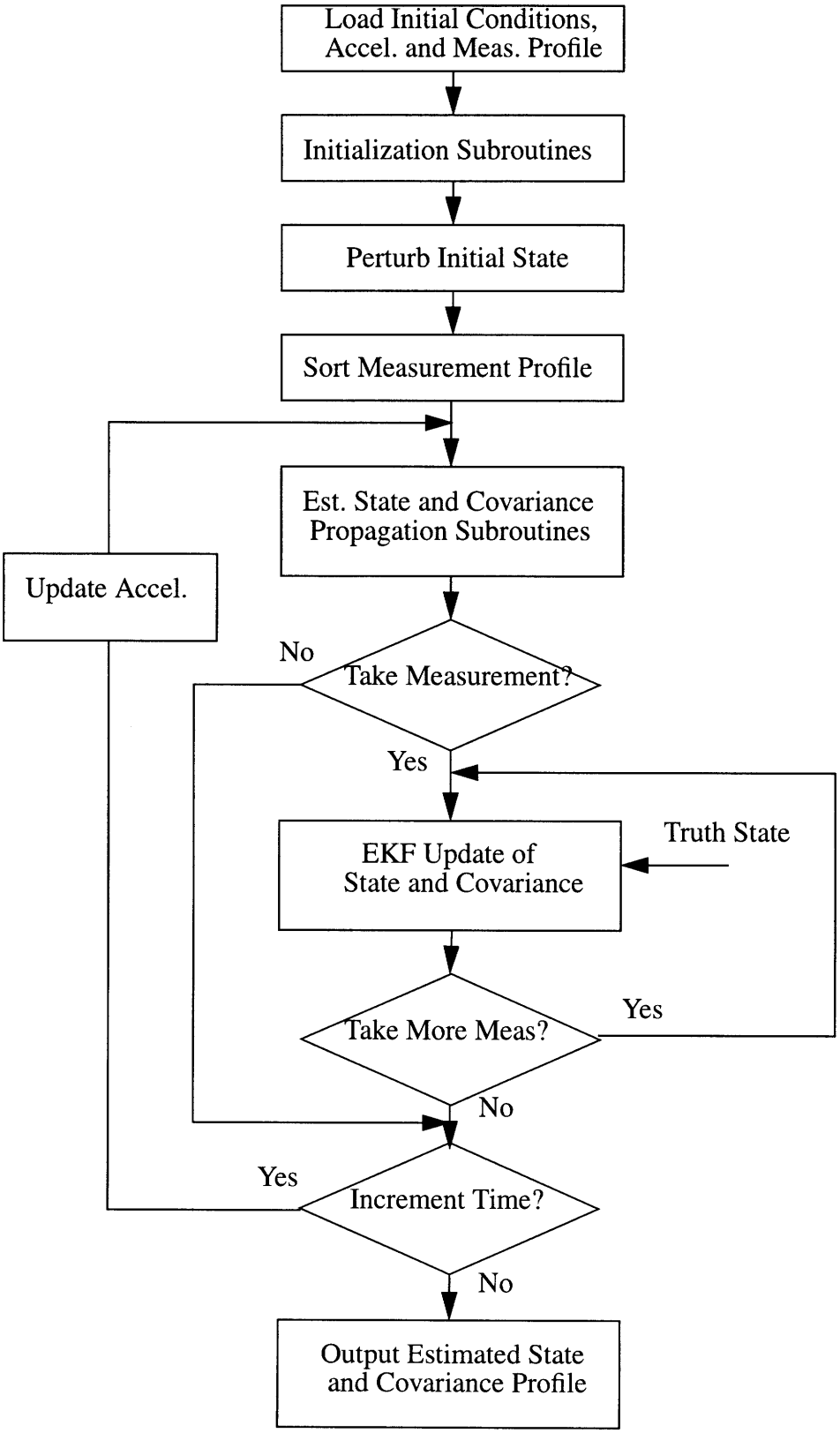

Figure 3.2: Estimation Simulation Algorithm

3.2.1 Truth Simulation Executive Program

The general sequence of the truth simulation is shown in Figure 3.1 and described as follows: an executive program receives all initial conditions, including the pre-determined acceleration profile, whereafter a set of initialization subroutines (one for each set of states) takes relevant initial conditions and creates an initial state vector and covariance matrix. This state and covariance is then propagated, via the propagation subroutines (one for each set of states), based on the time steps provided by the acceleration profile. The state and covariance at the end of each time step is stored for evaluation. The program checks the acceleration profile for the next time step and, if it finds one, sends the state and covariance to the beginning of the propagation stage to repeat the process.

3.2.2 Estimation Simulation Executive Program

The sequence of the estimation simulation, as shown in Figure 3.2, is quite similar to that of the truth simulation. An executive program receives the same initial conditions, in addition to the state and covariance truth profile and a pre-determined measurement profile. This measurement profile, which instructs the executive program to take which measurements at what time steps, is then sorted in chronological order. Like the truth simulation, the necessary initial conditions are sent through the same initialization subroutines to create an initial estimated state vector and covariance matrix. This initial estimated state is then perturbed before it and its covariance matrix are updated with the propagation subroutines. The perturbations are added so as to determine that the extended Kalman filter (EKF) is able to deal with an altered state appropriately, adjusting its values to keep them close to the corresponding truth state values. After propagation at each time step, the executive program consults with the measurement profile to check which measurement types to take, if any, at the current time step. For each approved type, the state and covariance is sent to a measurement subroutine where a measurement is taken and processed in

the EKF to update the state estimate and associated covariance. If the spacecraft is taking two measurements of the same type, then the state and covariance are sent to the appropriate measurement subroutine to process one measurement and then sent again to process the second one. The state and covariance after the filtering stage at each time step is then stored. As with the truth simulation, the executive program checks the acceleration profile for the next time step and, if one exists, sends the state and covariance back to the beginning of the propagation stage where the cycle is repeated until there are no more time steps.

3.2.3 Program Subroutine Types

There are three chief subroutine types called by the executive programs: initialization, propagation, and measurement filtering. While the initialization and propagation subroutines are quite similar for the truth and estimated simulation cases, the measurement filtering subroutines are exclusively called by the estimated simulation program, since the truth case involves no filtering.

The main responsibility of the initialization subroutines is to create an initial state and covariance matrix. There are initialization subroutines for the lander, each satellite and surface beacon, each range bias state, each Doppler bias state, the IMU bias states, the altimeter bias states, and the velocimeter bias states. In addition, the order of these subroutines determines the order of the states. The subroutines receive inputs such as initial positions, velocities, and uncertainties of all spacecraft and surface beacons, as well as necessary variables for bias dynamics, such as time constants and initial bias uncertainties. Spacecraft state conditions arrive in the form of orbital elements and uncertainties while beacon state conditions are received in local coordinates, but the complete initial state and covariance have these states in inertial (Mars-centered) coordinates. All bias states are ini-

tialized to zero. The subroutine outputs include the initial state and covariance as well as a database of all bias dynamics for propagation.

The propagation subroutines are responsible for updating the state and covariance in time, based on the dynamics described in Sections 2.3 and 2.4. Like the initialization subroutines, there are propagation subroutines for the lander, each satellite and surface beacon, each range bias state, each Doppler bias state, the IMU bias states, the altimeter bias states, and the velocimeter bias states. The propagation is performed using the fourth-order Runge-Kutta method, a standard numerical method used to solve continuous differential equations at discrete time steps. Each subroutine individually propagates its set of states but it can not do the same for the covariance matrix, since this is a collective description of the state variances. However, the subroutines can update the system dynamics matrix $\underline{F}$ and the process noise matrix $\underline{Q}$ (matrices used in the covariance differentiation: Equation 2.8), and output them to the executive program which performs the covariance propagation. Inputs include the state, the covariance, the system dynamics matrix, the process noise matrix, the bias database, a database of four state midpoint values for fourth-order Runge-Kutta calculations, and the acceleration (for lander propagation). Updated outputs include the state, the system dynamics matrix, the process noise matrix, and the state midpoint value database. It is also notable to mention that since the biases are initialized to zero and there are no noises in the truth simulation, the bias states will all have zero values throughout the truth simulation.

The measurements are taken and processed into the extended Kalman filter in the measurement subroutines. One subroutine is responsible for each measurement. Measurements and their variances, created with the models discussed in Section 2.5, are used in the EKF to improve the state and covariance. Inputs include the state, the covariance, and constants used in measurement variance models. The subroutines will output the updated state

and covariance. It should be mentioned that the simulation will not take range or Doppler measurements if the appropriate navigation satellites or beacons are obstructed or not within sight. In addition, no altitude or surface velocity measurements are taken if the lander is not within a certain height above the Martian surface (20,000 metres for this simulation).

3.3 Simulation Initial Conditions and Constants

The initial conditions and constants presented in this section are used in the simulation to evaluate its performance. They are divided into acceleration profile/planetary constants, state initial conditions and constants, and measurement noise constants.

3.3.1 Acceleration Profile and Planetary Constants

The acceleration profile and Mars planetary constants were taken from values used in the Ada-encoded Linear Covariance Tool [12] developed at the Charles Stark Draper Laboratory (CSDL) for NASA-JSC. As will be shown, this code is also the source of some of the initial conditions and standard deviations used in the simulation. The given acceleration profile gives values for total acceleration, i.e. gravitational and non-gravitational. The Mars planetary constants in this simulation are presented in Table 3.1.

Planetary Constants	**Value**
Gravitational Constant μ_M	4.2828287e13 m^3/s^2
Equatorial Radius R_{eq}	3.3934e6 m
Polar Radius R_{po}	3.3757e6 m
Planetary Rotational Rate $\underline{\omega}_M$ (inertial XYZ coordinates)	$\begin{bmatrix} 0 \\ 0 \\ 7.088218e\text{-}5 \end{bmatrix}$ rad/sec

Table 3.1: Martian Planetary Constants

From the planetary rotational rate value, it is clear that the planet Mars is spinning purely on the inertial Z-axis for this simulation.

3.3.2 State Initial Conditions and Constants

The initial conditions and relevant constants of the state are displayed in the following sets of state variables: lander states, satellite states, beacon states, IMU bias states, range/Doppler bias states, and altimeter/velocimeter bias states.

The initial state and covariance of the lander, already in inertial coordinates, also came from the CSDL covariance code. However, the initial covariance matrix, which is strictly diagonal, is modified in this simulation in that it takes the highest position and velocity variance of one axis and applies it to all axes. The values are displayed below in Table 3.2.

Lander State	Initial State	Initial Std. Deviation
Position in X axis	1.155577e7 m	632.456 m
Position in Y axis	0.0 m	632.456 m
Position in Z axis	0.0 m	632.456 m
Velocity in X axis	-5.127135e3 m/s	1.85193 m/s
Velocity in Y axis	2.238625e4 m/s	1.85193 m/s
Velocity in Z axis	0.0 m/s	1.85193 m/s

Table 3.2: Initial Lander States and Standard Deviations

Three navigation satellites are used in this simulation. Their initial states, in orbital elements, were designed such that each one will be along a different axis relative to the lander. Initial uncertainties, in the form of local coordinates, are conservative approximations based on [12]. These approximations were confirmed as reasonable from a NASA-JPL paper discussing the accuracy of the Mars Global Observer in the Mars atmosphere [13]. Translating these values to inertial coordinates, the initial satellite states for all three

satellites are presented in Table 3.3 while their standard deviations are displayed in Table 3.4.

Satellite State	Satellite 1	Satellite 2	Satellite 3
Position in X axis	7.7379e6 m	4.9182e6 m	3.4434e6 m
Position in Y axis	-1.5561e6 m	5.6137e6 m	2474.8 m
Position in Z axis	-5.3593e5 m	-1.5561e6 m	6.0862e6 m
Velocity in X axis	404.3 m/s	-1856.9 m/s	11.755 m/s
Velocity in Y axis	2162.6 m/s	1410.9 m/s	2474.8 m/s
Velocity in Z axis	-441.06 m/s	-62.365 m/s	20.777 m/s

Table 3.3: Initial Satellite States

Satellite Std. Dev.	Satellite 1	Satellite 2	Satellite 3
Position in X axis	87.968 m	177.31 m	75.0 m
Position in Y axis	220.81 m	158.29 m	171.23 m
Position in Z axis	149.19 m	149.19 m	209.3 m
Velocity in X axis	0.051179 m/s	0.040586 m/s	0.06515 m/s
Velocity in Y axis	0.023314 m/s	0.044935 m/s	0.048005 m/s
Velocity in Z axis	0.042723 m/s	0.045999 m/s	0.034821 m/s

Table 3.4: Initial Satellite Standard Deviations

The simulation will also contain two surface beacons, whose initial positions are given in latitude-longitude coordinates. One beacon will be located directly below the final position of the lander while the other one will be five degrees latitude north of that spot. Initial uncertainties in position are taken from NASA-JPL, which is able to track beacons on Mars via the Deep Space Network (DSN) [11], and are given in East-North-Up (ENU) coordinates. Transforming these positions and uncertainties to inertial coordinates yields the value in Table 3.5.

Beacon State/Std. Deviation	Initial State	Initial Std. Dev.
Beacon 1 Position in X axis	3.3335e6 m	50 m
Beacon 1 Position in Y axis	6.3481e5 m	50 m
Beacon 1 Position in Z axis	-1084.3 m	150 m
Beacon 2 Position in X axis	3.3275e6 m	51.421 m
Beacon 2 Position in Y axis	5.9712e5 m	50.046 m
Beacon 2 Position in Z axis	2.9269e5 m	149.5 m

Table 3.5: Initial Beacon States and Standard Deviations

Actually, in the standard deviations of Beacon 1 (the beacon directly below the final position of the lander), the ENU coordinates translate directly to XYZ inertial coordinates with the Z-axis representing the 'North'-axis.

The inertial measurement unit (IMU) consists of three gyroscopes and three accelerometers (one for each axis) and it is represented in the simulation with nine states: a gyroscope bias, a gyroscope drift, and an accelerometer bias, each in three dimensions. As mentioned in the previous section, all mean values for initial conditions, including bias states, in this simulation are initialized to zero. However, an initial standard deviation is necessary for each state. In addition, the integration of the gyroscope drift and accelerometer bias each require a time constant.

All time constants in this simulation were given a starting value of 1 sec, to represent the difference in time steps in the acceleration profile as well as to provide a good variety of fluctuations in the biases. In the process of tuning the filter for the different measurement cases, these values were adjusted to the current values presented in the following tables.

The IMU state values chosen for this simulation are as follows:

IMU State	Initial State (in all axes)	Initial Std. Deviation (in all axes)	Time Constant
Gyroscope Bias	0 arcsec	40.0 arcsec	-
Gyroscope Drift	0 deg/hr	0.02 deg/hr	1.0 sec
Accelerometer Bias	0 μg	50.0 μg	1.0 sec

Table 3.6: IMU Initial States, Standard Deviations and Time Constants

The initial standard deviations from this table are approximations based on a number of sources describing gyroscopes and accelerometers used in industry [1, 6, 12].

The scalar range measurement biases will have the same standard deviation and time constant for each spacecraft and beacon. This will also be true for its delta-range counterparts, the Doppler measurement biases. The values chosen are as such:

State	Initial State	Initial Std. Deviation	Time Constant
Range Meas Bias	0 m	20.0 m	1.5 sec
Doppler Meas Bias	0 m/s	0.60 m/s	1.6 sec

Table 3.7: Range/Doppler Initial States, Standard Deviations, and Time Constants

When compared with other sources, the standard deviations of the range bias [11, 12], and the Doppler bias [10] were found to be reasonable approximations.

The surface-based measurement sensors involve eleven states in all. The altimeter involves five states: two first-order Markov processes (altimeter bias and terrain FOMP bias) and three constants (three-dimensional terrain misalignment). All five will require initial values and standard deviations but only the two first-order Markov processes will require time constants. In actuality, the time constant of the terrain FOMP bias is dependent on the angular momentum of Mars as well as an altimeter correlation distance. Thus, this correlation distance is the necessary input for the dynamics of this state. The six states of the velocimeter are the three dimensional velocimeter bias and misalignment bias,

which are also modeled as first-order Markov processes. For both biases, the standard deviations in each direction will be of the same value. The initial standard deviations and correlation distance in the following table are approximations based from various sources [1, 12, 18].

State	Initial State	Initial Std. Deviation	Time Constant
Altimeter Meas. Bias	0 m	1.0 m	1.0 sec
Terrain FOMP Bias	0 m	1.0 m	50000 m (correl. dist.)
Terrain Misalignment (in each axis)	0 m	20.0 m	-
Velocimeter Bias (in each axis)	0 m/s	0.30 m/s	1.0 sec
Velocimeter Misalignment (in each axis)	0 deg	0.067 deg	1.0 sec

Table 3.8: Altimeter/Velocimeter Initial States, Std. Deviations, and Time Constants

3.3.3 Measurement Noise Model Constants

As illustrated in Section 2.5, all measurement noise variance models are linear functions of the measurements. The exception is that the Doppler noise variance model is a linear function of the range measurement, such that a greater distance between the lander and a satellite or beacon would result in larger measurement noises. Thus, the basic equation defining the noise models is:

$$V(t) = (C + m \cdot z(t))^2 \qquad \textbf{(3.1)}$$

where $V(t)$ is the noise variance, C is a constant, m is a slope, and $z(t)$ is the measurement value from the truth model. The constants and slopes used in the measurement noise variance models of this simulation, taken from the CSDL code [12] and empirically adjusted for the purpose of tuning the EKF, are shown in the Table 3.9.

Measurement	Constant	Slope	Max Variance	Min Variance
Range	0 m	6.67e-6	$(40.65\ m)^2$	$(4.0\ m)^2$
Doppler	0 m/s	0.33e-6 s^{-1}	$(2.03\ m/s)^2$	$(1.5\ m/s)^2$
Altitude	2.0 m	2.0e-4	$(6\ m)^2$	$(3.6\ m)^2$
Surface Vel.	0.3 m/s	2.0e-3	$(2.42\ m/s)^2$	$(0.67\ m/s)^2$

Table 3.9: Measurement Noise Variance Model Constants

The minimum range and Doppler measurement noise variances are set values to ensure that they will not fall too low, as would be the case with the surface beacon measurements. Other maximum and minimum values are determined using the measurement extremes in Equation 3.1.

Chapter 4

Covariance Analysis

4.1 Introduction

In this chapter, simulation results are presented to analyze the performance of the extended Kalman filter. These covariance results are obtained by running the simulation with different measurement profiles. In the following sections, the nominal trajectories of the lander, as well as of all navigation satellites and surface beacons, are displayed and the covariance analyses for all selected measurement profiles are addressed in detail. Finally, the measurements types in these profiles are optimally sequenced to produce the best overall results.

4.2 Truth State Trajectories

The nominal trajectories of the lander, navigation satellites, and surface beacons can be obtained directly from the truth state profile, since the truth state profile contains no noises or initial perturbations. In Figures 4.1 to 4.5, the position and velocity states of the lander et al are presented separately. Then, in Figure 4.6, all paths are mapped in an inertial coordinate scale, with the center of Mars as the origin. Since the acceleration profile only lasts 162 seconds, it should be forewarned that not much movement can be seen on the full Mars-centered scale. However, the relative positions of the spacecraft and beacons, on this scale, are well exemplified. Z axis projections of the initial satellite positions are also displayed in this figure to provide a clearer image of the entire geometry.

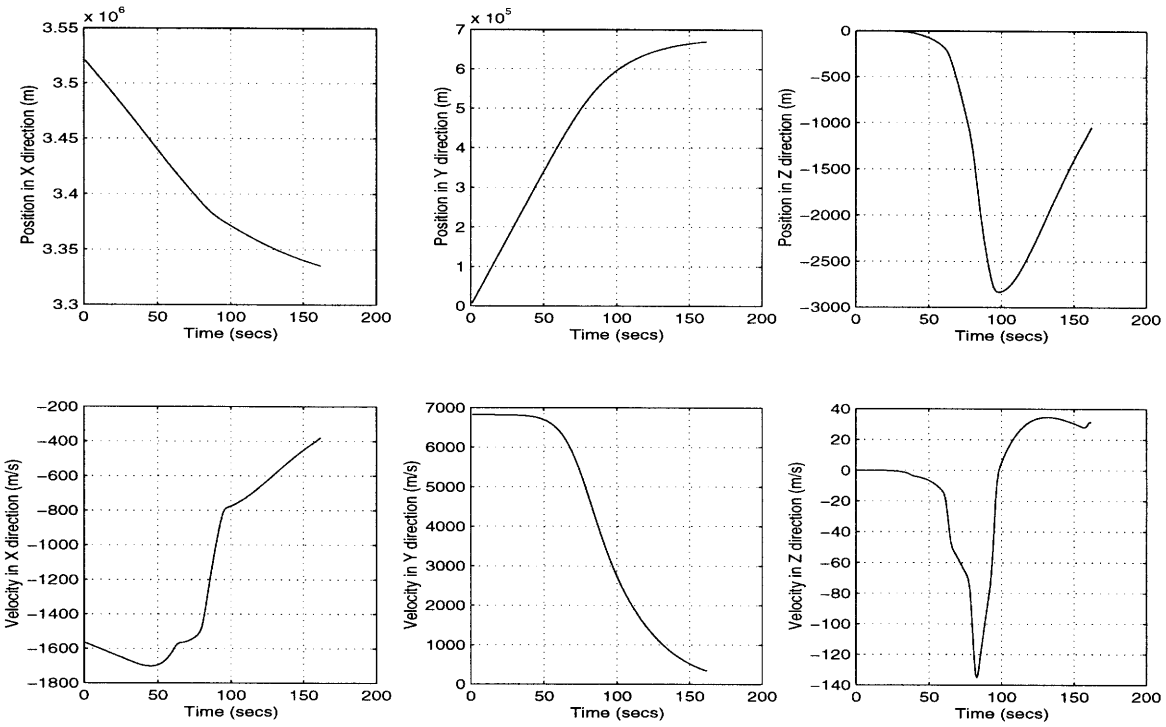

Figure 4.1: Lander Position and Velocity Truth States

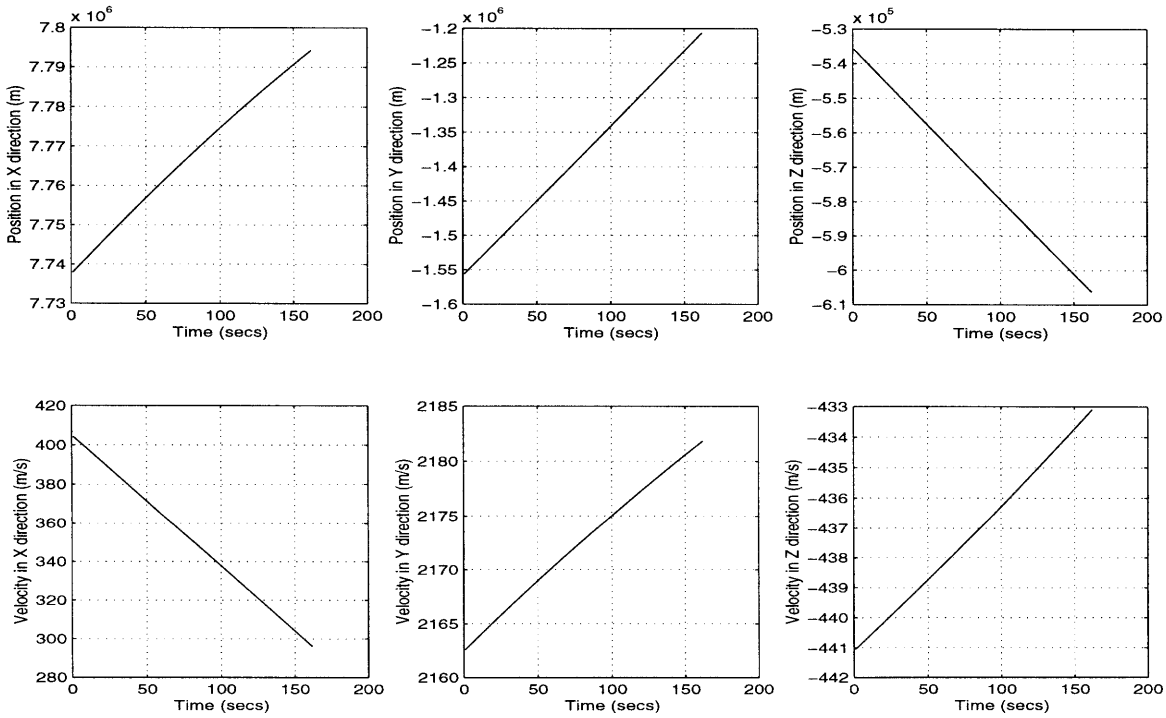

Figure 4.2: Satellite 1 Position and Velocity Truth States

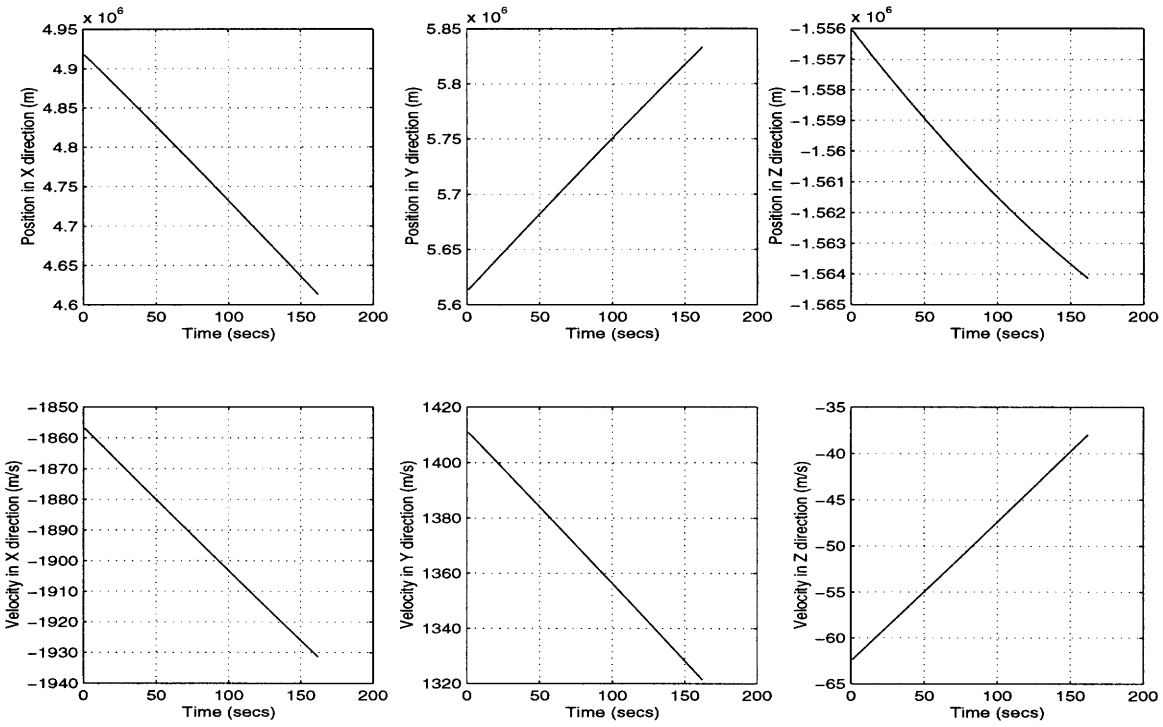

Figure 4.3: Satellite 2 Position and Velocity Truth States

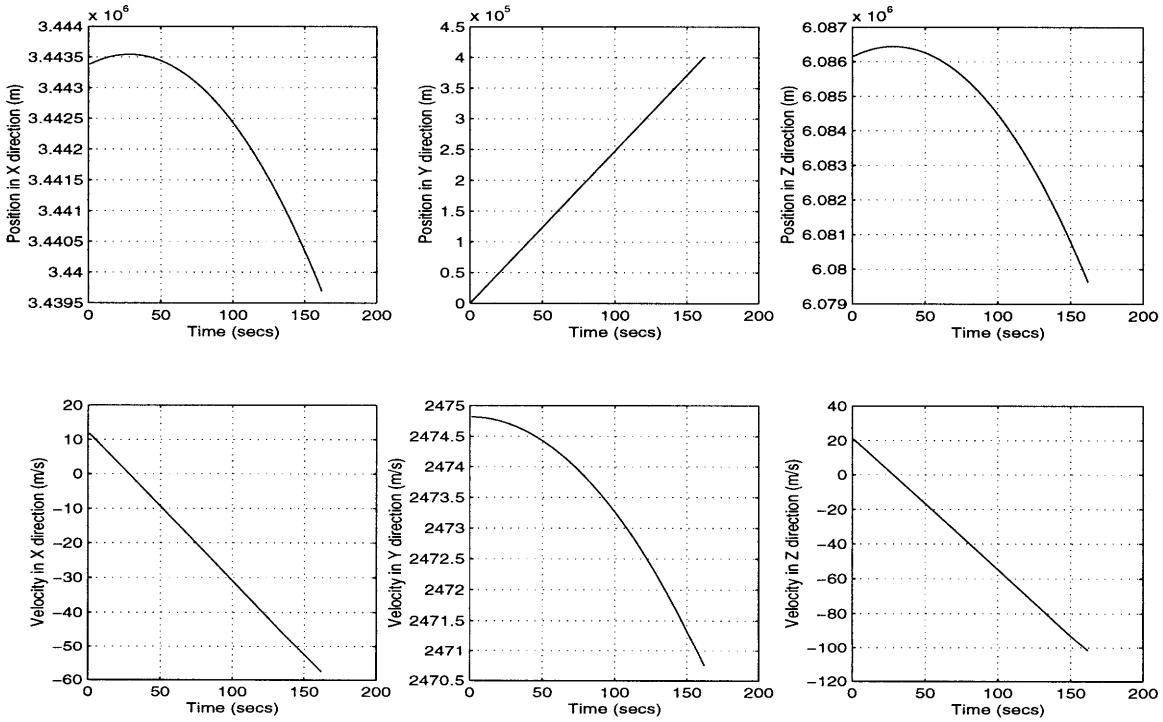

Figure 4.4: Satellite 3 Position and Velocity Truth States

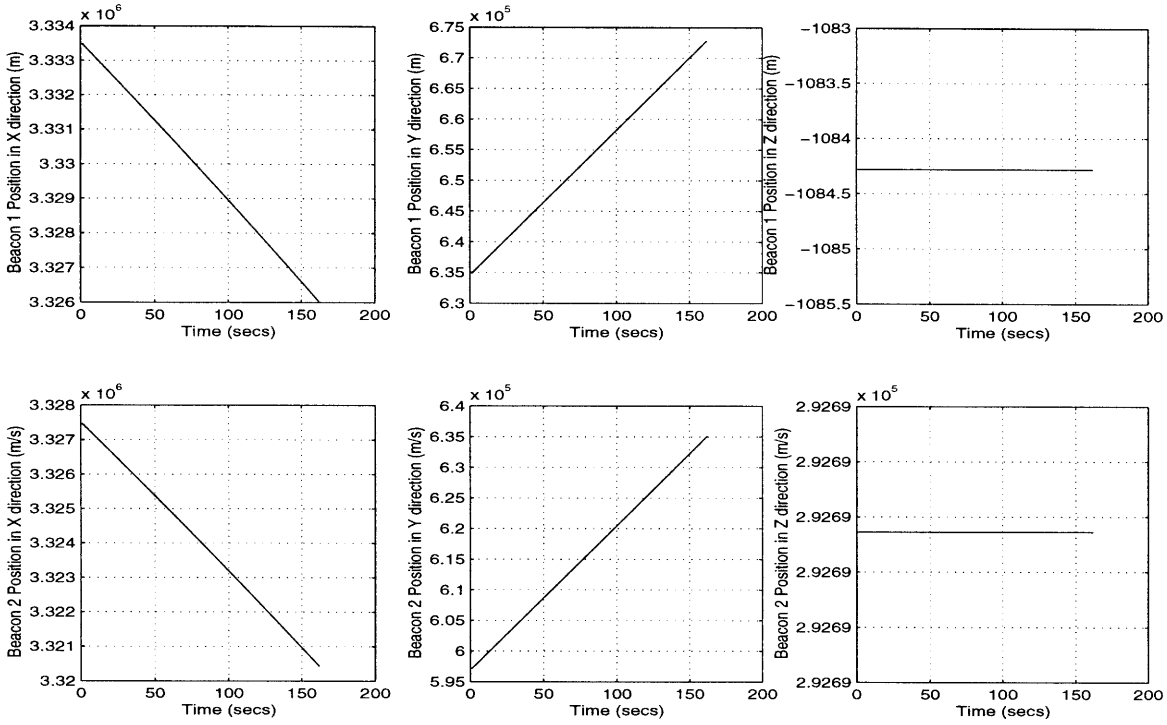

Figure 4.5: Beacon Truth States

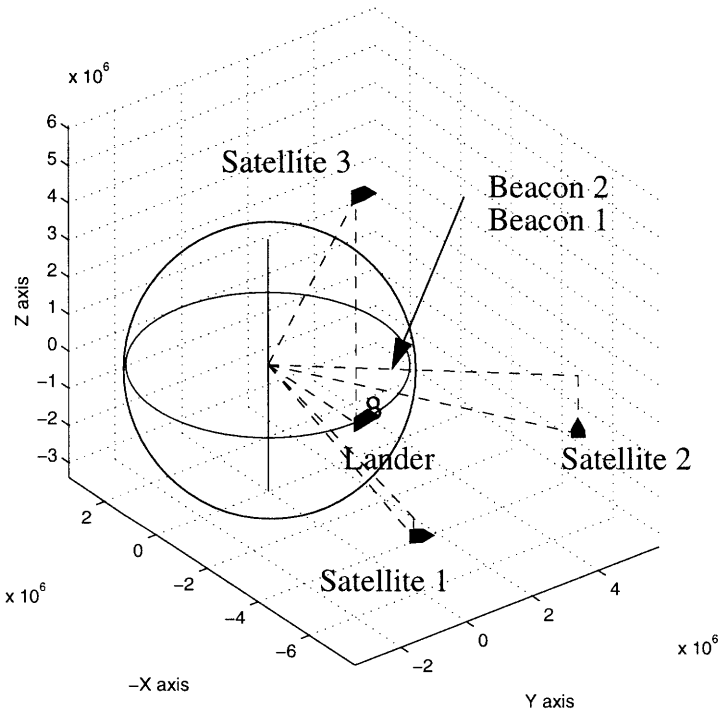

Figure 4.6: Nominal Trajectories in Inertial Coordinate Scale

4.3 Measurement Type Covariance Analysis

The covariance analyses for each measurement profile are presented in this section. The seventeen selected measurement profiles, which were chosen to address the performance of each measurement type singularly, are grouped as follows: no measurement, satellite range measurement (with Satellite 1, Satellite 2, Satellite 3, and all satellites), satellite Doppler measurement (with Satellite 1, Satellite 2, Satellite 3, and all satellites), beacon range measurement (with Beacon 1, Beacon 2, and both beacons), beacon Doppler measurement (with Beacon 1, Beacon 2, and both beacons), altitude measurement, and surface velocity measurement. In addition, all measurement profiles have measurements taken at all time steps starting with the third time step.

For each simulation run, all estimated position and velocity states have initial perturbations of one (initial) standard deviation with a random sign (this can be denoted as $\pm 1\sigma$). This is to ensure that the EKF can deal with considerable initial state errors and make the state estimation errors converge for each measurement type. However, it should be mentioned that it is not ideal to use very large initial perturbations as the general EKF algorithm does not guarantee stability for such situations [8].

The covariance analysis plots use three main formats. The first format shows the estimation errors (difference between truth and estimate) of the relevant position and velocity states for that simulation over time. Each estimation error will be bounded by three times its standard deviation (3σ). The second format compares the magnitudes of relevant position and velocity standard deviations of the current measurement profile and of the no measurement case. Of course, this format cannot apply to the profile of no measurements, but the lander position and velocity standard deviation magnitudes are shown for reference. The third format presents the estimation errors of relevant bias states with 1σ and 3σ bounds.

4.3.1 No Measurement Case

The simulation is ran without taking measurements (and likewise, without using the extended Kalman filter). Its results can then be compared those of simulations that do use measurements. Performance data illustrated in this section concentrate on errors in the lander states, since these are the most important states and their performance accurately reflects the performance of satellite and beacon states as well.

The lander estimation errors are shown below in Figure 4.7. Without any measurement filtering, all estimation errors have initial values stemming directly from the initial state perturbations. In addition, velocity errors produce position errors that increase or decrease accordingly.

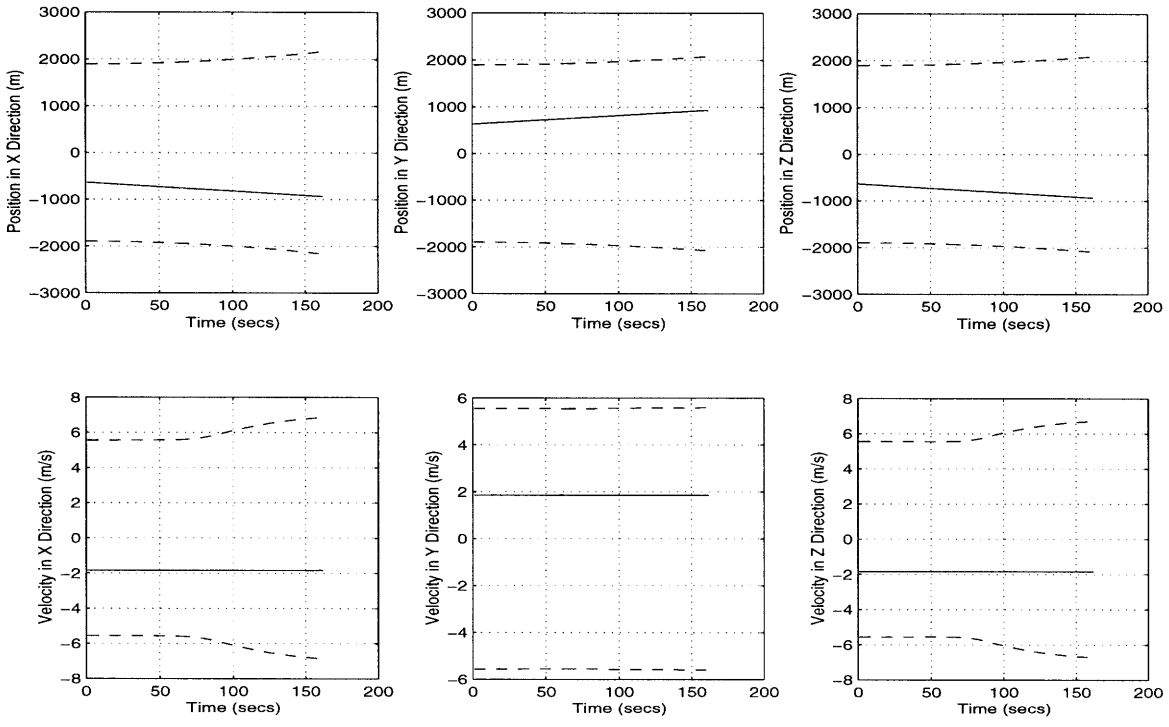

Figure 4.7: No Meas: Lander Estimation Errors with 3σ Boundaries

A curious characteristic shown in these plots is that some of the velocity standard deviations increase sharply after about 80 secs. This is actually unique to the lander velocity

states and is directly due to the accelerometer bias that is added in the lander velocity dynamics. Since the accelerometer bias incorporates acceleration into the lander covariance dynamics, the velocity standard deviations are plotted in comparison to the total (gravitational and non-gravitational) acceleration in Figure 4.8. Indeed, in the case of the X and Z axes, there are distinct impulses in the acceleration components at about the same times that the velocity component standard deviations start to increase sharply. Another interesting feature in this figure is that, although the velocity standard deviation in the Y axis does not vary in time much, it actually decreases in the first 80 seconds. This is due to the nature of the orbital mechanics [5]. In fact, apart from the accelerometer bias, the dynamics of the lander, satellites, or beacons do not contain process noises that ensure their variances will always rise (in the absence of a filtering algorithm, of course).

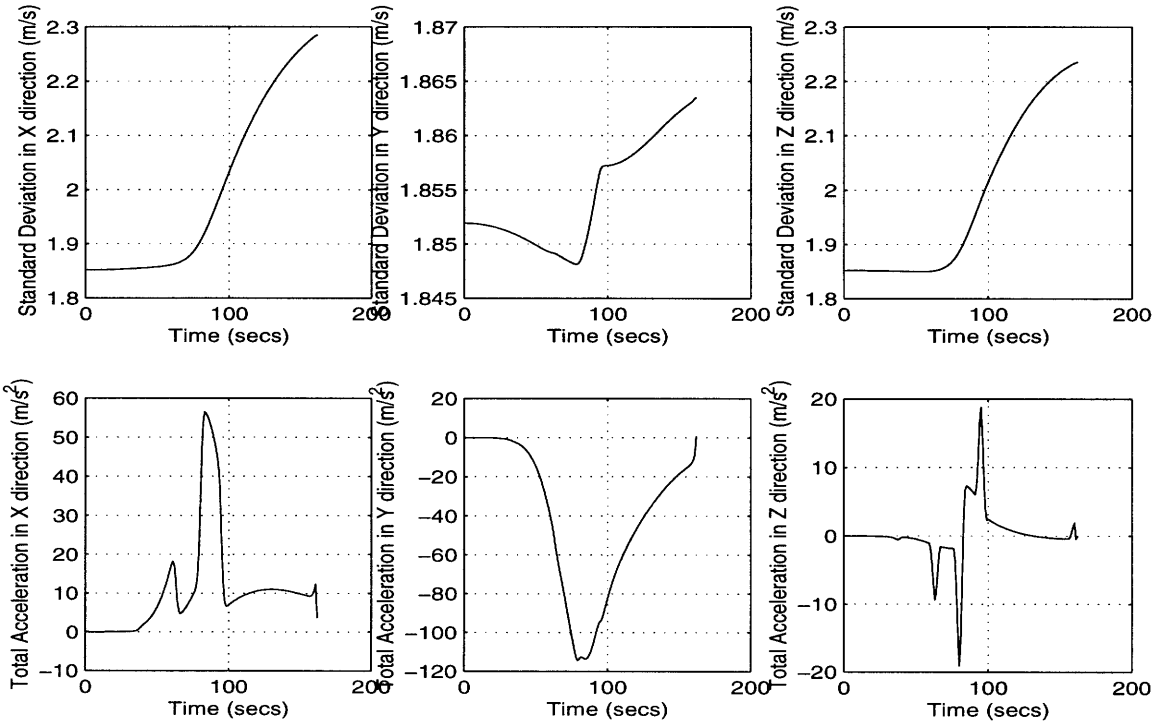

Figure 4.8: No Meas: Lander Velocity Standard Deviations with Total Accelerations

The lander position and velocity standard deviation magnitudes are shown in Figure 4.9. These plots, which also reflect the acceleration-based increases in the lander velocity standard deviations, will be useful in comparison to the other measurement cases in the next sections.

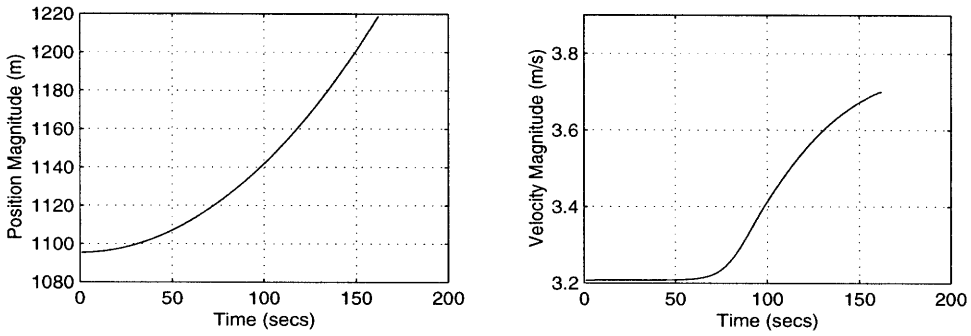

Figure 4.9: No Meas: Lander Standard Deviation Magnitudes

4.3.2 Satellite Range Measurement Case

Four measurement profiles are used to illustrate the performance of the EKF using two-way range measurements with one or more orbiting satellites in view. The positions of the three satellites were chosen so that their ranges with the lander would be predominantly in one axis: Satellite 1 with the X axis, Satellite 2 with the Y axis, and Satellite 3 in the Z axis. Thus, the first three measurement profiles address range measurements with each of the three satellites. The fourth measurement profile incorporates range measurements with all three satellites. Table 4.1 on page 77 compares the final lander standard deviations of the four simulations.

For the first satellite range simulation (range measurement with Satellite 1), estimation errors with 3σ bounds of the lander and Satellite 1 are shown in Figures 4.10 and 4.11, respectively. With this measurement, the filter affects the lander position state results in

the X direction most of all, whose estimation error is immediately driven to near zero and whose standard deviation is rapidly decreased. The lander X-velocity estimation error shows the same effects although not quite as quickly as its position counterpart. These results are very reasonable, as the range vector between the lander and Satellite 1 has its largest component in the X direction. The range vector also has a significant Y component, and the filter does correct the corresponding estimation errors, but is not as successful as it is with the X direction states. In addition, the range has practically no Z axis component, and likewise, the filter has no effect on Z axis estimation errors. In addition, the filter has no appreciable effect on satellite estimation errors and standard deviations. This is because the satellite initial standard deviations are much smaller than those of the lander and, thus, are much less sensitive to filtering.

The position and velocity standard deviation magnitudes of the lander and Satellite 1 for this measurement case and the no measurement case are compared in Figure 4.12. The initial drop in the lander position magnitude is clearly displayed, while the velocity position magnitude is still susceptible to the effects of the accelerometer bias. The standard deviation magnitudes for the satellite also show that the filter has limited influence on these states.

Estimation errors of the lander and satellite range biases (in units of metres), along with 1σ and 3σ boundaries, are graphed in Figure 4.13. This figure shows that both estimation errors are predominantly kept within 1σ and never stray outside of 3σ. Thus, using a range bias time constant of 1.5 seconds, the estimation errors of the range biases are well bounded. Since all biases are modeled in the same fashion, bias estimation errors will only be shown for one singular satellite or beacon case per measurement type.

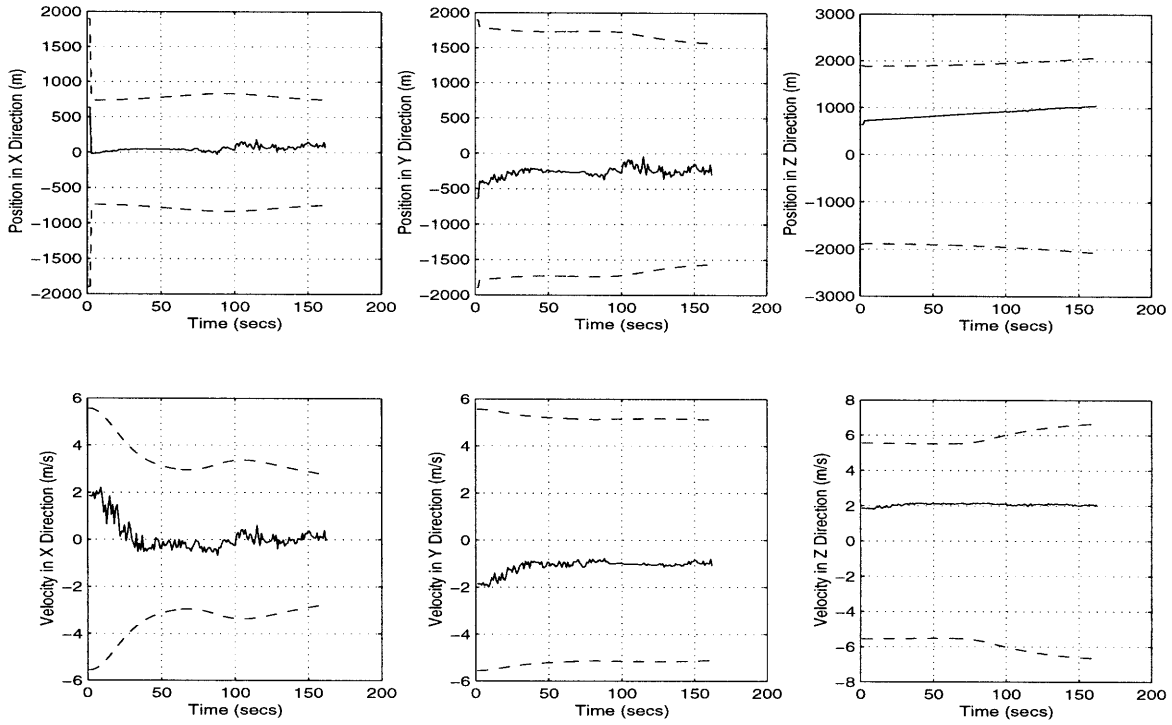

Figure 4.10: Sat1 Range Meas: Lander Estimation Errors with 3σ Boundaries

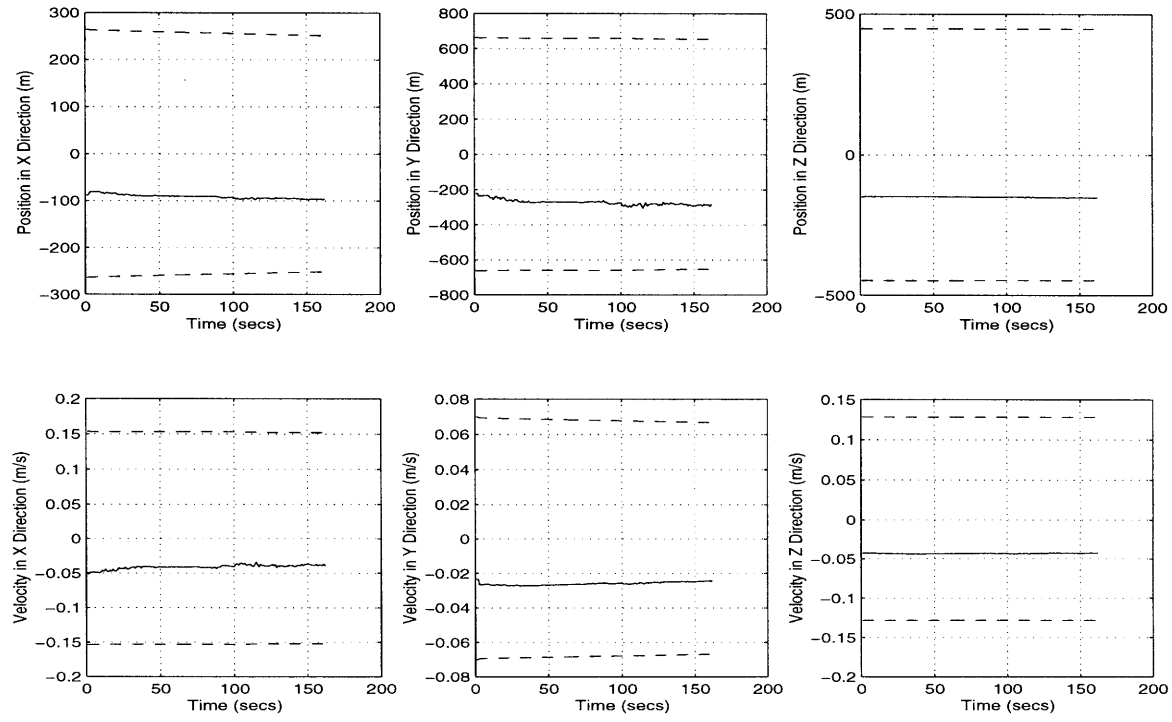

Figure 4.11: Sat1 Range Meas: Satellite 1 Estimation Errors with 3σ Boundaries

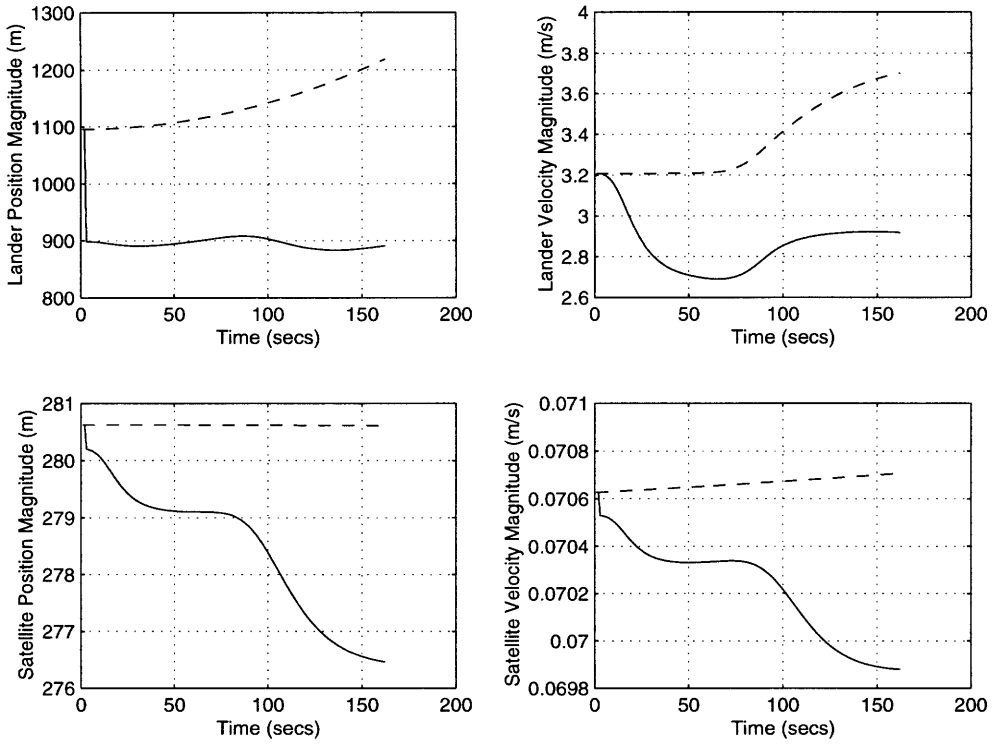

Figure 4.12: Sat1 Range Meas: Lander and Satellite Standard Deviation Magnitudes

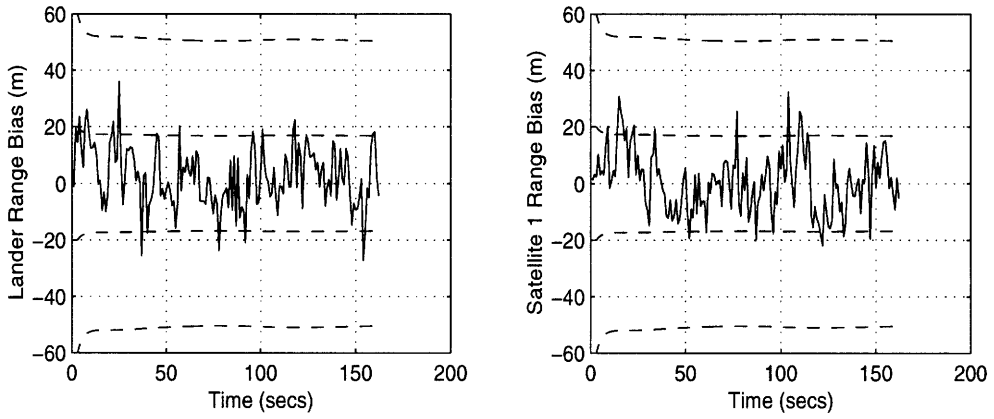

Figure 4.13: Sat1 Range Meas: Range Bias Estimation Errors with 1σ/3σ Bounds

The next two simulations involve range measurements with Satellite 2 and Satellite 3, which lie predominantly in the Y and Z directions, respectively. For the simulation involving Satellite 2, estimation errors with 3σ bounds of the lander and Satellite 2 are shown in Figures 4.14 and 4.15, respectively. Position and velocity standard deviations of the lander

and Satellite 2 are shown in Figure 4.16. Likewise, for the simulation involving Satellite 3, estimation errors with 3σ bounds of the lander and Satellite 3 are shown in Figures 4.17 and 4.18, respectively. Position and velocity standard deviations of the lander and Satellite 3 are shown in Figure 4.19.

The results shown in these figures are consistent with the results of the Satellite 1 range simulation. Again, the filter is most effective on the lander position (and velocity) state in the direction of the largest range component. In addition, the filter does not hold much influence on the satellite states. Regarding the standard deviation magnitudes of the lander, the filter is efficient in minimizing the position magnitude immediately while the velocity magnitude gradually reaches a minimum at approximately 60 to 70 secs. After these times, the magnitudes increase due to biases (chiefly the accelerometer bias) but the filter does not allow them to increase faster than the magnitudes of the no measurement case. While the filter is fighting off these unwanted increases, it is able to further minimize the position and velocity standard deviation magnitudes of the respective satellite, which are not governed by process noise. This lack of process noise in the satellite dynamics, coupled with orbital mechanical behavior, may actually permit the satellite standard deviation magnitudes to decrease slightly, even without measurement filtering, as is the case with Satellite 2 and Satellite 3.

One key peculiarity in these plots is that the relevant lander estimation errors for the Satellite 2 and 3 simulations have noticeable biases. However, close examination of the Kalman gain matrices $\underline{K}_k$ at each measurement pass reveal that the filter is accountable for 23 states (6 lander states, 6 satellite states, 2 range bias states, and 9 lightly weighted IMU bias states), which is a lot to handle for scalar measurements. In fact, this is a warning that the lander estimation errors are susceptible to biases with range measurement filtering.

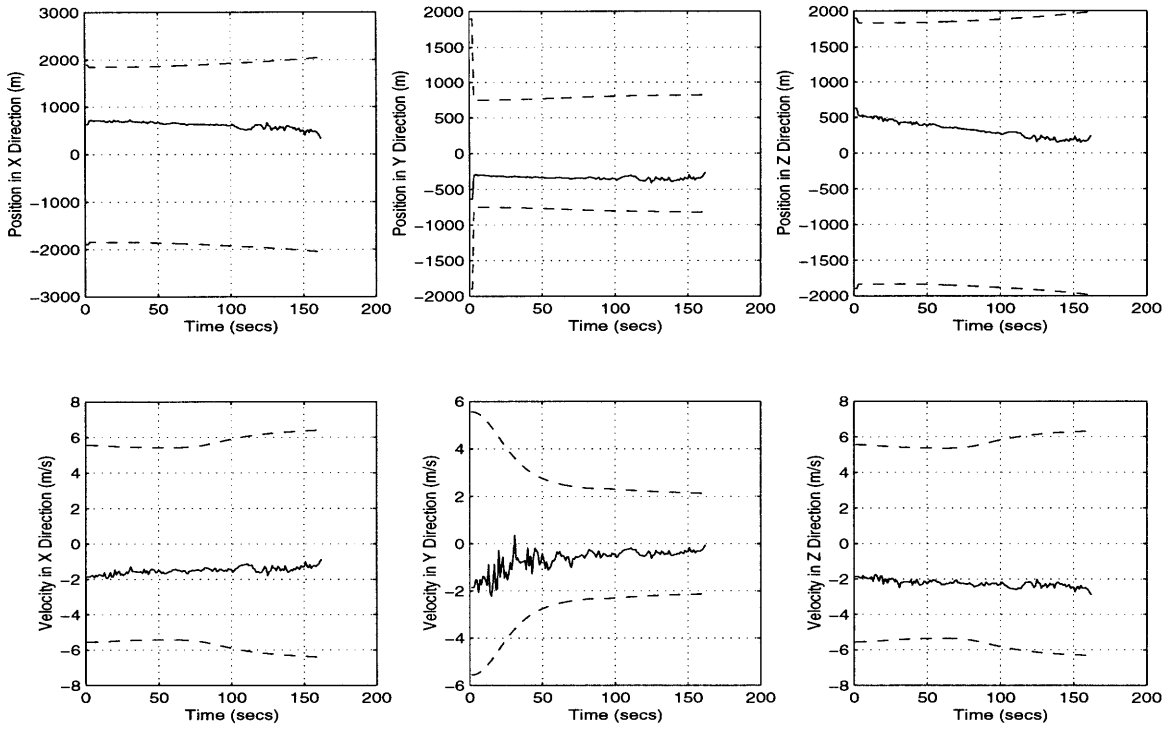

Figure 4.14: Sat2 Range Meas: Lander Estimation Errors with 3σ Boundaries

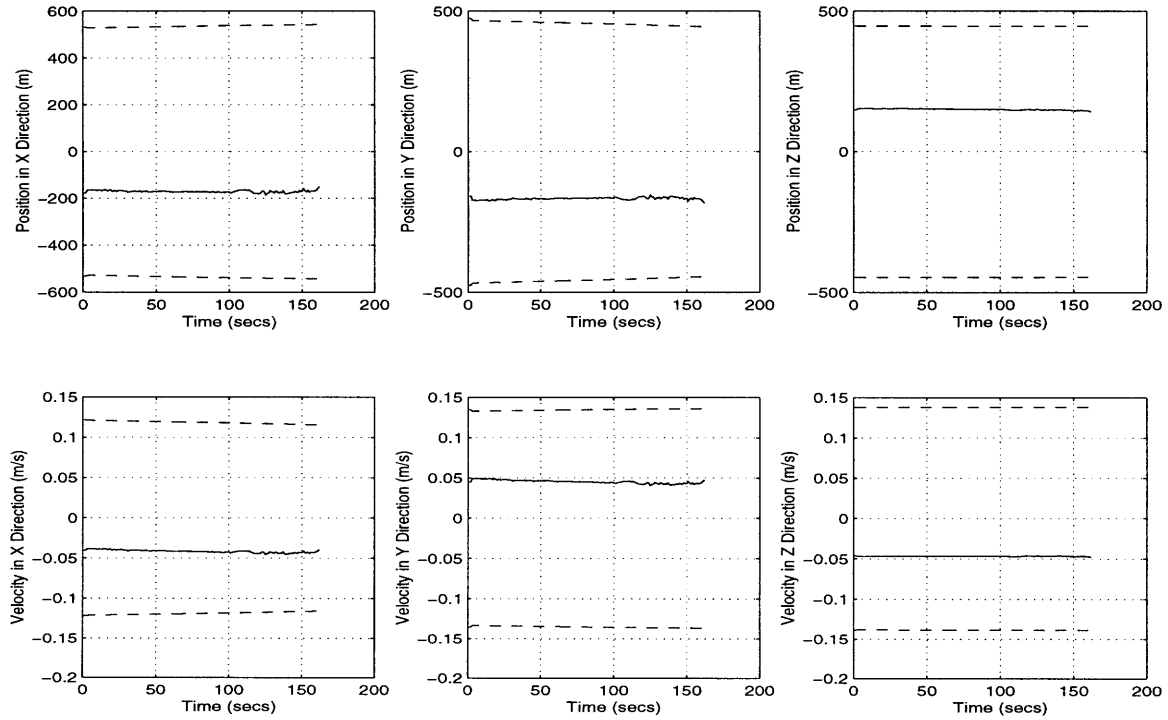

Figure 4.15: Sat2 Range Meas: Satellite 2 Estimation Errors with 3σ Boundaries

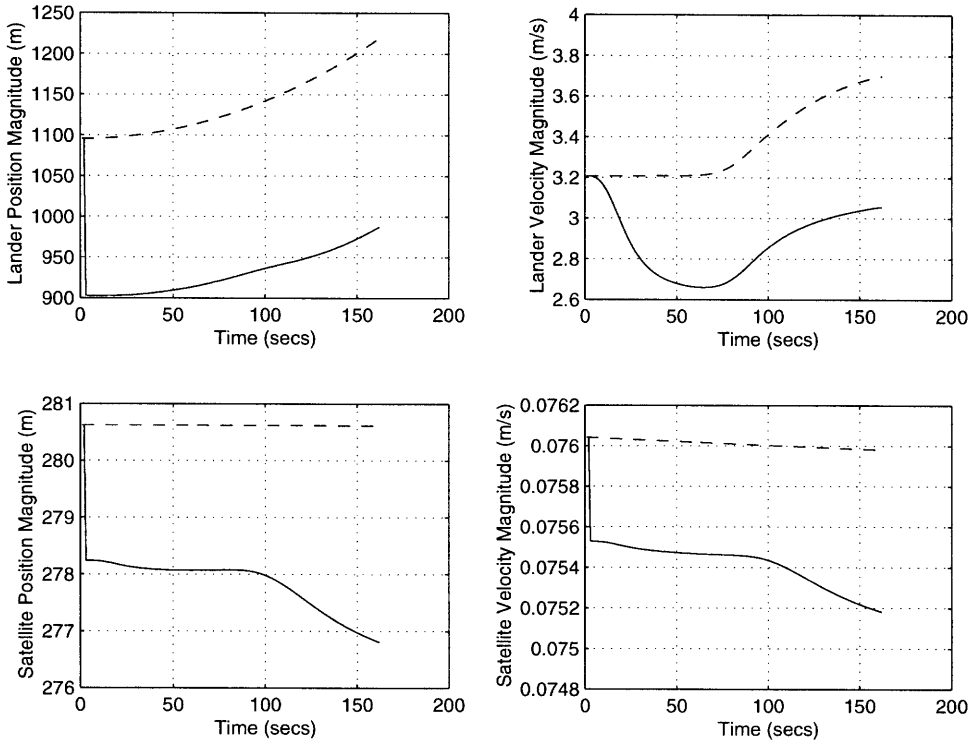

Figure 4.16: Sat2 Range Meas: Lander and Satellite Standard Deviation Magnitudes

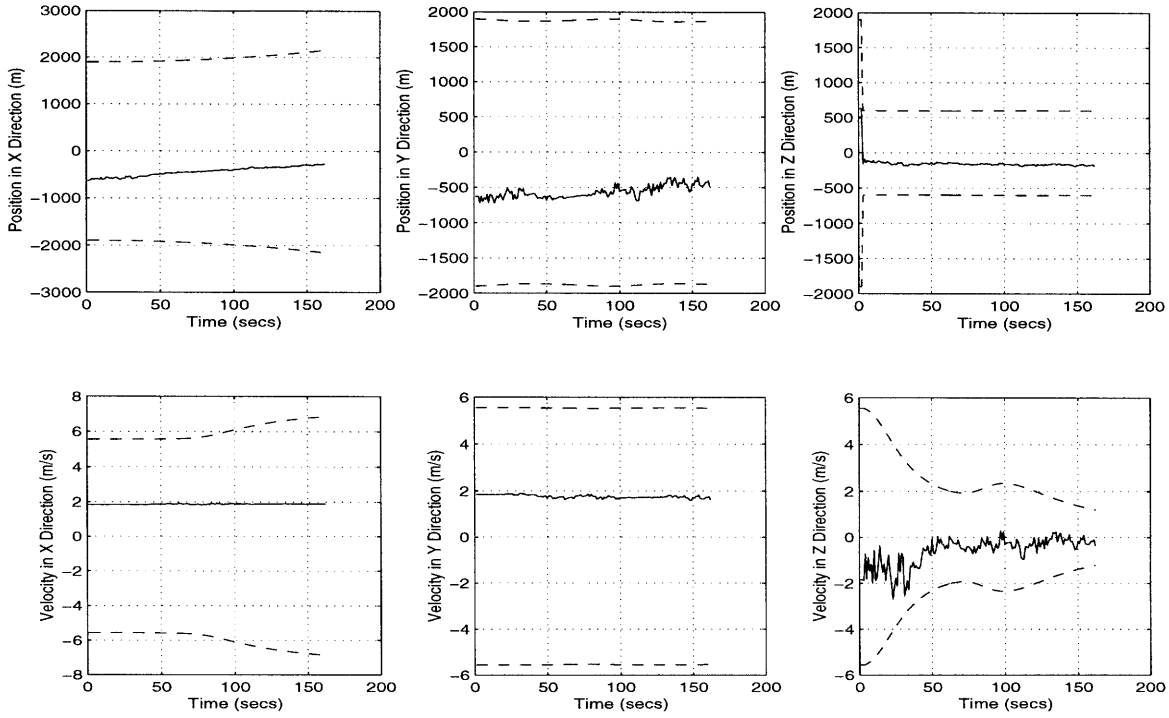

Figure 4.17: Sat3 Range Meas: Lander Estimation Errors with 3σ Boundaries

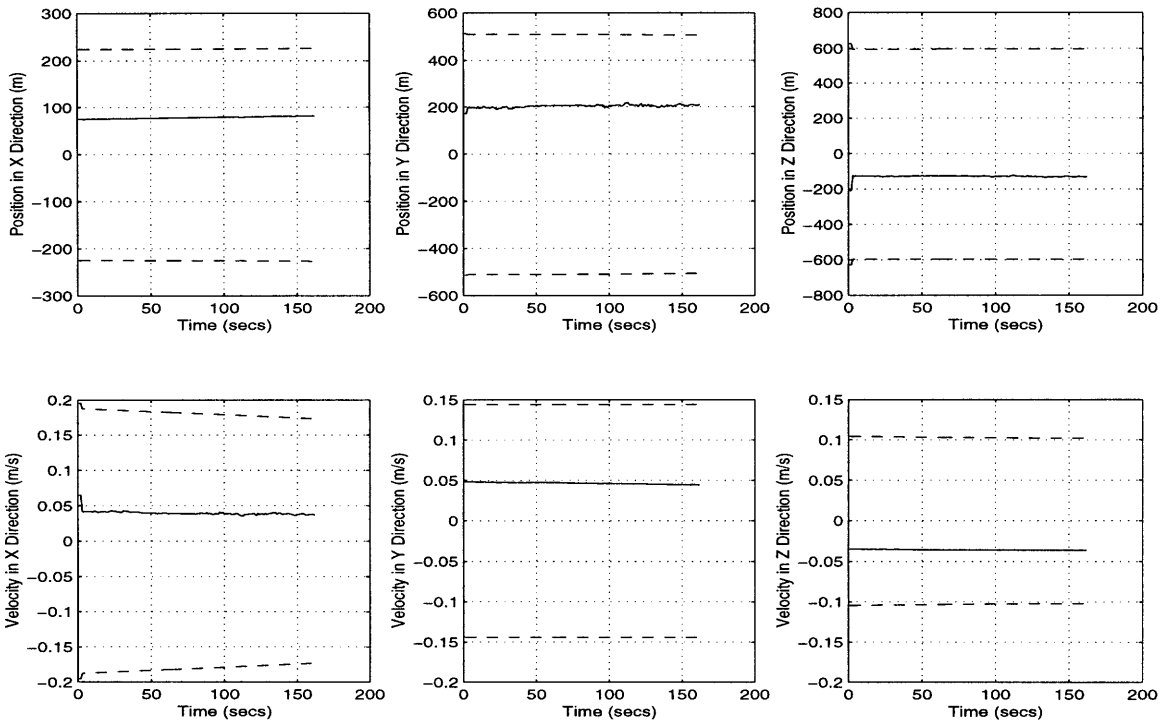

Figure 4.18: Sat3 Range Meas: Satellite 3 Estimation Errors with 3σ Boundaries

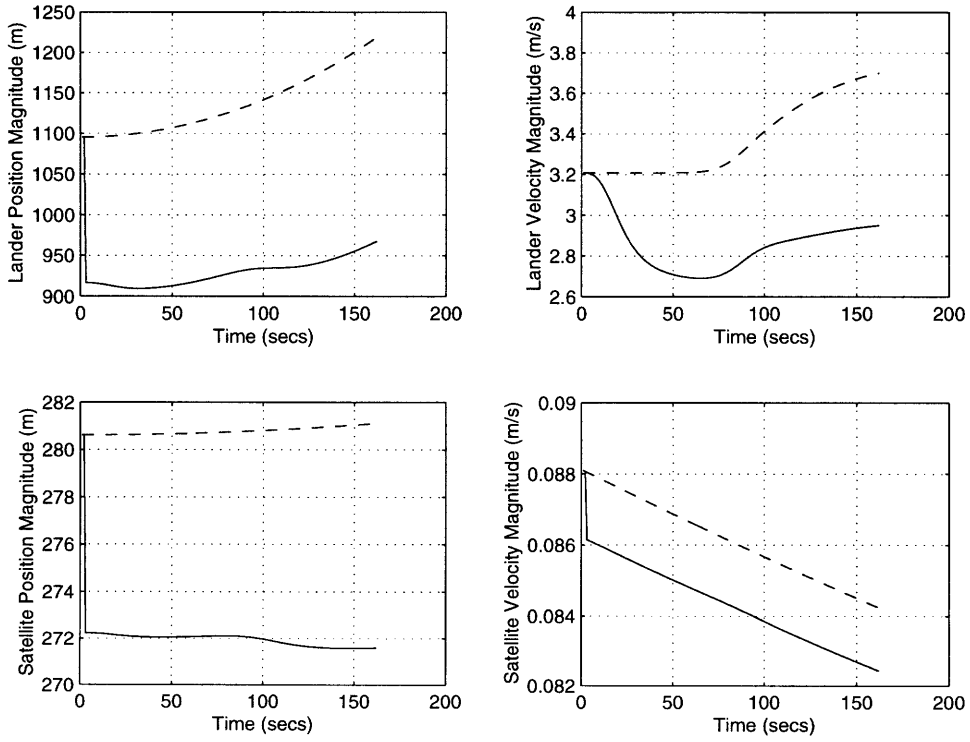

Figure 4.19: Sat3 Range Meas: Lander and Satellite Standard Deviation Magnitudes

The last satellite range simulation takes measurements with all three satellites. The results are displayed below: Figures 4.20 to 4.23 illustrate the estimation errors of the lander, Satellite 1, Satellite 2, and Satellite 3, respectively, while Figure 4.24 shows the standard deviation magnitudes of the spacecrafts. Finally, the estimation errors for the range bias of each spacecraft are found in Figure 4.25.

After three consecutive range measurement processes in the EKF, the lander standard deviations (and likewise, the variances) have decreased in each direction. The estimation errors still reveal biases in the lander position states, but these biases remain well within the 3σ bounds. Otherwise, the amplitudes of the lander velocity estimation error transients in Figure 4.20 look to be a little larger than those of the singular range measurement cases. This is because they contain measurement noises from three sources (the three measurements) instead of one.

The lander standard deviation magnitudes also have large decreases, since the filter is able to contribute to the minimization in three directions, rather than one. This, in fact, does not allow the magnitudes to undergo (large) increases at any time. In contrast, the singular cases would tend to decrease the standard deviations in one direction, while the standard deviations in the other two directions would be largely unaffected. However, the velocity standard deviations are always affected by accelerometer bias increases but, for this particular case, the filter is better able to control these increases, as shown in Figure 4.24.

Once again, satellite estimation errors are not greatly influenced by the filter, regardless of the number of range measurements processed. However, as the filter takes additional range measurements, their standard deviations do decrease slightly more, although not to the degree of the lander standard deviations.

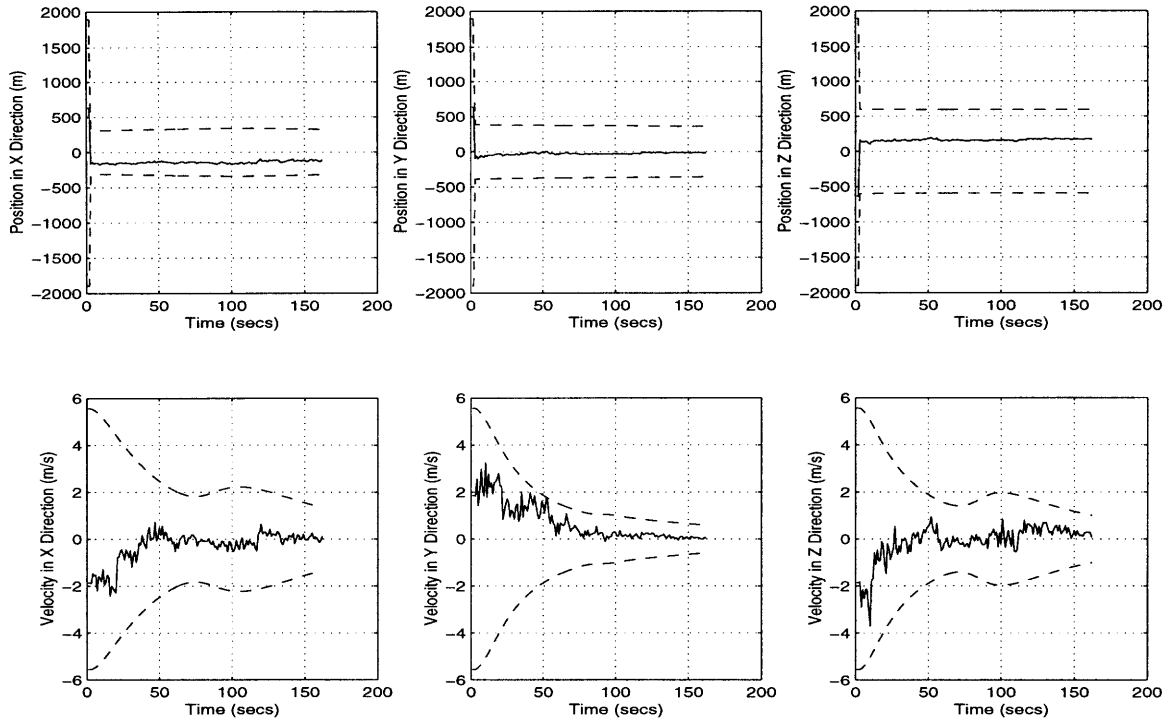

Figure 4.20: All Sat Rng Meas: Lander Estimation Errors with 3σ Boundaries

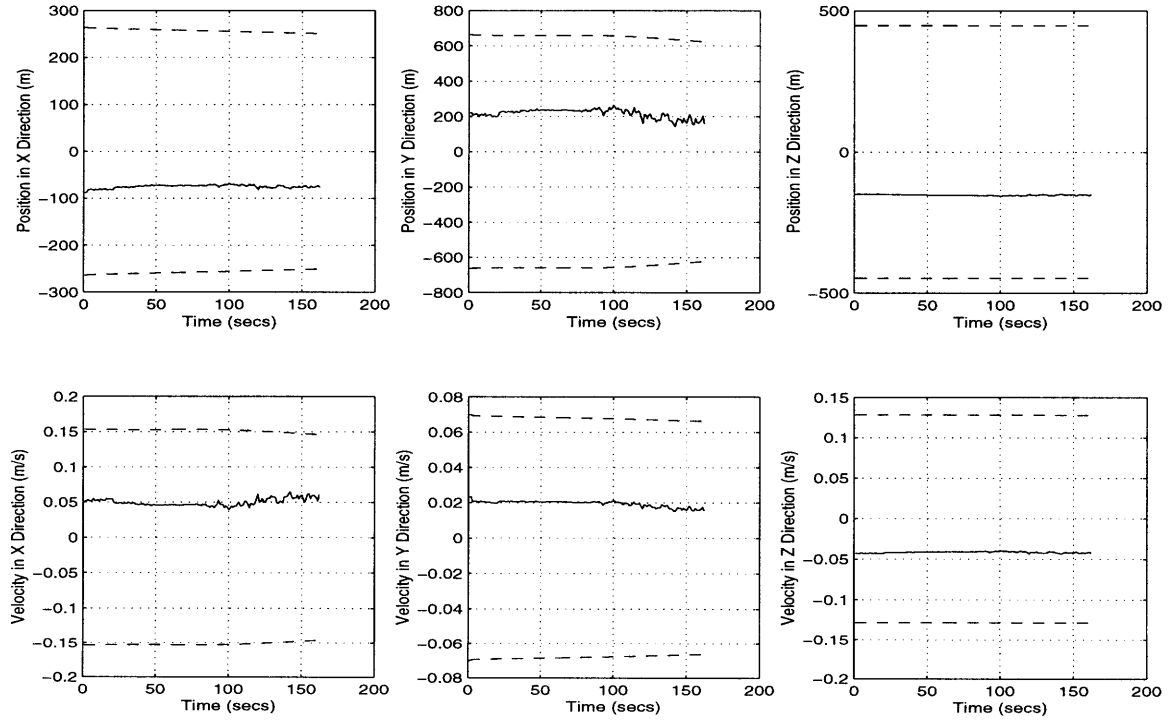

Figure 4.21: All Sat Rng Meas: Satellite 1 Estimation Errors with 3σ Boundaries

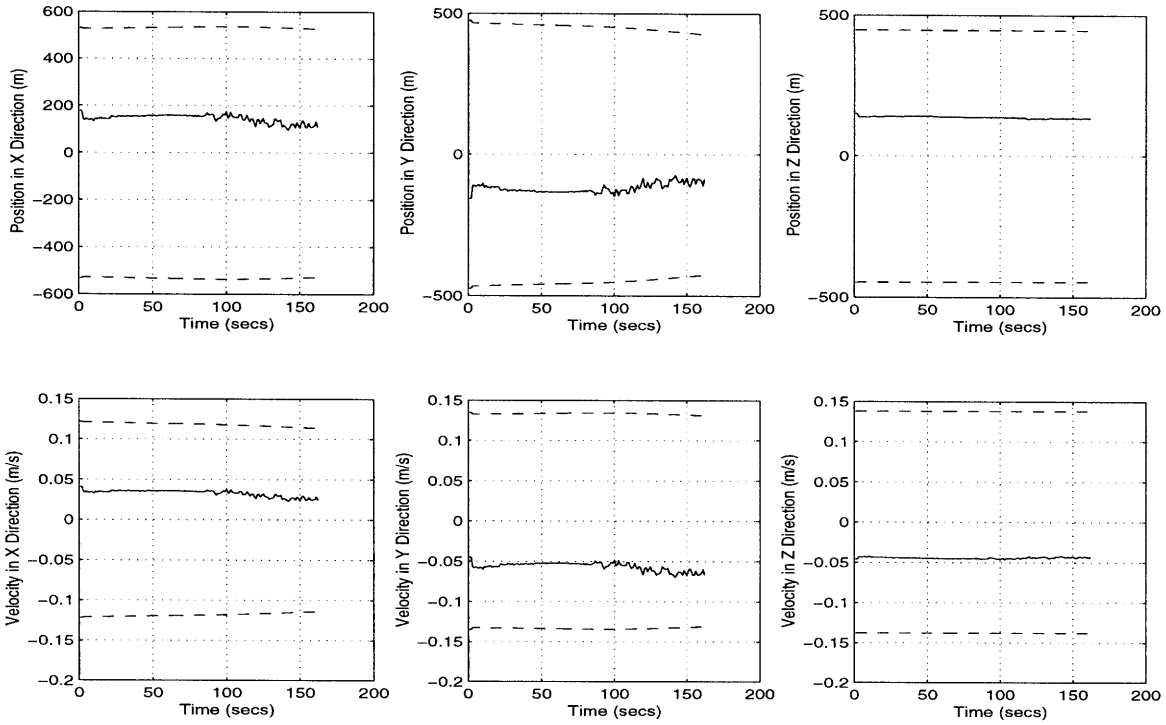

Figure 4.22: All Sat Rng Meas: Satellite 2 Estimation Errors with 3σ Boundaries

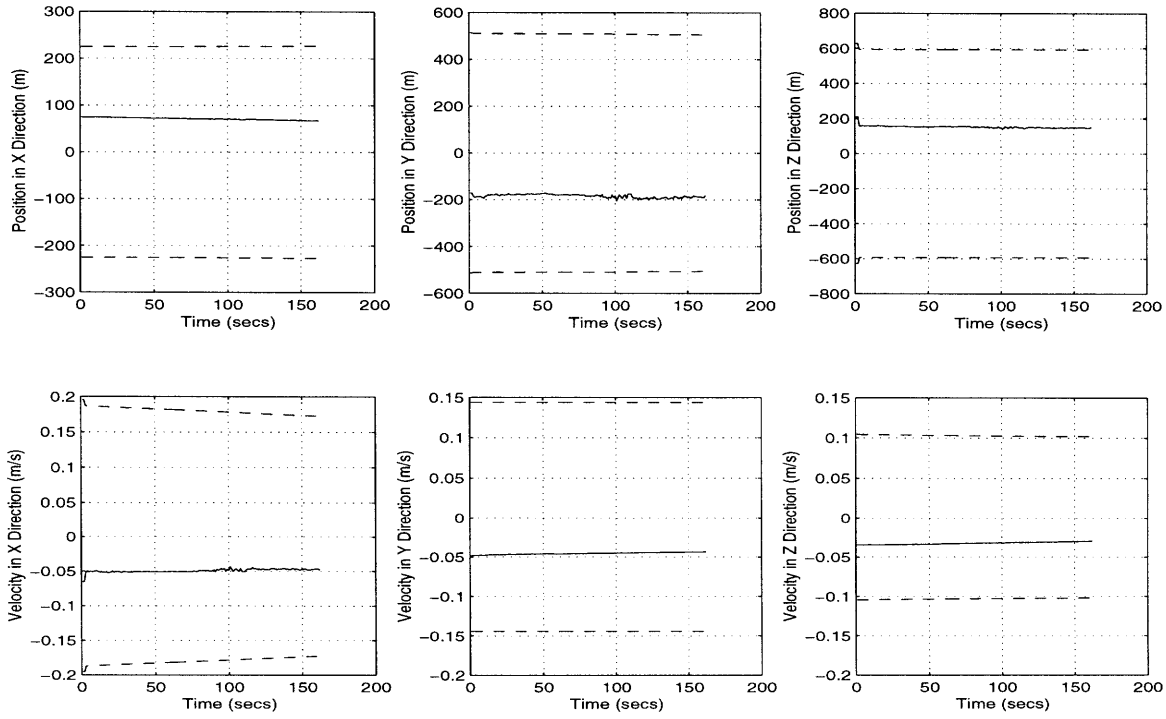

Figure 4.23: All Sat Rng Meas: Satellite 3 Estimation Errors with 3σ Boundaries

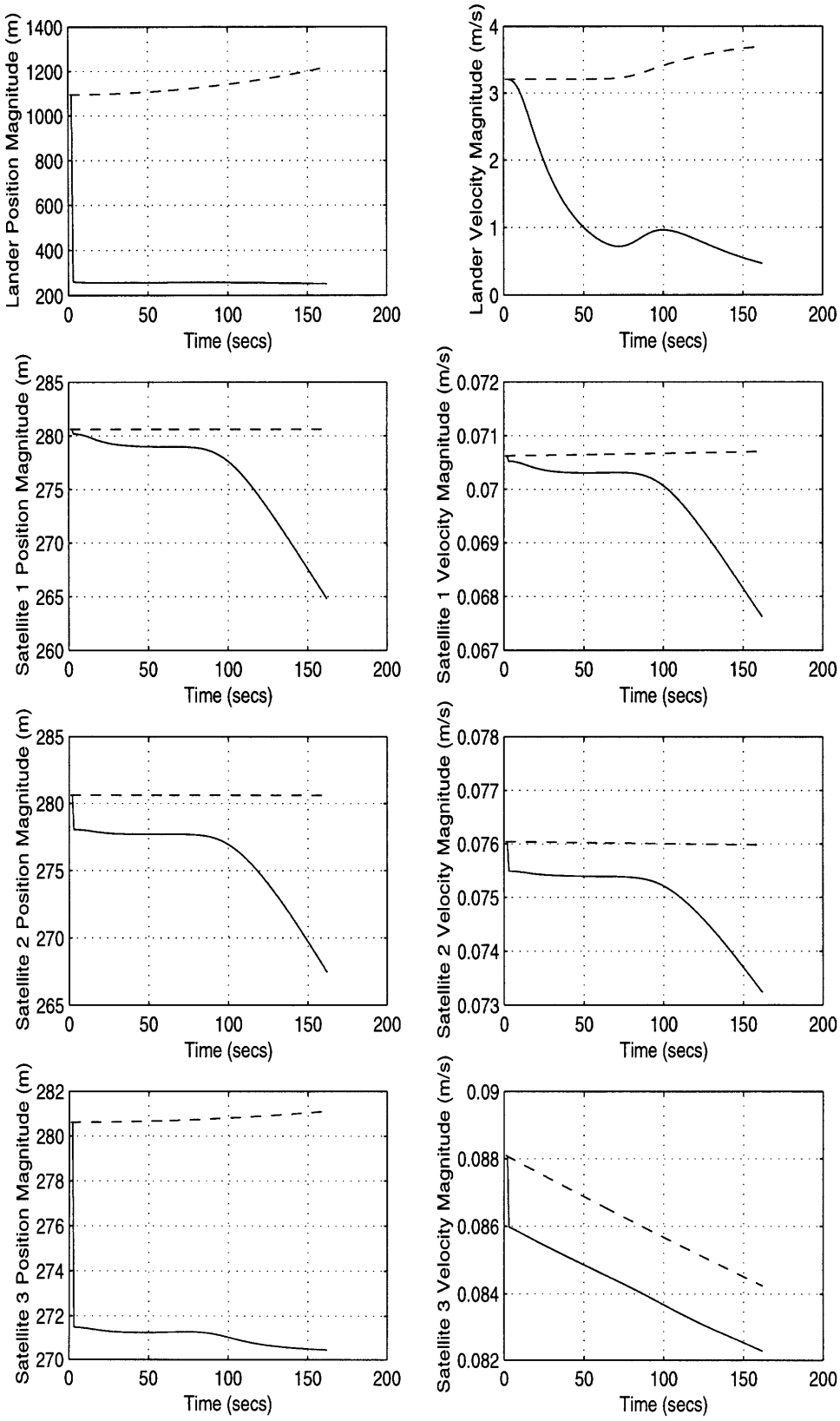

Figure 4.24: All Sat Rng Meas: Standard Deviation Magnitudes

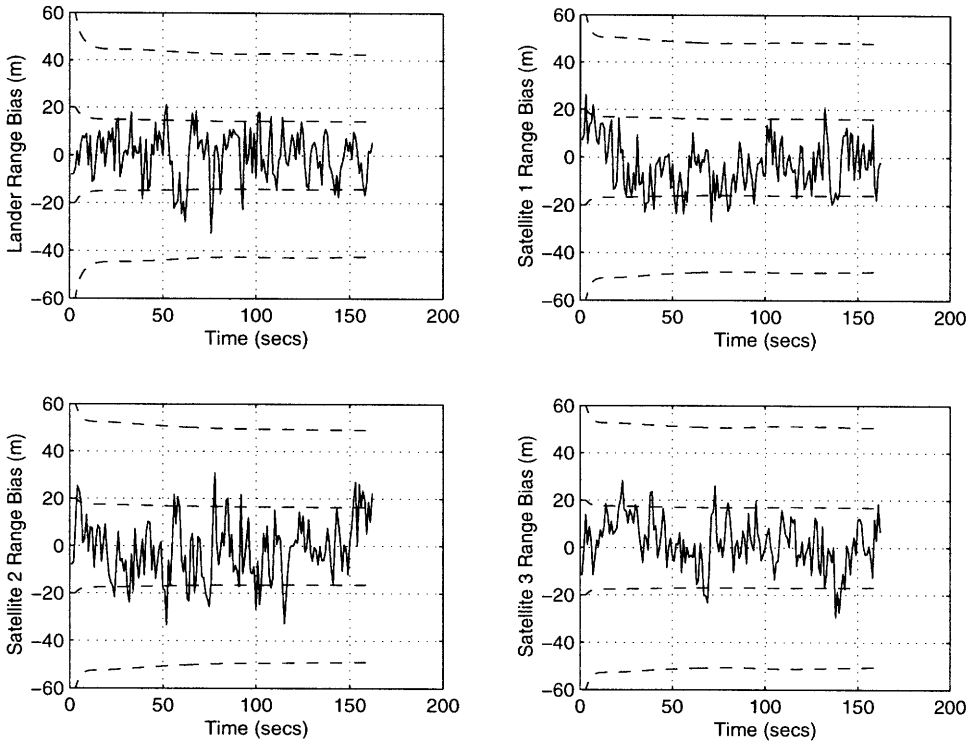

Figure 4.25: All Sat Rng Meas: Range Bias Estimation Errors with 1σ/3σ Bounds

The range bias estimation errors with 1σ and 3σ bounds for the lander and the navigation satellites are shown above in Figure 4.25. Like those of the single satellite range measurement case in Figure 4.13, these estimation errors are well bounded; they are predominantly kept within 1σ and never stray outside of 3σ.

Table 4.1 compares the final lander state standard deviations of the no measurement case against all four range measurement cases. Of all the cases, the best results belong to the measurement profile using all three satellites. In addition, minimizations in position and velocity standard deviations in one axis are well illustrated in the single satellite case results. Furthermore, it is notable to mention that the minimum position value of all single satellite cases is the Z axis position in the Satellite 3 case, because the range vector between the lander and Satellite 3 lies more directly on the Z axis than any of the other range vectors.

Lander State Std. Dev.	Measurement Profile (Range Measurements)				
	No Meas	Satellite 1	Satellite 2	Satellite 3	All Sats
X Position	721.3008 m	241.0250 m	681.1316 m	717.3309 m	103.6851 m
Y Position	692.3987 m	508.2495 m	272.0762 m	617.8812 m	117.8582 m
Z Position	697.0675 m	691.1518 m	660.7988 m	199.8766 m	197.0611 m
X Velocity	2.2852 m/s	0.8784 m/s	2.1160 m/s	2.2828 m/s	0.3429 m/s
Y Velocity	1.8635 m/s	1.6827 m/s	0.7038 m/s	1.8356 m/s	0.1615 m/s
Z Velocity	2.2351 m/s	2.2145 m/s	2.0892 m/s	0.3447 m/s	0.2755 m/s

Table 4.1: Final Lander Standard Deviations for Range Measurement Profiles

4.3.3 Satellite Doppler Measurement Case

EKF performance analysis of two-way Doppler measurements with satellites is presented in this section. The simulation is ran with four measurement profiles: Doppler measurements with Satellite 1, Satellite 2, Satellite 3, and all satellites. The final lander state standard deviations of the four simulations as well as the no measurement simulation are collected in Table 4.2 on page 89.

The results of the first simulation (Doppler measurement with Satellite 1) in Figures 4.26 to 4.29 show many similarities between range measurements and Doppler measurements. The filter is most effective on lander velocity states and in the axis of the largest range vector component (in this case, the X axis), as shown in Figure 4.26. In addition, Figure 4.27 reveals that the filter has limited effect on the satellite states.

In addition, the measurement sensitivity ($\underline{H}_k$) model in Section 2.5.2 dictates that the velocity state entries in the measurement sensitivity matrix are dependent on the range vector components and the position state entries are dependent on the delta-range (Doppler) vector components. Thus, the lander position standard deviation is reduced much

more in the Y axis than in the other axes. Furthermore, the position estimation errors are not greatly affected (as the biases from the initial perturbations remain), revealing that satellite Doppler measurement filtering does not affect position states as powerfully as velocity states.

Figure 4.29 displays the Doppler bias estimation errors with 1σ and 3σ bounds (in units of metres per second) for the lander and Satellite 1. These bias estimation errors are well bounded; they are predominantly kept within 1σ and never stray outside of 3σ. It is reminded that the time constant used for the Doppler dynamics is 1.6 seconds.

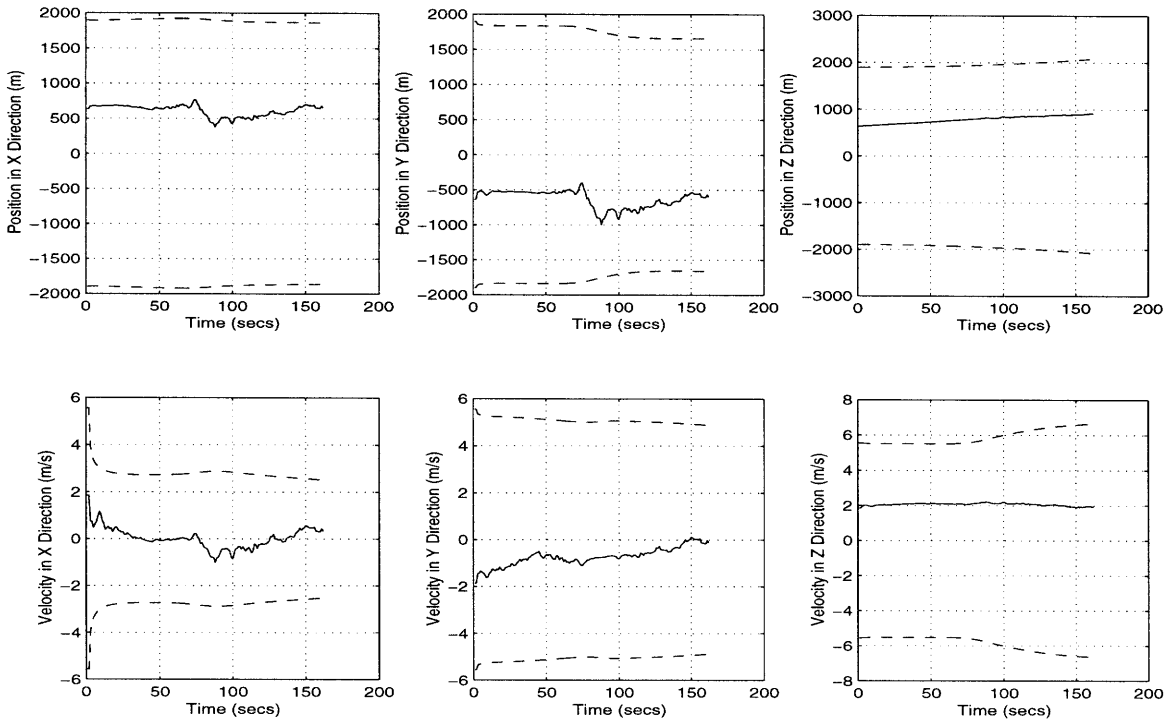

Figure 4.26: Sat1 Doppler Meas: Lander Estimation Errors with 3σ Boundaries

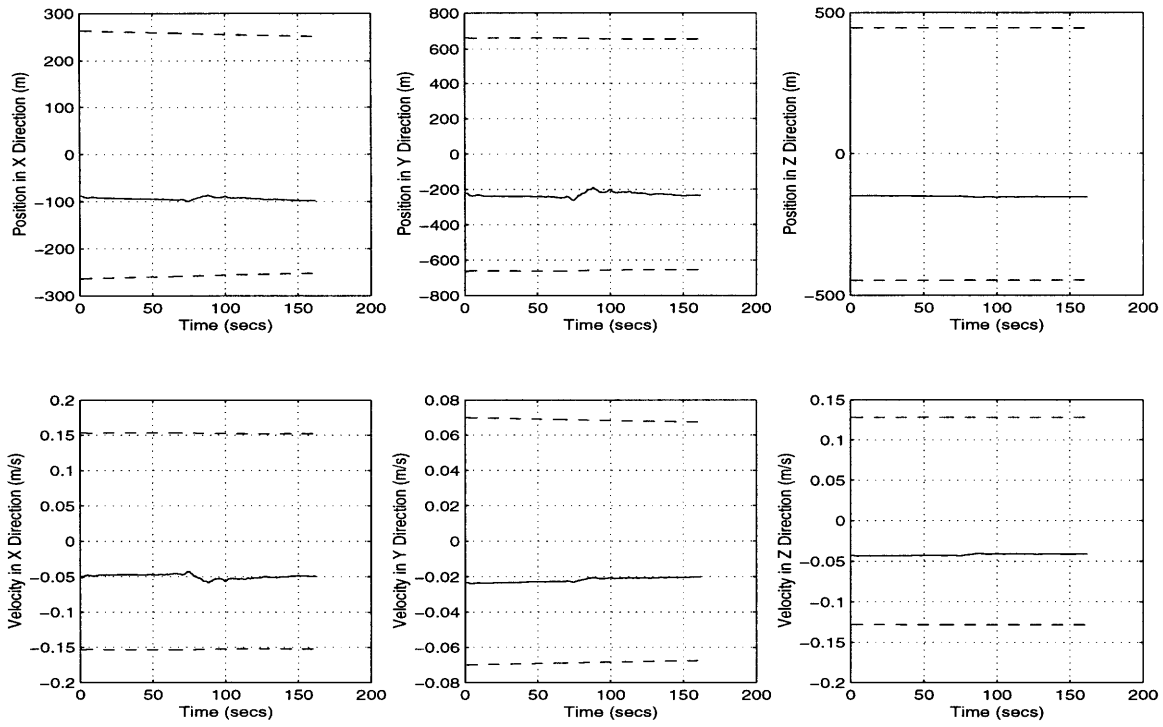

Figure 4.27: Sat1 Doppler Meas: Satellite 1 Estimation Errors with 3σ Boundaries

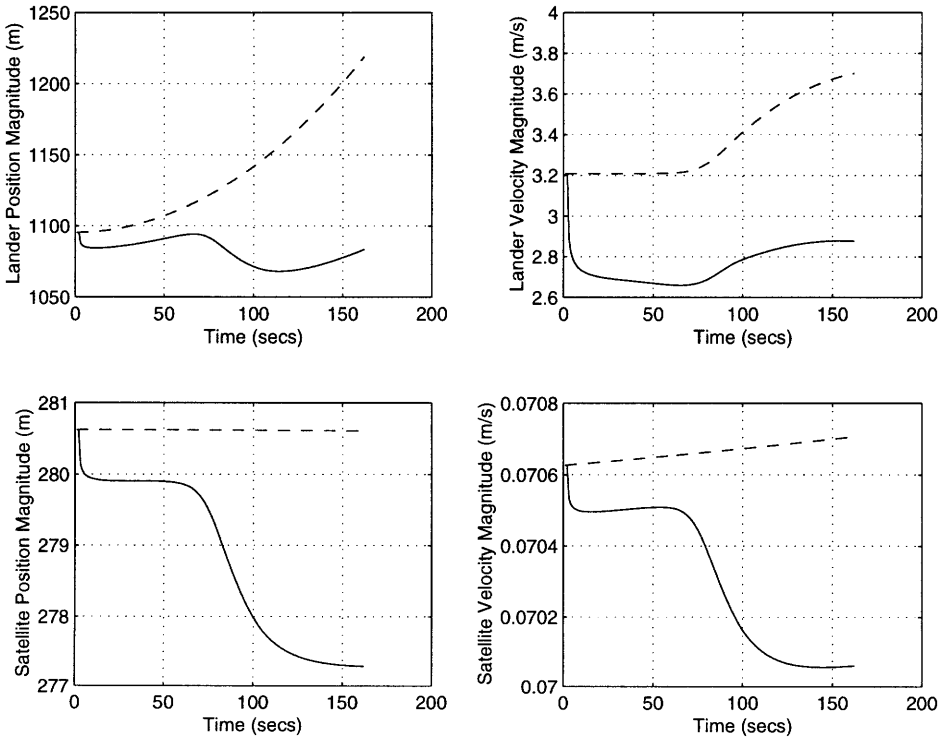

Figure 4.28: Sat1 Doppler Meas: Lander and Satellite Std. Deviation Magnitudes

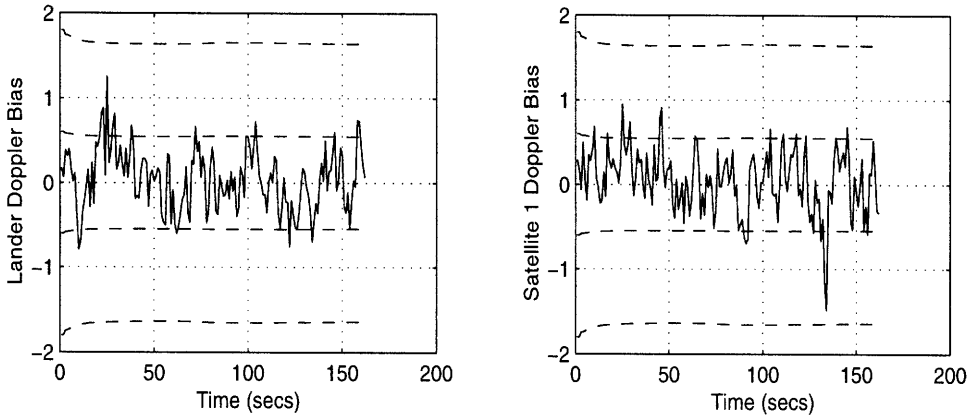

Figure 4.29: Sat1 Doppler Meas: Doppler Bias Estimation Errors with 1σ/3σ Bounds

The results of the simulations using Doppler measurements with Satellite 2 and with Satellite 3 are presented in Figures 4.30 to 4.35. Once again, the lander velocity estimation errors and standard deviations, in Figures 4.30 and 4.33, are most affected in the axis of the largest range component. However, in both simulations, the lander position estimation errors and standard deviations display minimal effects from the filter in all axes. The lander position standard deviation magnitudes in Figures 4.32 and 4.35 also exhibit these minimal responses. Thus, in general, singular satellite Doppler measurement filtering cannot be relied upon to improve knowledge of the lander position states. Finally, the satellite estimation errors and standard deviations also illustrate limited effects from the filter, which is consistent with the Doppler filtering results for Satellite 1 (and all range filtering results, for that matter).

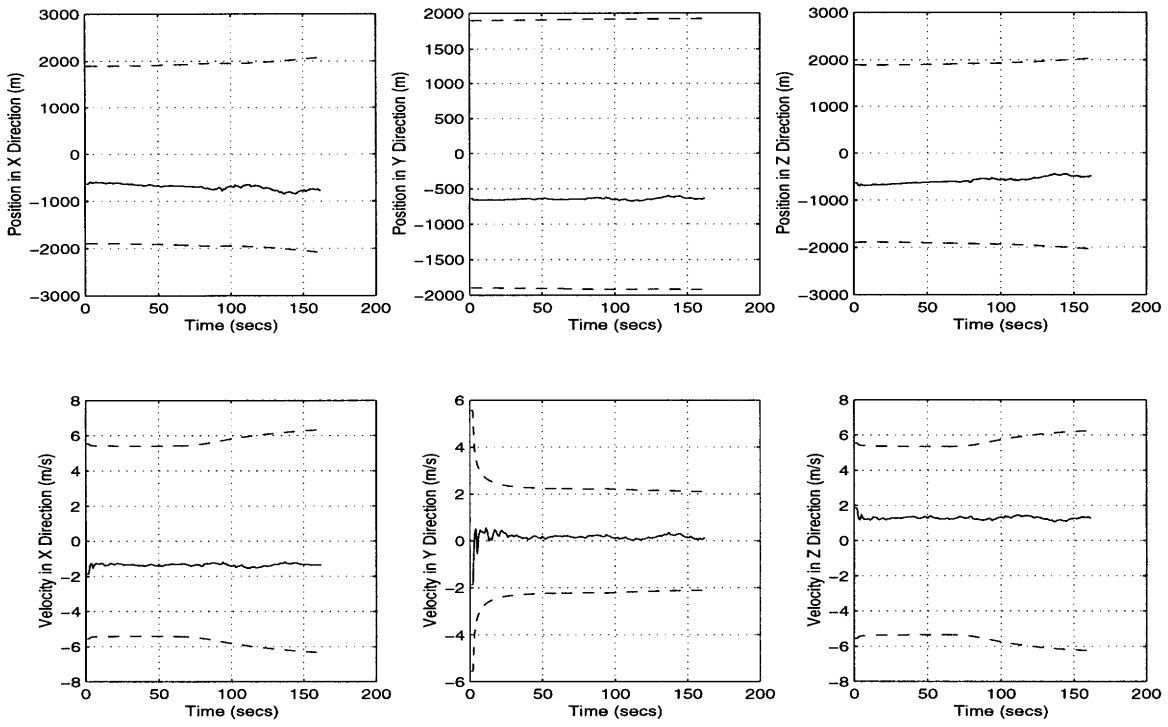

Figure 4.30: Sat2 Doppler Meas: Lander Estimation Errors with 3σ Boundaries

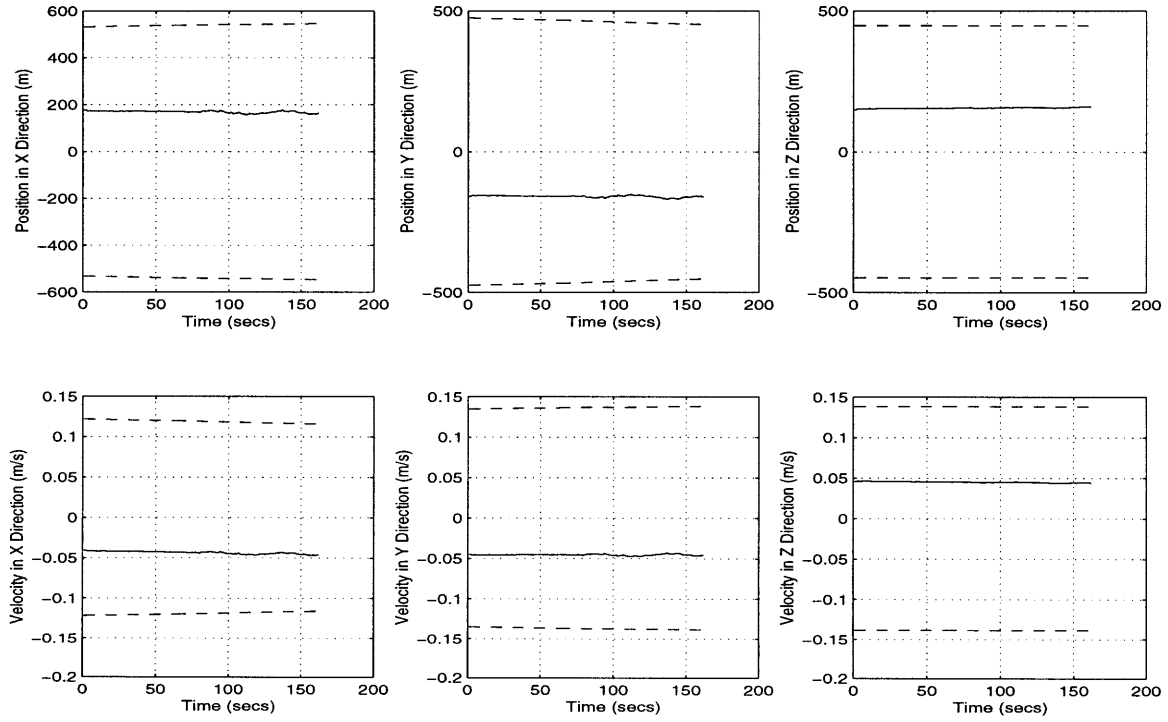

Figure 4.31: Sat2 Doppler Meas: Satellite 2 Estimation Errors with 3σ Boundaries

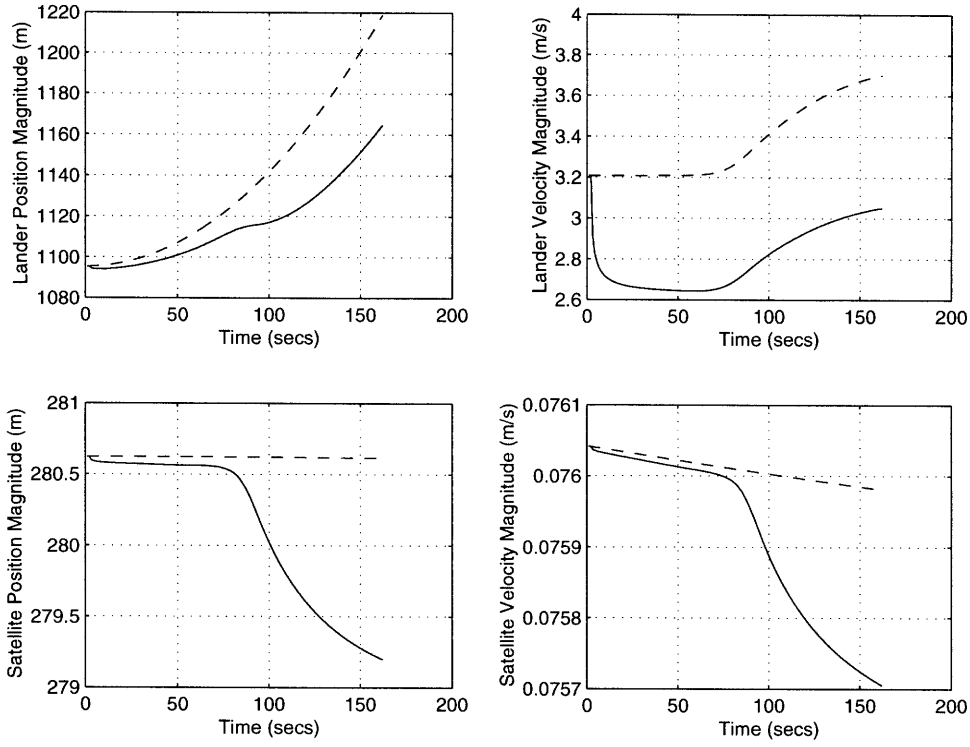

Figure 4.32: Sat2 Doppler Meas: Lander and Satellite Std. Deviation Magnitudes

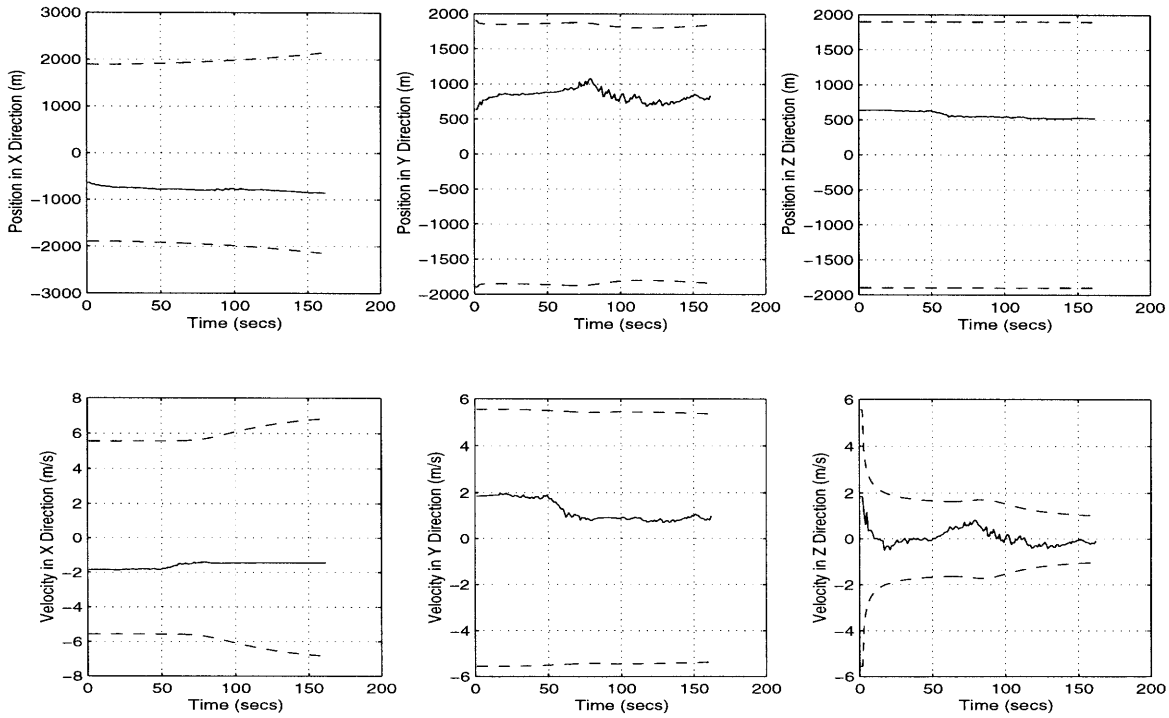

Figure 4.33: Sat3 Doppler Meas: Lander Estimation Errors with 3σ Boundaries

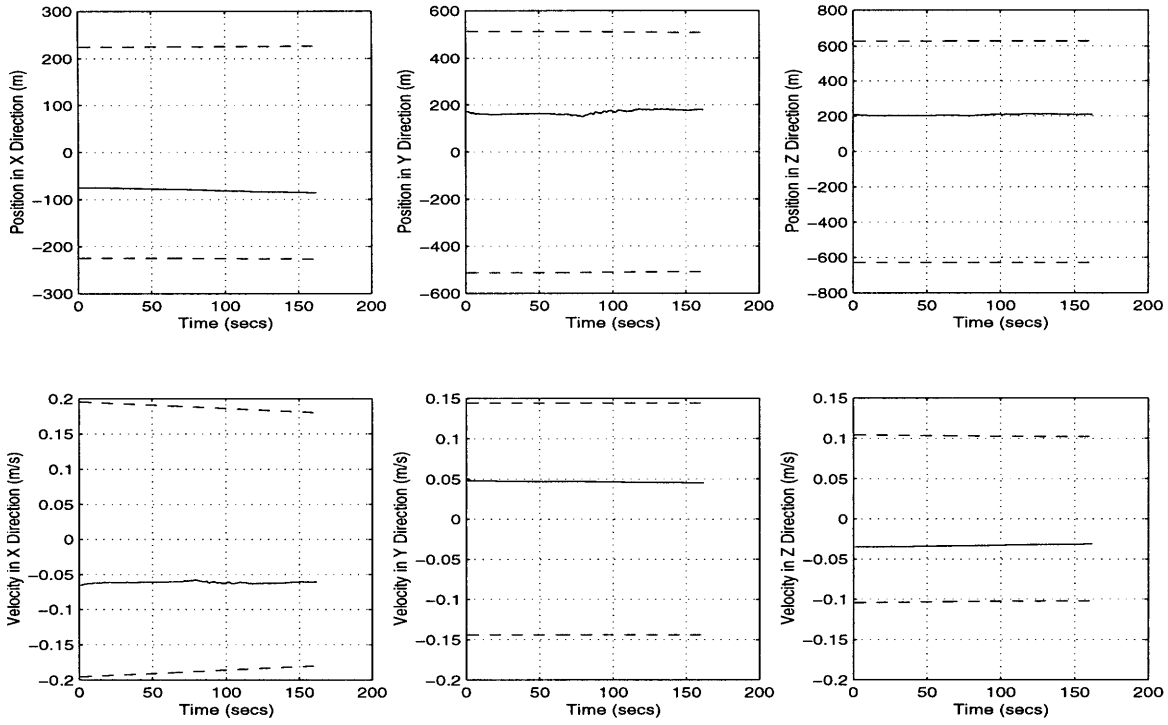

Figure 4.34: Sat3 Doppler Meas: Satellite 3 Estimation Errors with 3σ Boundaries

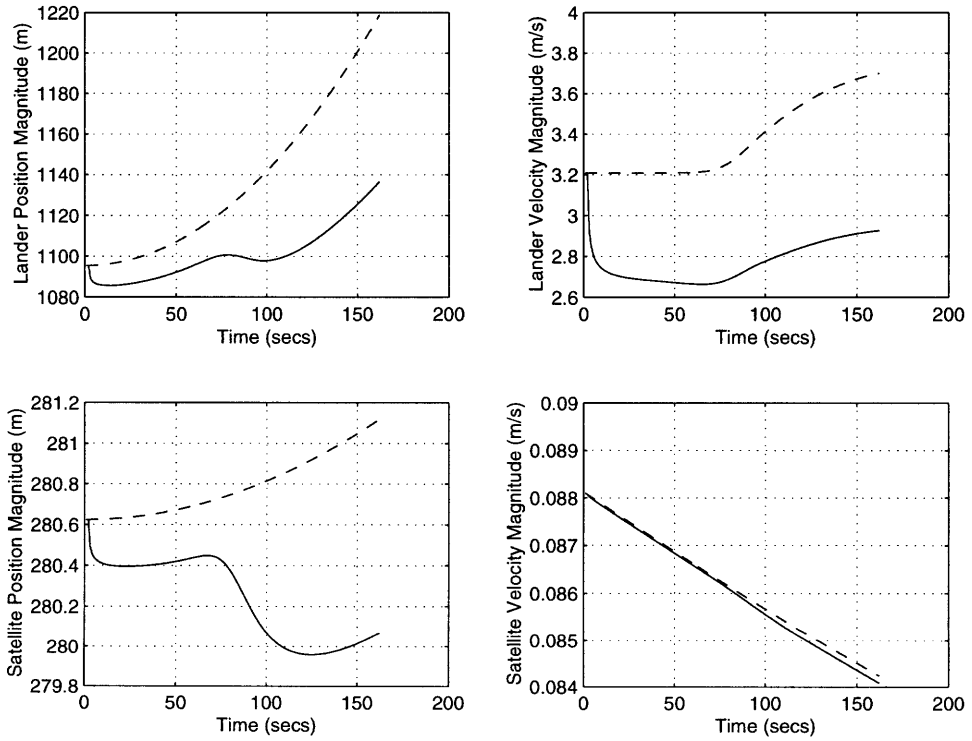

Figure 4.35: Sat3 Doppler Meas: Lander and Satellite Std. Deviation Magnitudes

The final satellite Doppler measurement profile incorporates Doppler measurements with all three satellites. Estimation errors with 3σ bounds of the lander, Satellite 1, Satellite 2, and Satellite 3 states are shown in Figures 4.36 to 4.39, respectively. Additionally, position and velocity standard deviation magnitudes can be found in Figure 4.40 and estimation errors for the Doppler biases (in units of metres per second) of each spacecraft are on Figure 4.41.

Figure 4.36 demonstrates that the lander velocity estimation errors in all axes are driven close to zero promptly. This is reflected in the responses of the corresponding standard deviations, which significantly decrease in all directions. In contrast, the position standard deviations display minimal reductions over time, although these reductions are greater for this case than for the singular satellite Doppler measurement cases. Position estimation errors are not improved, as the initial biases are not corrected. Thus, like the previous satellite Doppler cases, multiple Doppler measurements cannot be expected to improve knowledge of the lander position states to any substantial degree.

The other figures representing this measurement profile are also consistent with the previous satellite Doppler cases. Figures 4.37 to 4.39 indicate that the filter is not able to soundly improve upon the satellite estimation errors and standard deviations. This is also well illustrated in Figure 4.40, where all standard deviation magnitudes for this case are compared to those of the no measurement case. Finally, Figure 4.41 confirms that using three Doppler measurements will not impair the Doppler bias estimation errors since these estimation errors are still well bounded, as is the situation with one Doppler measurement (Figure 4.29).

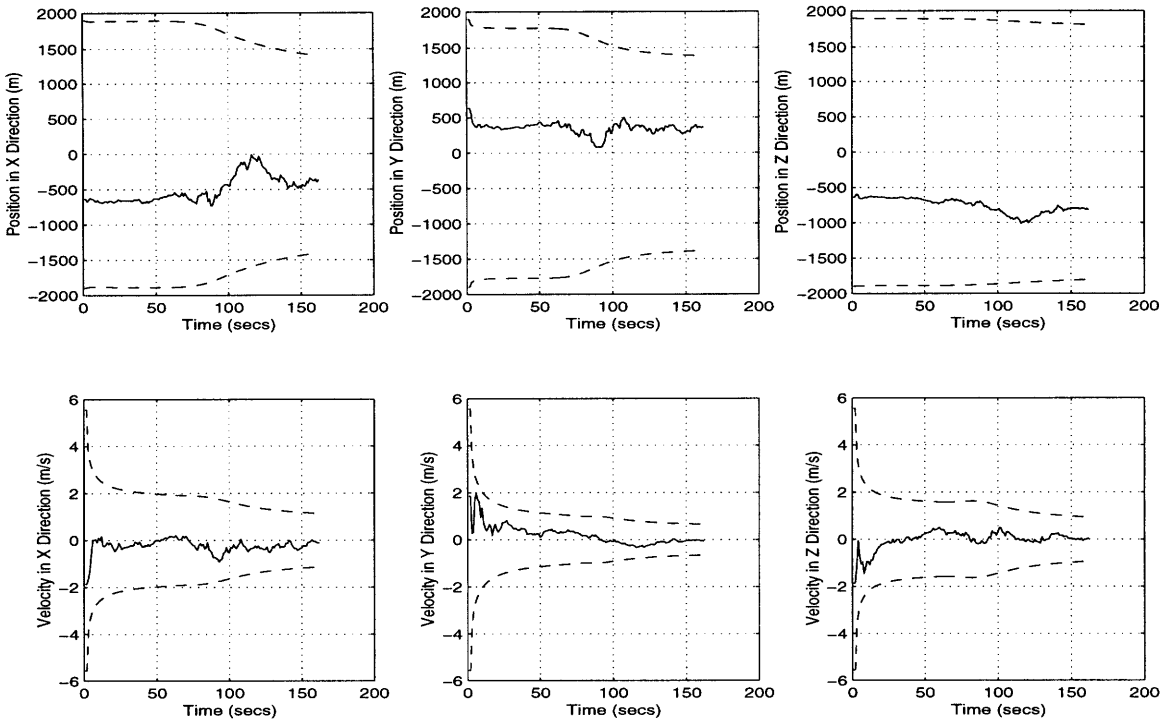

Figure 4.36: All Sat Dopp Meas: Lander Estimation Errors with 3σ Boundaries

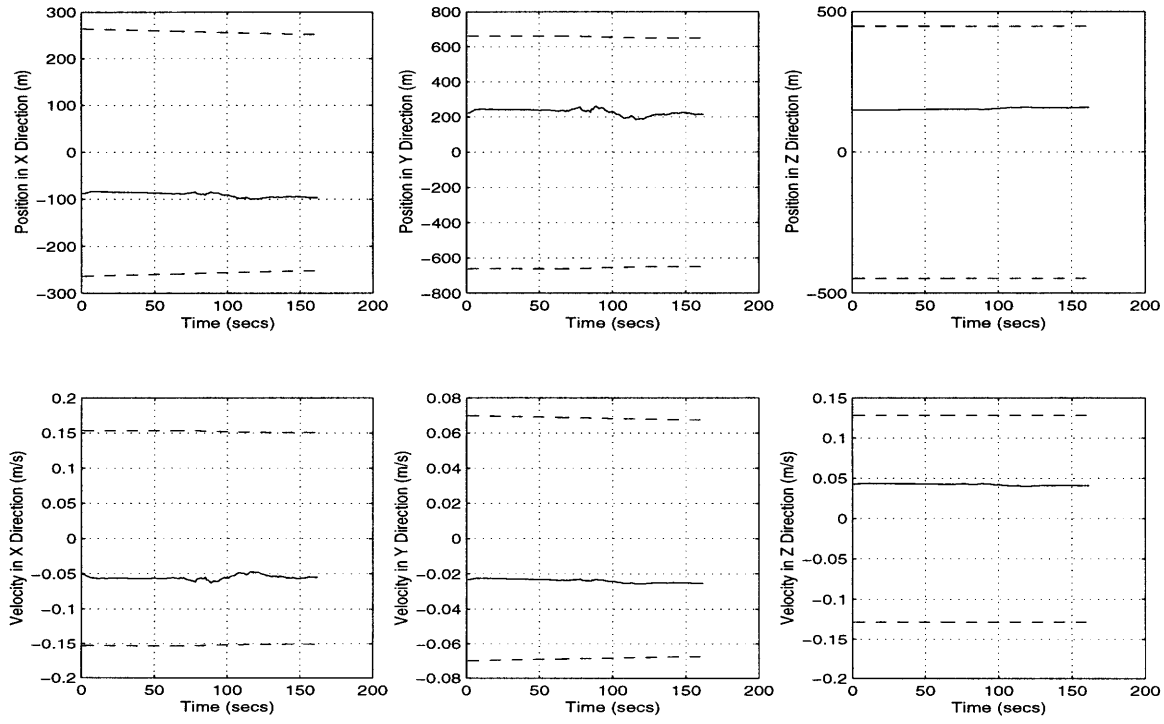

Figure 4.37: All Sat Dopp Meas: Satellite 1 Estimation Errors with 3σ Boundaries

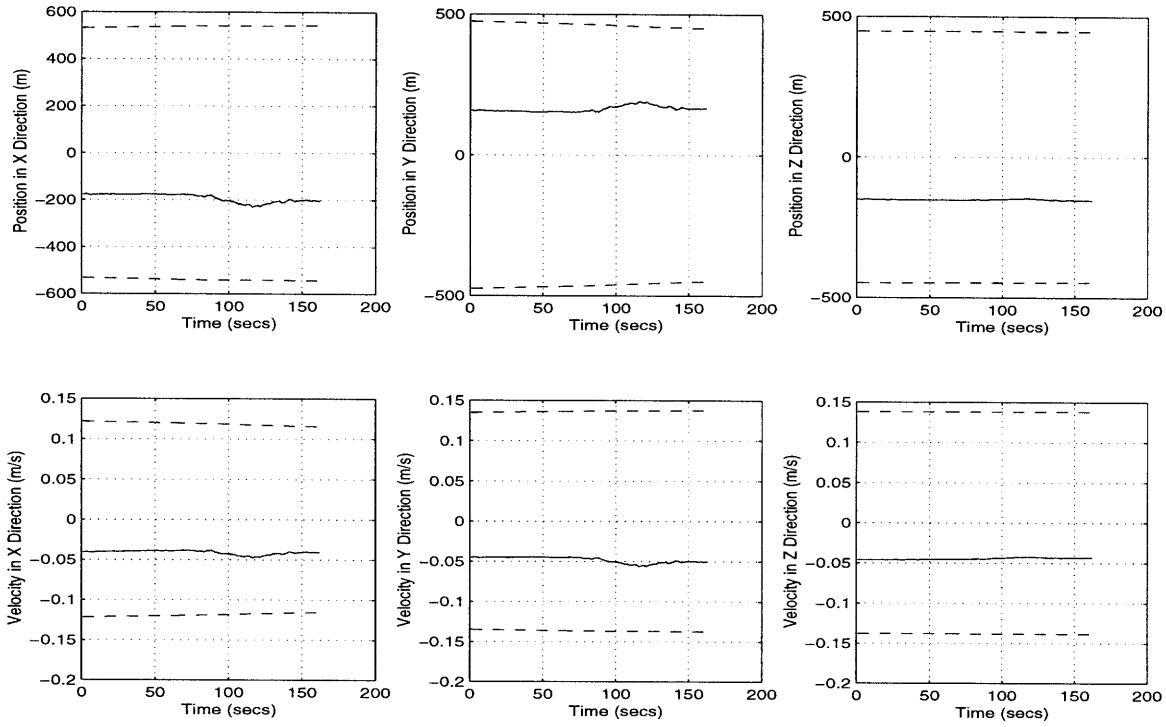

Figure 4.38: All Sat Dopp Meas: Satellite 2 Estimation Errors with 3σ Boundaries

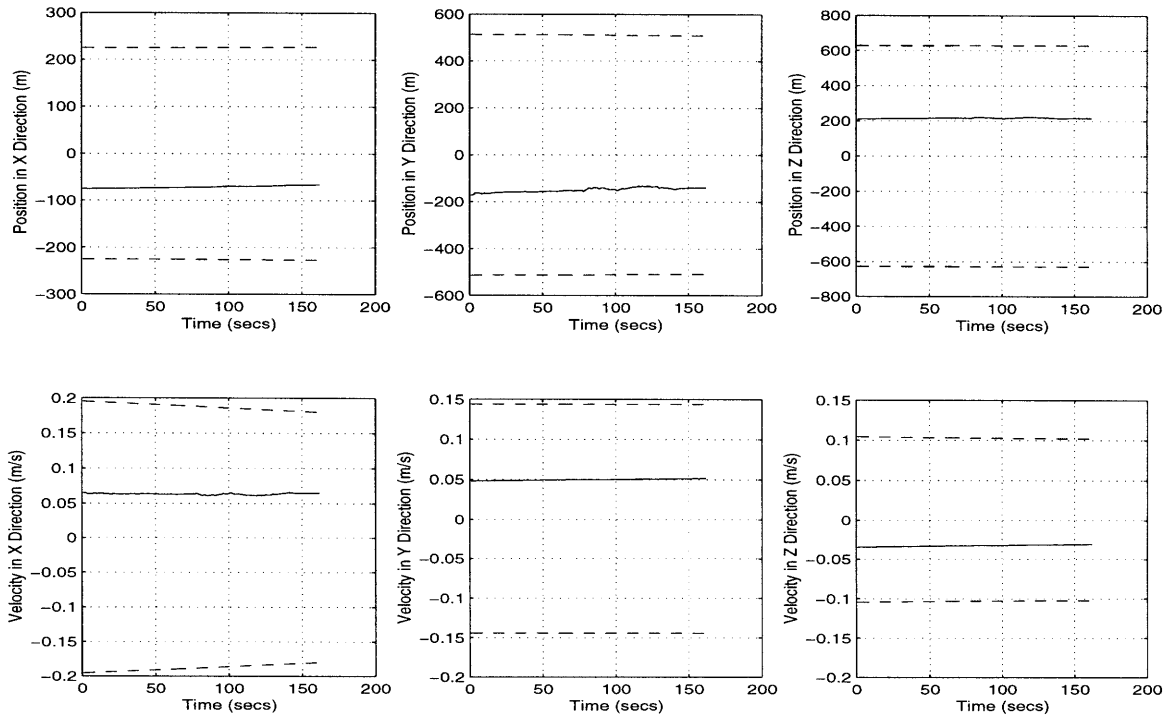

Figure 4.39: All Sat Dopp Meas: Satellite 3 Estimation Errors with 3σ Boundaries

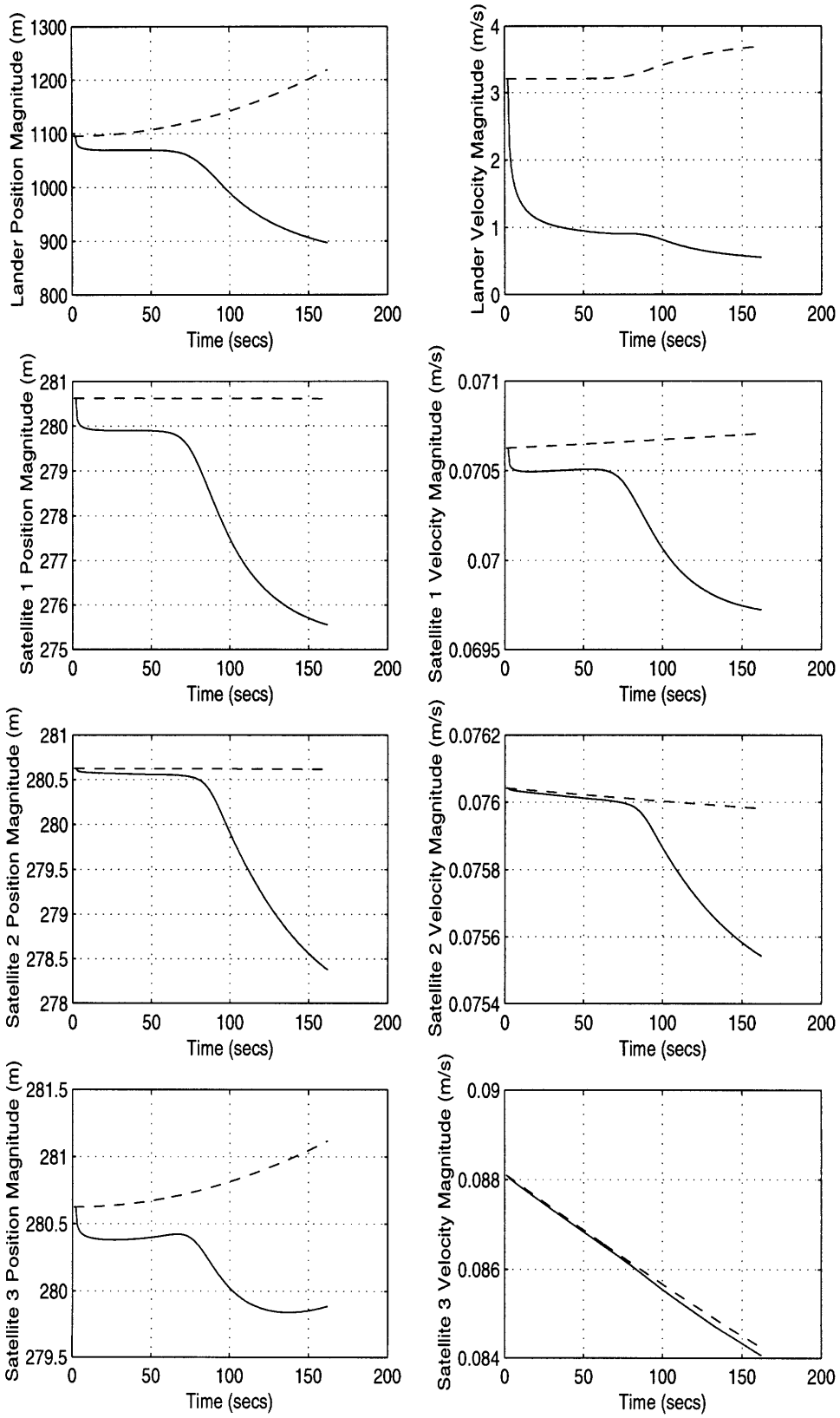

Figure 4.40: All Sat Dopp Meas: Standard Deviation Magnitudes

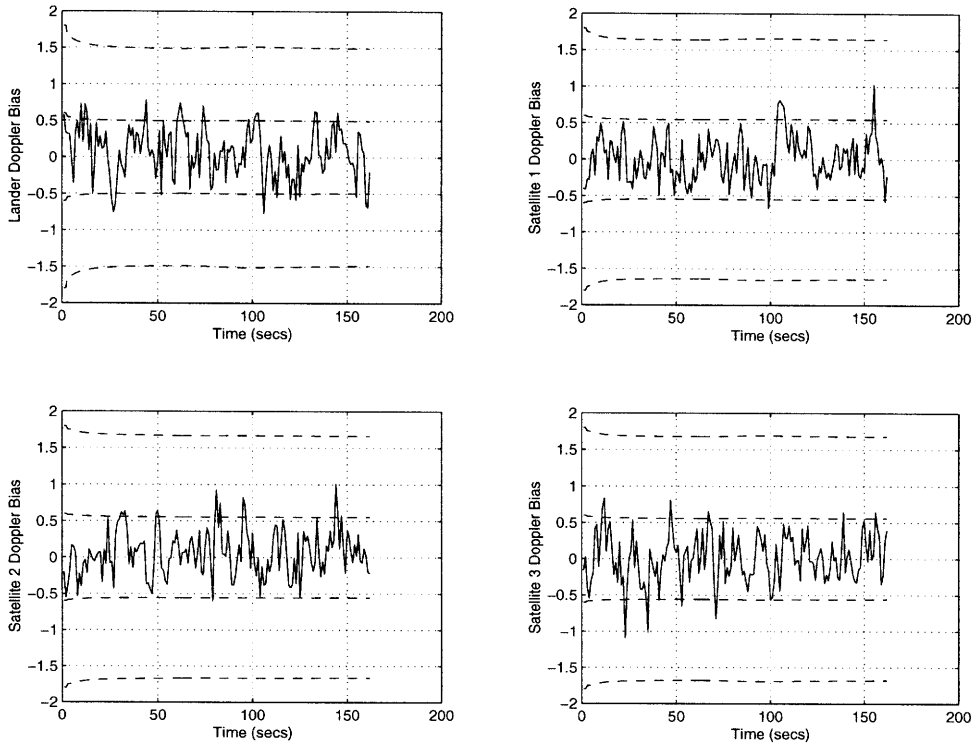

Figure 4.41: All Sat Dopp Meas: Doppler Bias Estimation Errors with 1σ/3σ Bounds

Table 4.2 compares the final lander state standard deviations of the no measurement case and the four Doppler measurement cases. In summary, Doppler measurements have the greatest effect on the lander velocity states. (In contrast, Table 4.1 shows that range measurements hold considerable influence on both lander position and velocity states.) The most favourable results are those of the measurement profile using all three satellites, although the single satellite case results do exhibit the minimizations of velocity standard deviations in one axis. Similarly to Table 4.1, the minimum velocity value out of the single satellite cases is the Z-axis velocity in the Satellite 3 case, because the range vector between the lander and Satellite 3 lies more directly on the Z-axis than any of the other range vectors on any other axis.

Lander State Std. Dev.	Measurement Profile (Doppler Measurements)				
	No Meas	Satellite 1	Satellite 2	Satellite 3	All Sats
X Position	721.3008 m	620.8925 m	695.5263 m	716.6128 m	475.1788 m
Y Position	692.3987 m	553.8649 m	641.2200 m	614.9201 m	462.0775 m
Z Position	697.0675 m	694.1867 m	679.3316 m	632.5754 m	604.3277 m
X Velocity	2.2852 m/s	0.8439 m/s	2.1144 m/s	2.2796 m/s	0.3832 m/s
Y Velocity	1.8635 m/s	1.6320 m/s	0.7032 m/s	1.7982 m/s	0.2281 m/s
Z Velocity	2.2351 m/s	2.2133 m/s	2.0842 m/s	0.3572 m/s	0.3266 m/s

Table 4.2: Final Lander Standard Deviations for Doppler Measurement Profiles

4.3.4 Beacon Range Measurement Case

EKF performance is also evaluated for two-way range measurements with surface beacons using three measurement profiles. The first measurement profile will have range measurements taken between the lander and Beacon 1, whose initial position is directly below the final position of the lander. The second measurement profile involves range measurements with Beacon 2, whose initial position is five degrees latitude north of Beacon 1. The third measurement profile takes range measurements with both surface beacons. The final lander standard deviations of the three cases are compared with those of the no measurement case in Table 4.3.

For reference, a close-up of the nominal trajectories on Figure 4.6 is exhibited in Figure 4.42, focusing on the lander and surface beacons. However, since Mars does not rotate a great deal in 162 seconds (the length of the simulation), the surface beacons appear to be stationary in this picture. Of course, this is misleading since the surface beacons are always moving as the planet rotates.

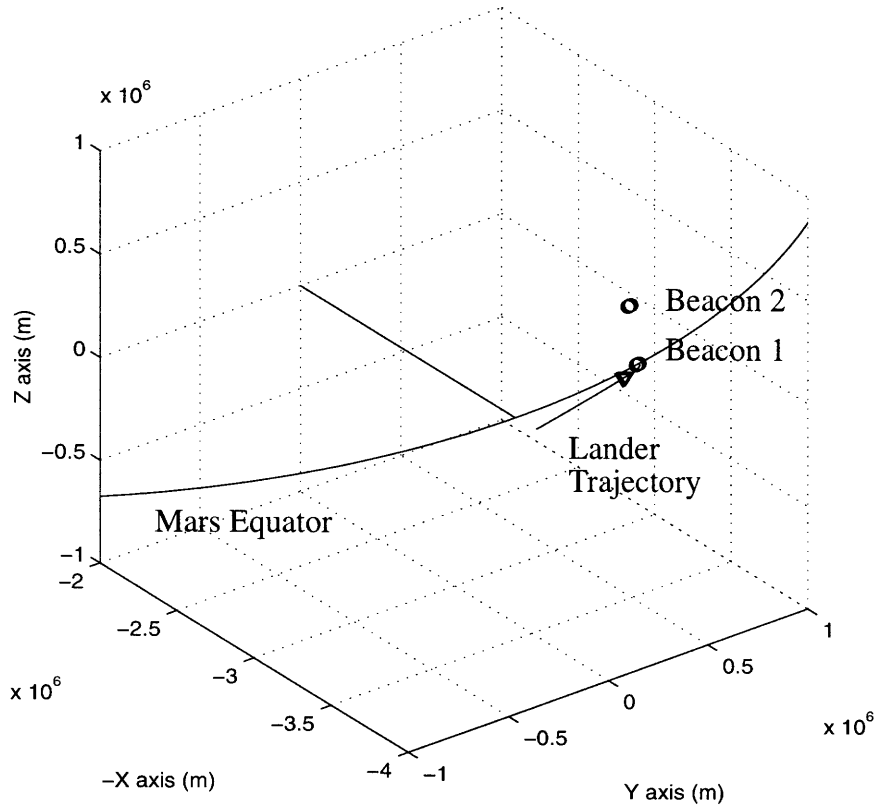

Figure 4.42: Nominal Trajectory of Lander with Surface Beacons

Estimation errors with 3σ bounds of the lander and Beacon 1 states are plotted in Figures 4.43 and 4.44, respectively. The standard deviations of the lander positions reveal that, initially, the filter has a powerful influence in the Y direction only. This influence continues and expands to the X direction after a while, growing stronger in time. The Z direction is affected only in about the last 20 seconds, and not as much as the other two axes at that. This activity also corresponds with the respective estimation error responses.

Like satellite range measurement filtering, surface beacon range measurement filtering is most effective in the axis of the largest range vector component. To illustrate this, the lander trajectory close-up view in Figure 4.42 is necessary for the sake of perception. At the beginning of the simulation, the range vector between the lander and Beacon 1 appears

to lie directly parallel with the Y axis. As the satellite travels in time, the X component of the range vector grows increasingly larger as well. Finally, as the lander nears its ultimate position, which is almost directly overhead Beacon 1, the range vector also gains a slight Z component. Thus, the range vector components in time are consistent with the position standard deviation reductions. Furthermore, since the range vector is always strongest in the X and Y axes (especially the Y axis), the lander velocity estimation errors and standard deviations in these directions also respond accordingly.

In comparison, the estimation errors and standard deviations of the beacon states show very little response to the EKF. This is because the initial standard deviations of these states are much smaller than those of the lander, which makes the beacon states much less sensitive to filtering. In addition, since the initial uncertainties (and likewise, the measurement sensitivities) of the beacon positions are smaller than those of the satellite positions, other relevant states in the filter are thus weighted more for beacon measurements than for satellite measurements. As a result in this case, the lander states are much more sensitive to the EKF with surface beacon range measurements than with satellite range measurements, allowing its standard deviations to be reduced even further. This is confirmed when comparing lander standard deviations from the satellite range measurement cases in Table 4.1 to those from the beacon range measurement cases in Table 4.3.

Other plots include the standard deviation magnitudes of the lander and beacon states in Figure 4.45 and the range measurement bias estimation errors with 1σ and 3σ bounds in Figure 4.46. The standard deviation magnitudes are consistent with the other figures: the lander position and velocity magnitudes are reduced significantly while the beacon position magnitude barely responds to the filter at all. In Figure 4.46, the bias estimation errors are well bounded, since they are predominantly kept within 1σ and never stray outside of 3σ.

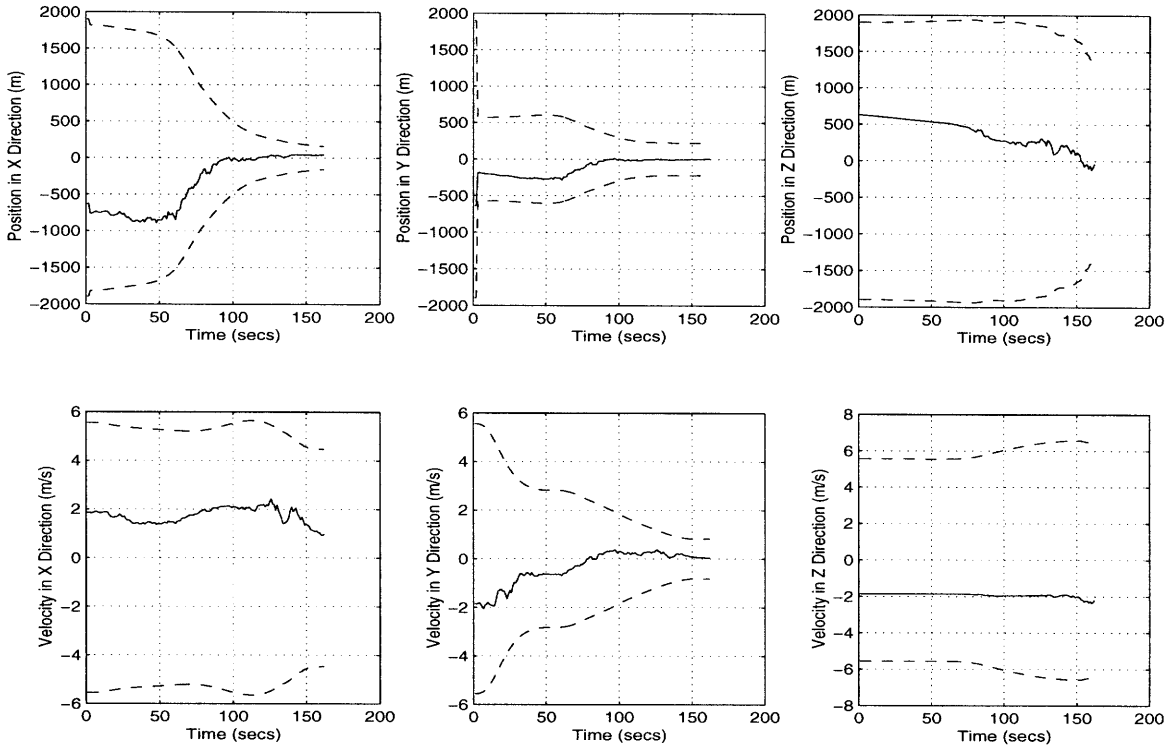

Figure 4.43: Beac1 Range Meas: Lander Estimation Errors with 3σ Boundaries

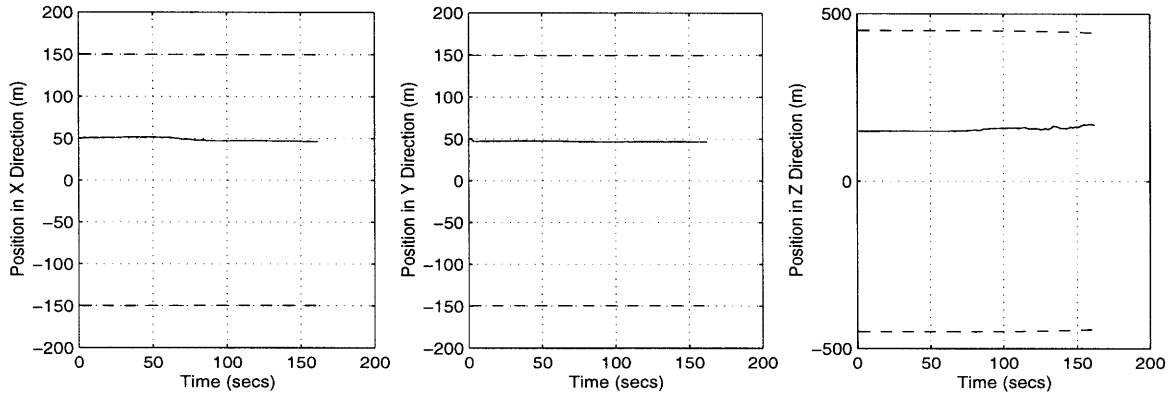

Figure 4.44: Beac1 Range Meas: Beacon 1 Estimation Errors with 3σ Boundaries

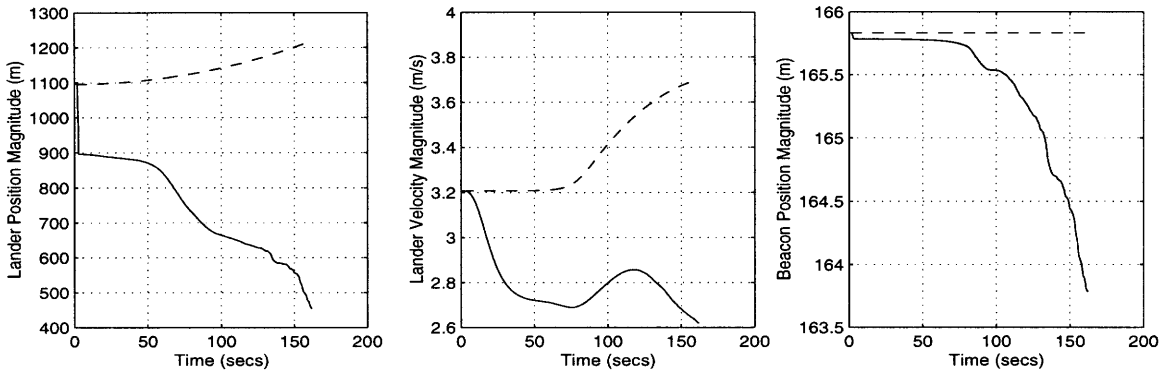

Figure 4.45: Beac1 Range Meas: Lander and Beacon Std. Deviation Magnitudes

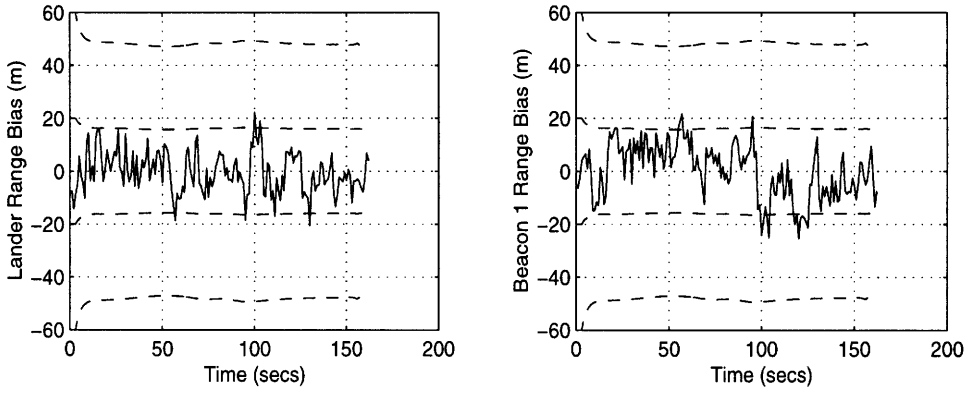

Figure 4.46: Beac1 Range Meas: Range Bias Estimation Errors with 1σ/3σ Bounds

The next figures include results from the simulation with Beacon 2 range measurements. The initial position of Beacon 2 was placed five degrees latitude north of Beacon 1. Figure 4.47 and Figure 4.48 display estimation errors with 3σ bounds of the lander and Beacon 2 states, while Figure 4.49 shows the standard deviation magnitudes of these states.

The estimation errors and standard deviations in Figure 4.47 demonstrate that the filter has the strongest effects on the lander states in the Y and Z axes. Initially, in the Y position, the filter is very strong but its influence seems to wane as time progresses. This is in contrast to the Z position, where the filter appears to be gaining influence in time. Furthermore, the standard deviation of the X position shows an minimal initial impact which seems to fade quickly. This corresponds with the motion of the range vector. Like the Beacon 1 case, this range vector has a very large initial Y component that decreases as the lander nears its final position. The Z component grows larger as the lander passes nearly directly south of the beacon. Finally, throughout the simulation, the smallest component of the range vector lies in the X direction.

Another point of interest is that the filter stops taking measurements from 148 seconds to the end of the simulation. This is because the lander is decreasing in altitude throughout the simulation. Since the largest component of the altitude is in the X direction, this explains why the X component of this range vector decreases as time progresses. Consequently, from the point of view of the beacon, the lander drops below the horizon at 148 seconds and is no longer within sight.

Like those from the satellite range simulation cases, the lander position estimation errors in Figure 4.47 also have noticeable biases. However, even though beacons use less states than satellites in this design (since beacon velocities are not state variables), the filter is still accountable for 6 lander states, 3 beacon states, 2 range bias states, and 9 IMU states: a total of 20 states for each beacon range measurement. Again, this is a lot to handle for a scalar measurement. Thus, lander estimation errors are susceptible to biases with range measurement filtering in general (i.e. using satellites or beacons).

The remaining plots complete the analysis for Beacon 2 range measurement filtering. Figure 4.48 shows that the filter has very little effect on the beacon state estimation errors, whose biases remain uncorrected throughout the simulation, and standard deviations. Figure 4.49 shows fairly consistent reductions in the standard deviation magnitudes. The fact that the simulation discontinues taking measurements at 148 seconds is well illustrated in the lander position and velocity plots, as the standard deviation magnitudes start to rise at this time step. This figure also illustrates the minimal response in the standard deviation magnitude of the beacon position, relative to the lander position.

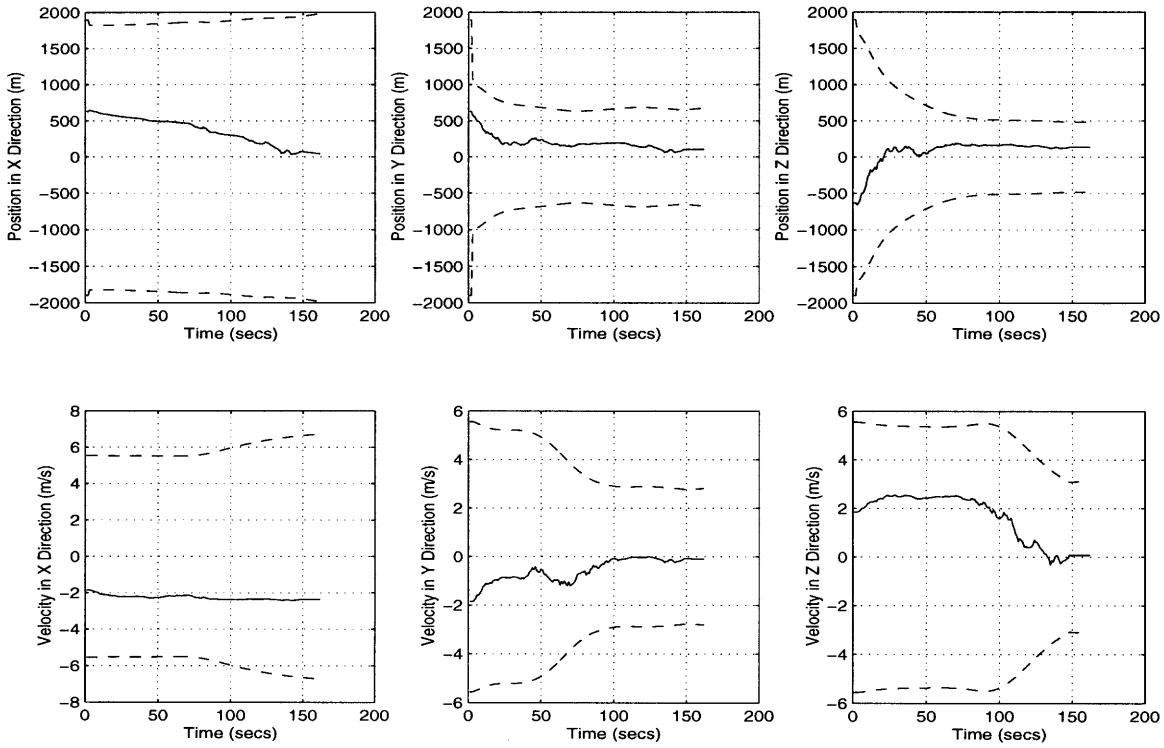

Figure 4.47: Beac2 Range Meas: Lander Estimation Errors with 3σ Boundaries

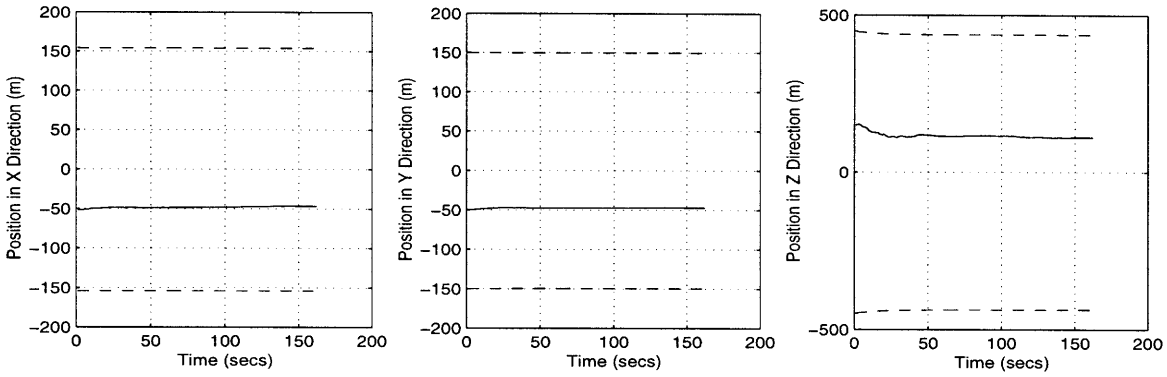

Figure 4.48: Beac2 Range Meas: Beacon 2 Estimation Errors with 3σ Boundaries

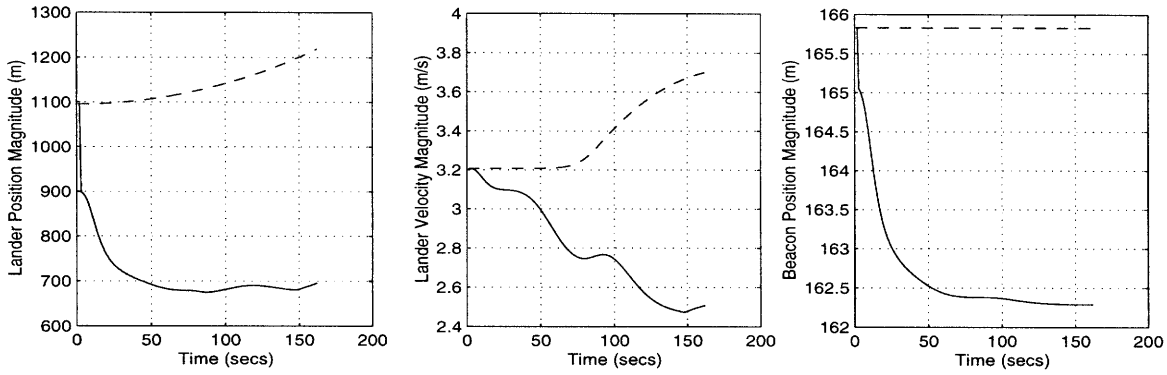

Figure 4.49: Beac2 Range Meas: Lander and Beacon Std. Deviation Magnitudes

The final beacon range simulation incorporates measurements with both Beacon 1 and Beacon 2. Five figures in the following pages are used to analyze the EKF performance. Figure 4.50 displays the estimation errors and 3σ bounds of the lander states. Figures 4.51 and 4.52 show the same for Beacon 1 and Beacon 2, respectively. The standard deviation magnitudes of these position and velocity states are graphed in Figure 4.53, while the estimation errors for all range biases are found in Figure 4.54.

The lander state standard deviations and estimation errors in Figure 4.50 document excellent responses to the EKF. Position standard deviations are minimized a great deal, with the Y and Z direction components absorbing large initial reductions. Position estimation errors do contain slight biases, but these biases are well within 3σ. The filter also

holds substantial influence over the velocity standard deviations and estimation errors, especially in the Y and Z directions. Between both beacons, the range vectors have significant components in all three axes, allowing the EKF to improve all position and velocity estimates.

As a whole, the position states of the two beacons in Figures 4.51 and 4.52 show very little response to the filter, in comparison to the lander states in Figure 4.50. The initial biases in the estimation errors remain unaffected and, for both beacons, only the standard deviations in the Y direction show slight and gradual decreases. The decreases are in this direction because the range vectors have a strong component in this axis for both Beacon 1 and Beacon 2.

All standard deviation magnitudes graphed in Figure 4.53 always decrease in time, with no increases relating to the accelerometer bias. In contrast, range measurement filtering with all three satellites was not able to counter the accelerometer bias effects completely. However, as discussed earlier in this section, range measurement filtering is more effective with beacons rather than satellites because the beacon states have smaller initial standard deviations. Finally, these plots also show that the filter is most effective in reducing the lander position magnitude.

Bias estimation errors, illustrated in Figure 4.54 with 1σ and 3σ bounds, are very well bounded, and never stray outside of the 3σ bounds. However, after the 148 second mark when range measurements with Beacon 2 are discontinued, the lander and Beacon 2 range bias standard deviations quickly increase. This is because the range bias states are the most sensitive states to this measurement filtering in the latter time steps, as is shown in corresponding Kalman gain matrices. Thus, if the filter is not processing measurements regularly, this sensitivity (and the contributions to the range bias standard deviations from the filter) is lost.

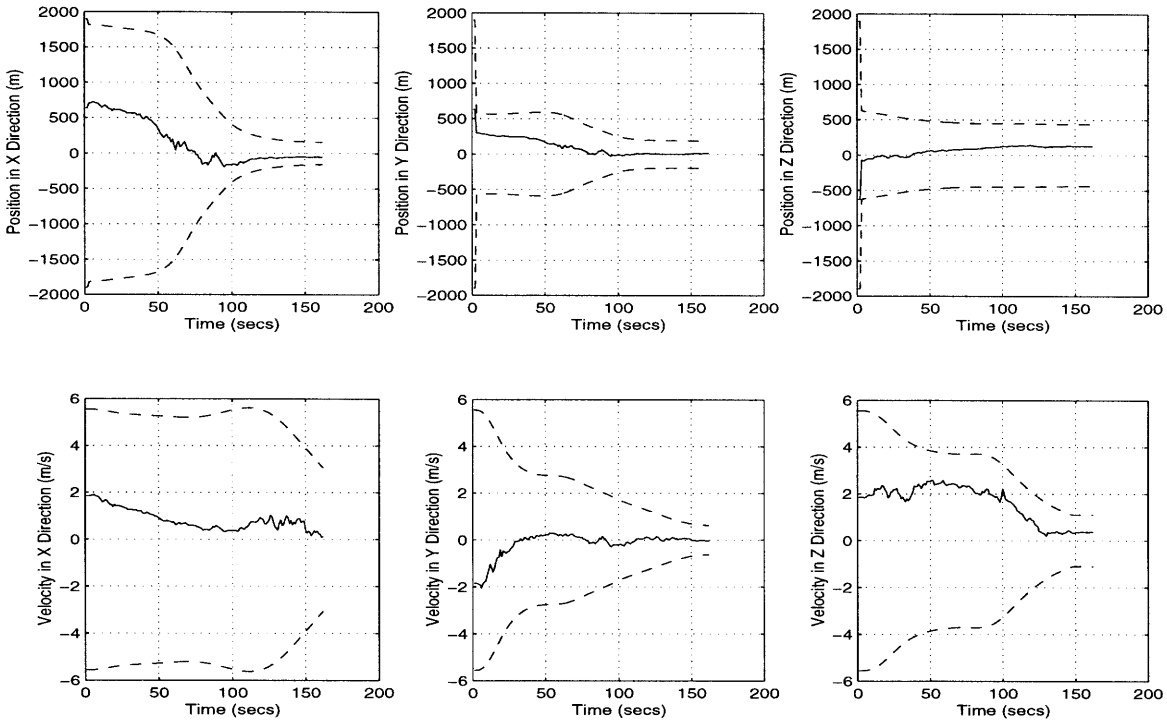

Figure 4.50: All Beac Range Meas: Lander Estimation Errors with 3σ Boundaries

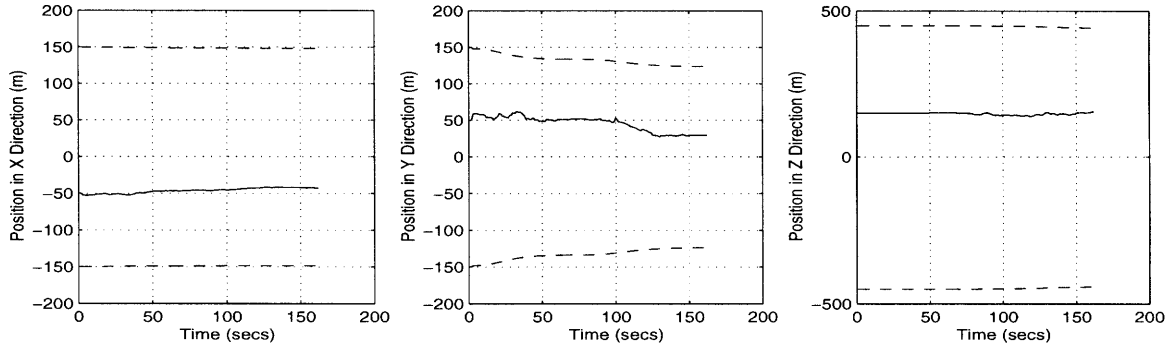

Figure 4.51: All Beac Range Meas: Beacon 1 Estimation Errors with 3σ Boundaries

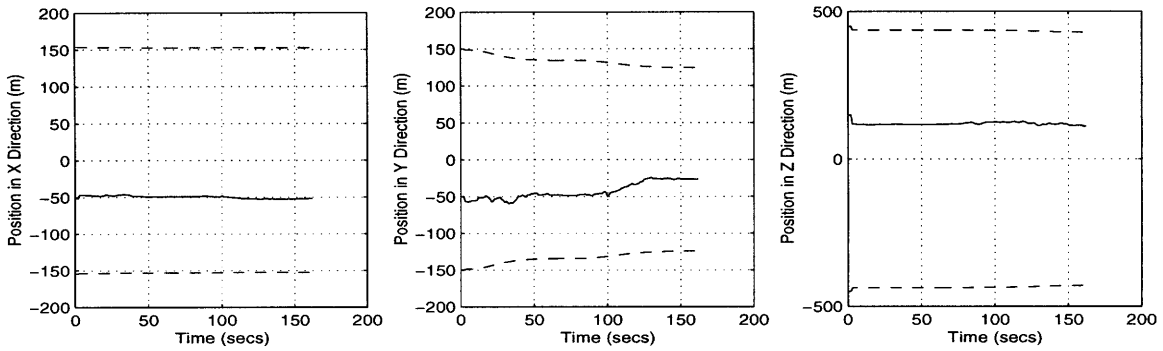

Figure 4.52: All Beac Range Meas: Beacon 2 Estimation Errors with 3σ Boundaries

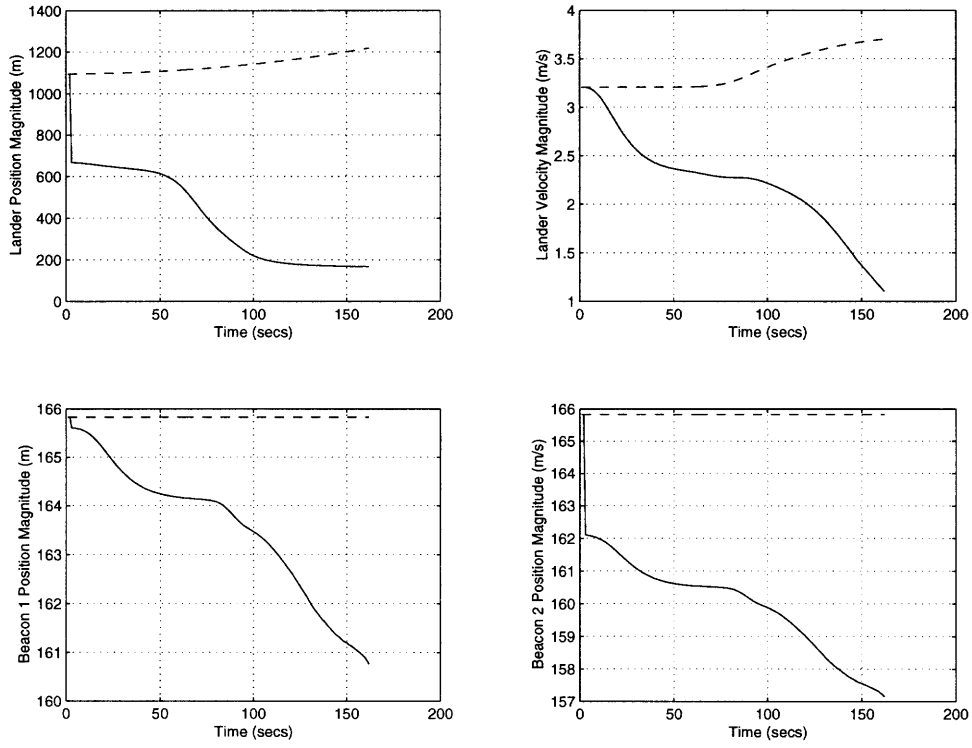

Figure 4.53: All Beac Range Meas: Standard Deviation Magnitudes

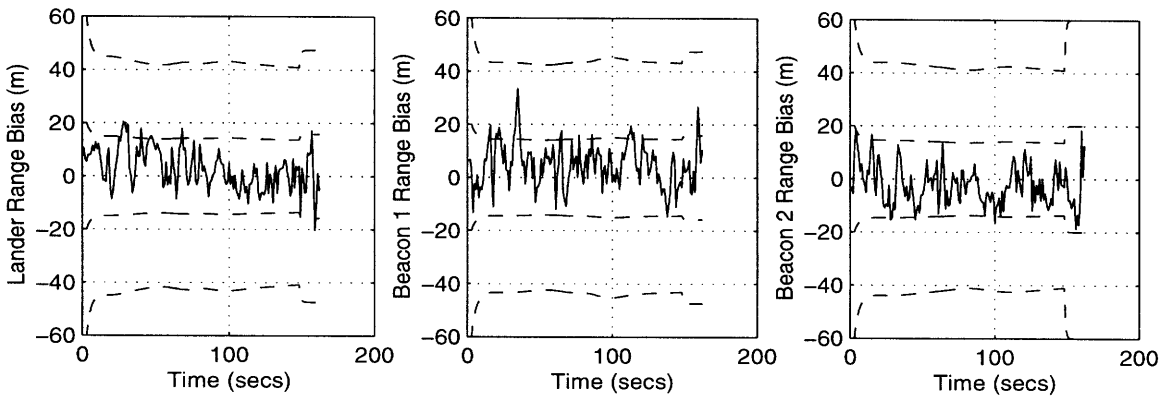

Figure 4.54: All Beac Range Meas: Range Bias Estimation Errors with 1σ/3σ Bounds

The final lander state standard deviations of the no measurement case and the three beacon range measurement cases are compared in Table 4.3. As should be expected, the measurement profile using both beacons yields the most favourable results. Furthermore, Beacon 1 range results illustrate that the filter is most effective in the X and Y directions while Beacon 2 range results are most effective in the Y and Z directions. Of course, this is due to the strength of the components of each range vector. The minimum position value in the two single beacon cases is the X-axis position in the Beacon 1 case. This stems from the fact the range vector between the lander and Beacon 1 lies more directly on the X-axis than the other range vector on any other axis. As a final note, this table also suggests that filtering with beacon range measurements is more effective than with satellite range measurements, when compared to Table 4.3.

Lander State Std. Dev.	Measurement Profile (Range Measurements)			
	No Meas	Beacon 1	Beacon 2	All Beacs
X Position	721.3008 m	52.8627 m	647.8235 m	52.4260 m
Y Position	692.3987 m	73.5868 m	197.8550 m	62.7443 m
Z Position	697.0675 m	445.0606 m	157.0557 m	146.1232 m
X Velocity	2.2852 m/s	1.4877 m/s	2.2275 m/s	1.0198 m/s
Y Velocity	1.8635 m/s	0.2740 m/s	0.7727 m/s	0.2081 m/s
Z Velocity	2.2351 m/s	2.1377 m/s	0.8548 m/s	0.3694 m/s

Table 4.3: Final Lander Standard Deviations for Range Measurement Profiles

4.3.5 Beacon Doppler Measurement Case

Doppler measurements with surface beacons can also be processed in the EKF. Analysis for such measurement types is presented in this section. Three measurement profiles are used: Doppler measurements with Beacon 1, Beacon 2, and both beacons. The results of these measurement profiles are discussed and compared against the no measurement case in Table 4.4 on page 110.

Performance results of the simulation involving Beacon 1 Doppler measurement filtering are portrayed in Figures 4.55 to 4.58. The first two of these plots display the estimation errors with 3σ bounds of the lander and Beacon 1 states. Figure 4.57 shows the magnitudes of the standard deviations of these states. Finally, estimation errors of the Doppler bias states can be found in Figure 4.58.

The estimation errors and standard deviations of the lander and Beacon 1 states in Figure 4.55 and 4.56 show similarities with the satellite Doppler results in Section 4.3.3. Once again the filter has negligible effects on the beacon estimation errors and standard deviations. Also, the filter is most effective on lander velocity states in the axis of the larg-

est range vector component, which is the Y axis for most of this simulation. Furthermore, as position errors are dependent on range vector components in surface beacon (and satellite) range measurement filtering, the Beacon 1 range measurement case results should show that the lander position is most affected in the Y direction as well. The corresponding plots in Figure 4.43 verify this to be true. Furthermore, the lander position estimation errors and standard deviations are most affected in the X and Y directions. If position states are mostly dependent on delta-range in the Doppler measurement sensitivity model (Equation 2.71), then it would make sense that the motion of the range vector is predominantly in the X and Y directions. Referring to the close-up plot of the nominal trajectories in Figure 4.42, this is indeed the case. The lander decreases in altitude (which is chiefly X axis motion) as it travels towards Beacon 1 in the Y direction.

However, an additional characteristic of these results is that, unlike the satellite Doppler results, beacon Doppler measurement filtering seems to be more effective on the lander position states than on the lander velocity states. This is because the Kalman gain matrix, which is representative of the state sensitivity to the measurement, is dependent on the state covariance matrix and therefore, indirectly, on the state standard deviations as well. Since the beacon states have much lower initial standard deviations than the satellite states, the other relevant states will be much more sensitive to beacon Doppler filtering than to satellite Doppler filtering.

The lander and beacon standard deviation magnitudes in Figure 4.57 support some of the previous results as well. Out of the three standard deviation magnitudes, the lander position magnitude displays the most dramatic decreases. In comparison, the beacon position magnitude exhibits the slightest responses. Again, the lander velocity magnitude is susceptible to the accelerometer bias-based increases.

Doppler bias estimation errors of the lander and Beacon 1 are displayed in Figure 4.58. As usual, 1σ and 3σ bounds are included. The results are consistent with the Doppler bias results of the satellite Doppler measurement cases in Section 4.3.3: the bias estimation errors are again well bounded, as they are predominantly kept within 1σ and never stray outside of 3σ.

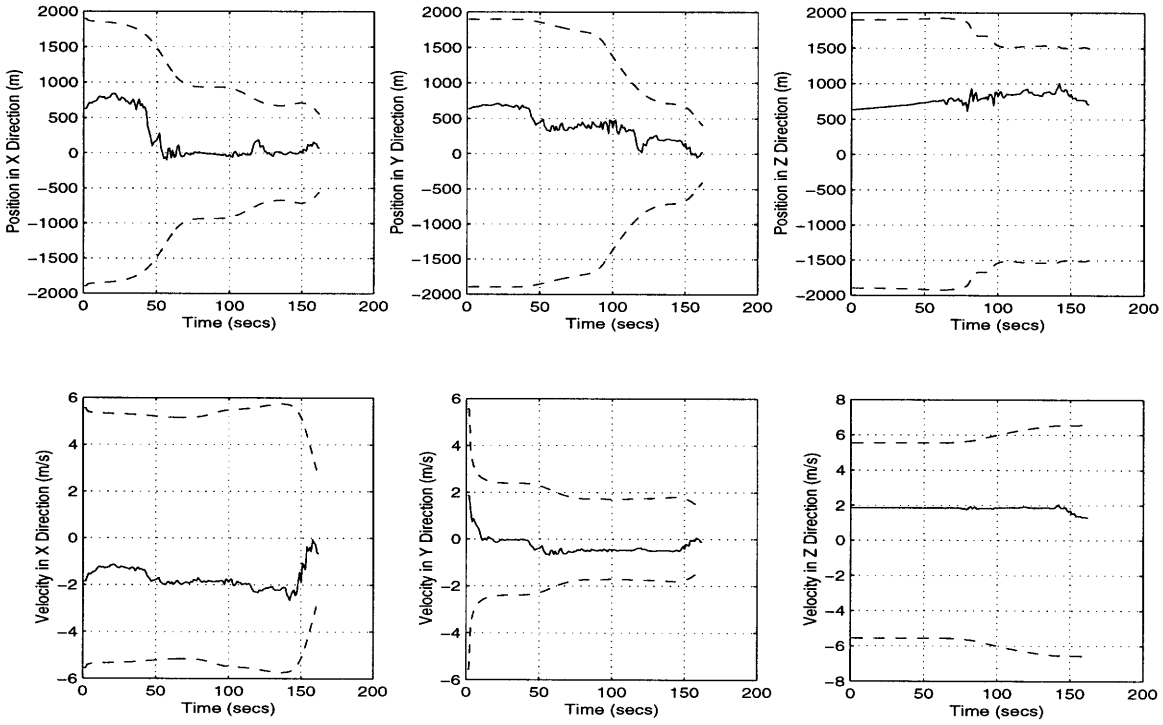

Figure 4.55: Beac1 Doppler Meas: Lander Estimation Errors with 3σ Boundaries

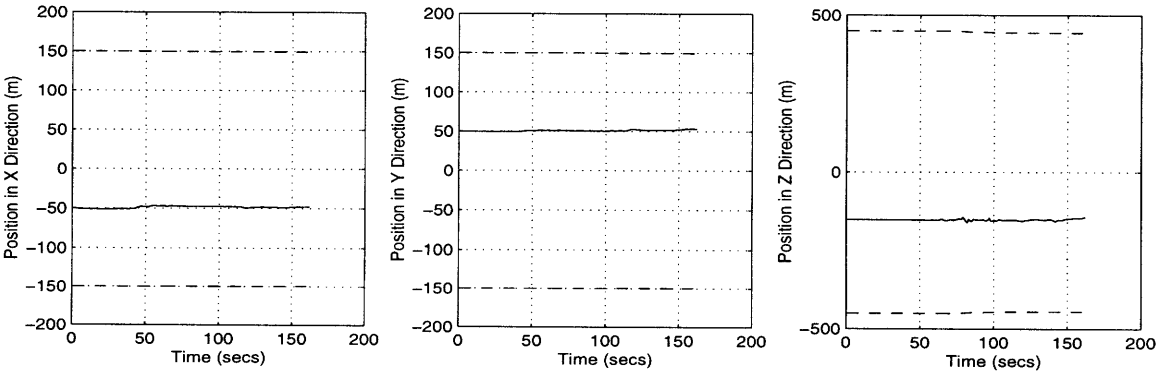

Figure 4.56: Beac1 Doppler Meas: Beacon 1 Estimation Errors with 3σ Boundaries

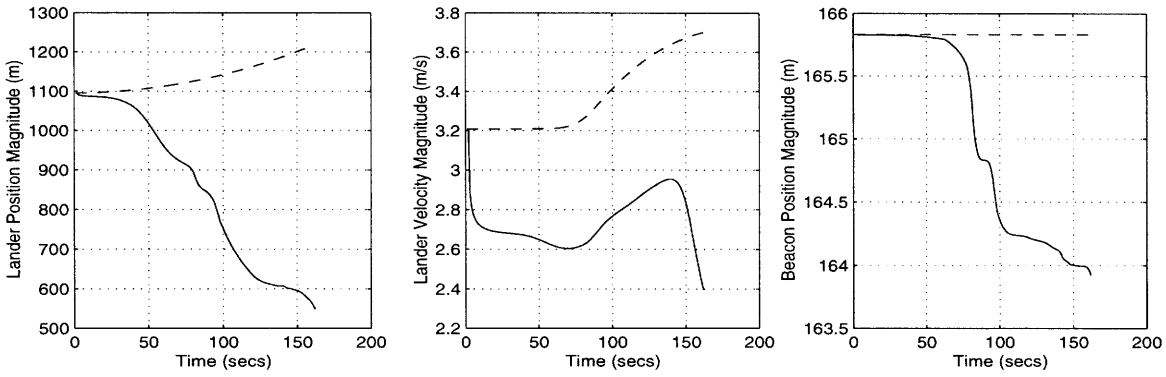

Figure 4.57: Beac1 Doppler Meas: Lander and Beacon Std. Deviation Magnitudes

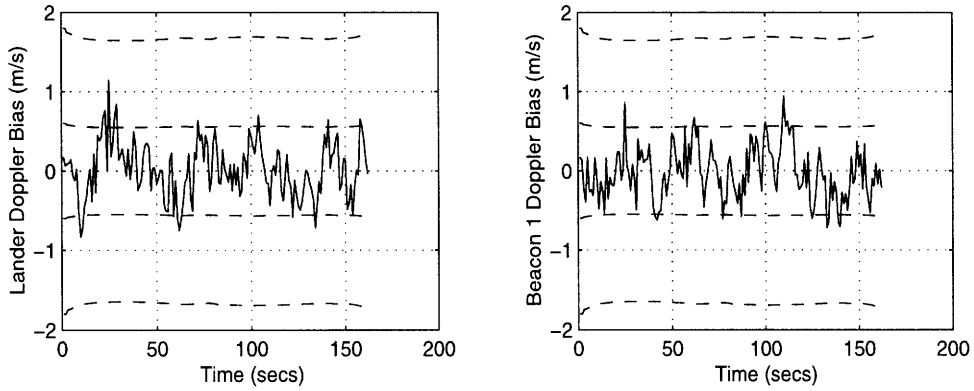

Figure 4.58: Beac1 Doppler Meas: Range Bias Estimation Errors with 1σ/3σ Bounds

Results of the simulation using Doppler measurements with Beacon 2, presented in Figures 4.59 to 4.61, are consistent with the previous results of the Beacon 1 Doppler measurement case. Figure 4.59, which contains the estimation errors and standard deviations of the lander states for this case, shows similar patterns to results in the Beacon 1 Doppler measurement case. Figure 4.60 displays beacon state estimation errors and standard deviations, and confirms that the filter has little effect on these errors, as with all cases thus far.

Finally, the results exhibited in these two figures are reflected in the magnitudes of the position and velocity standard deviations of the lander and Beacon 2, which are displayed in Figure 4.61. It is useful to recall that the lander and Beacon 2 are not within sight of each other after the 148 second mark, so the simulation cannot take Doppler measurements with Beacon 2 after that time step.

Taking a closer look at the components of the lander estimation errors and standard deviations in Figure 4.59, it is found that the filter is most effective on the lander position and velocity states in the Y and Z directions. Also, the Y axis velocity state shows an immediate reaction to the filter while the Z axis shows its standard deviation reduction later in time. It is seen that velocity states are dependent on the range vector components in Doppler measurement filtering, as the position states are in range measurement filtering. Thus, the lander position estimation errors and standard deviations in Beacon 2 range filtering should also show the same response: the immediate Y axis effect followed in time by the Z axis influence. Indeed, the appropriate plot, Figure 4.47, shows this to be true. In addition, this Z axis influence helps to curb the usual accelerometer bias-based increases in the lander velocity standard deviation magnitude. Without measurement filtering, it is the velocity standard deviations in the X and Z directions that are quite vulnerable to the effects of the accelerometer bias. Finally, the lander position state responses for this case suggest that the motion of the range vector is predominantly in the Y and Z axes. This too can be confirmed with examination of the nominal trajectories close-up plot in Figure 4.42.

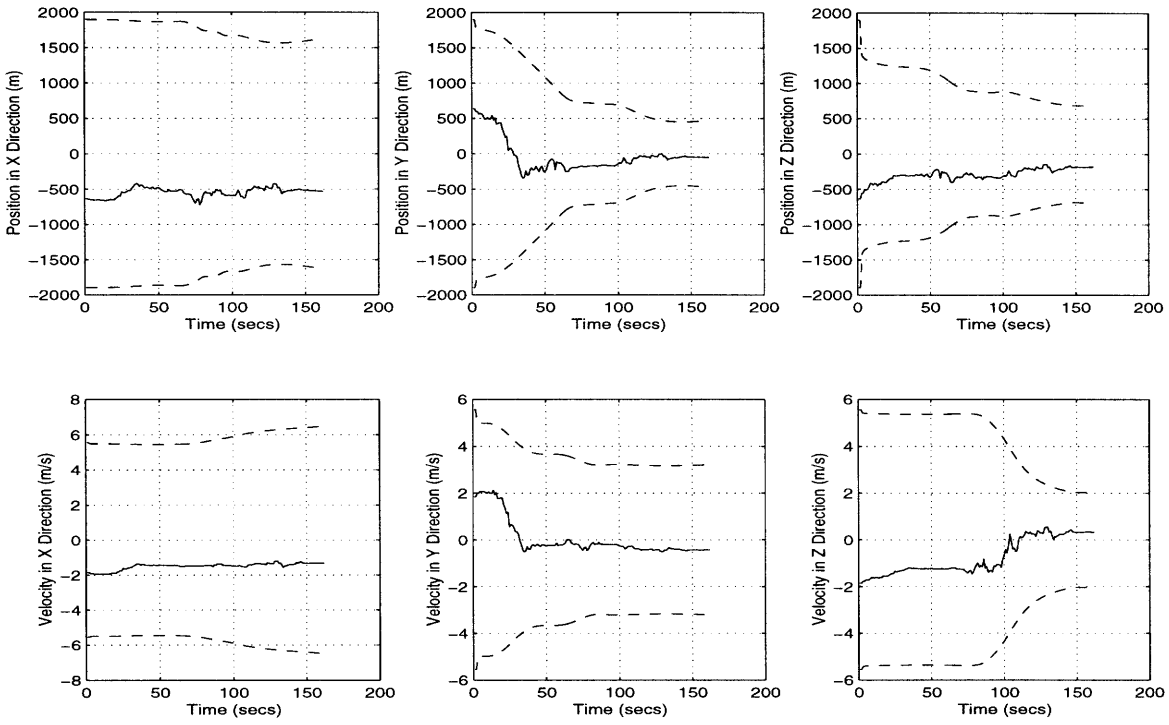

Figure 4.59: Beac2 Doppler Meas: Lander Estimation Errors with 3σ Boundaries

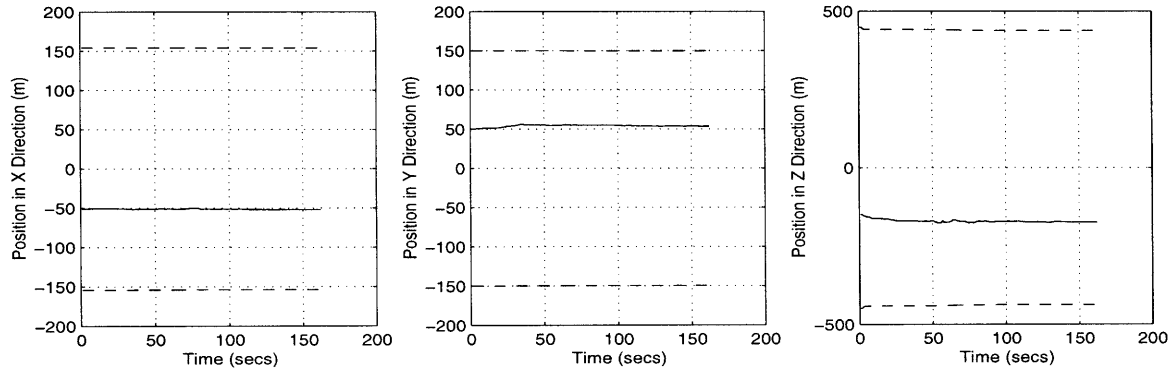

Figure 4.60: Beac2 Doppler Meas: Beacon 1 Estimation Errors with 3σ Boundaries

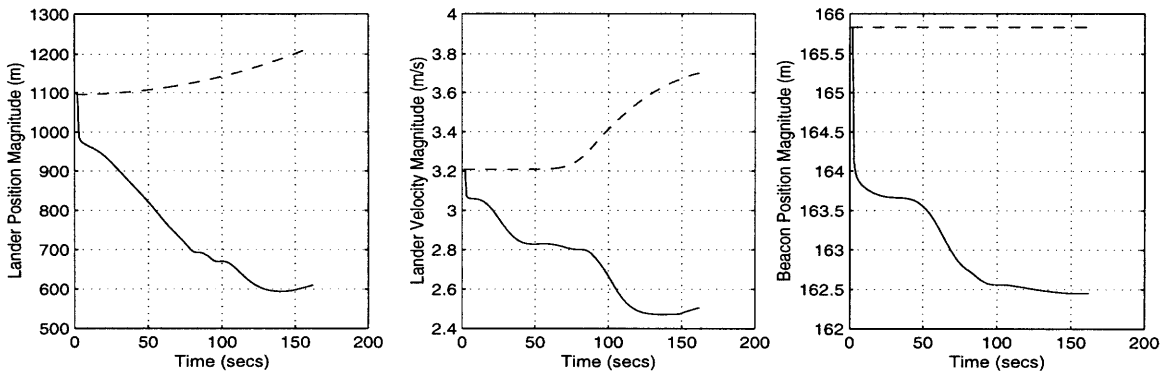

Figure 4.61: Beac2 Doppler Meas: Lander and Beacon Std. Deviation Magnitudes

The last of the three beacon Doppler simulations handles measurements with both beacons. Filter performance results are analyzed with the aid of five plots. Figures 4.62, 4.63, and 4.64 display the estimation errors with 3σ bounds of the lander, Beacon 1, and Beacon 2 states, respectively. Standard deviation magnitudes of the afore mentioned states are presented in Figure 4.65. Estimation errors of the Doppler measurement bias states for the lander, Beacon 1 and Beacon 2 are shown in Figure 4.66.

According to Figure 4.62, the lander state estimation errors and standard deviations respond exceptionally well in all directions to the filter. Together, the two measurements represent all axes in the range and delta-range vector for all time steps. Lander position and velocity estimation errors are driven near zero and contain no significant biases. In addition, the corresponding standard deviations of these states are substantially reduced.

In a manner consistent with the previous results, the beacon state estimates do not exhibit much reaction to the filter. Figures 4.63 and 4.64 illustrate this fact. The filter can neither correct the initial biases in the estimation errors nor reduce the standard deviations to any substantial degree.

The standard deviation magnitudes in Fig 4.65 reflect the sizeable lander state responses and paltry beacon state responses. In addition, the magnitudes are always decreasing in time. This is especially noteworthy in the lander velocity standard deviation magnitude, which is most vulnerable to the accelerometer bias. However, the two beacon measurements successfully suppress accelerometer bias effects in all three axes, allowing the lander velocity magnitude to decrease in time with the other magnitudes. This figure also shows that the filter has more of an effect on the lander position magnitude than the lander velocity magnitude, relatively, which is consistent with past findings for beacon Doppler measurement filtering.

As with all Doppler measurement cases previously discussed (with satellites or beacons), bias estimation errors, shown in Figure 4.66, stay well within 1σ and 3σ bounds. Furthermore, the lack of Beacon 2 measurements processed past 148 seconds is apparent.

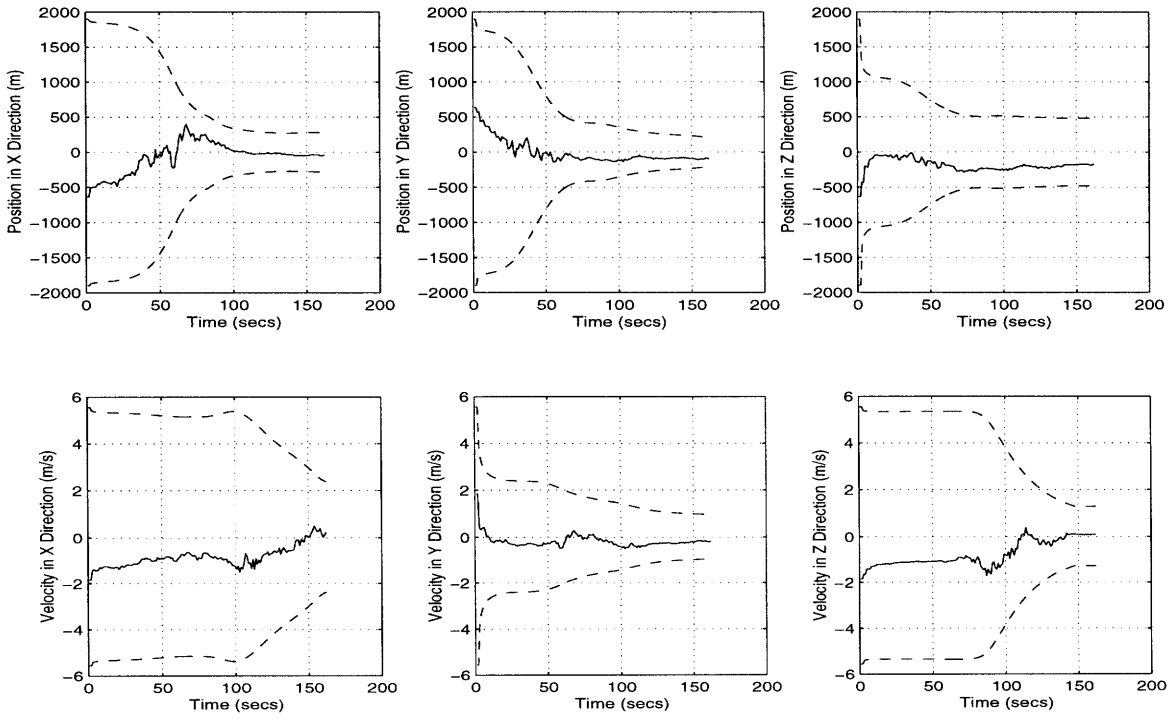

Figure 4.62: All Beac Dopp Meas: Lander Estimation Errors with 3σ Boundaries

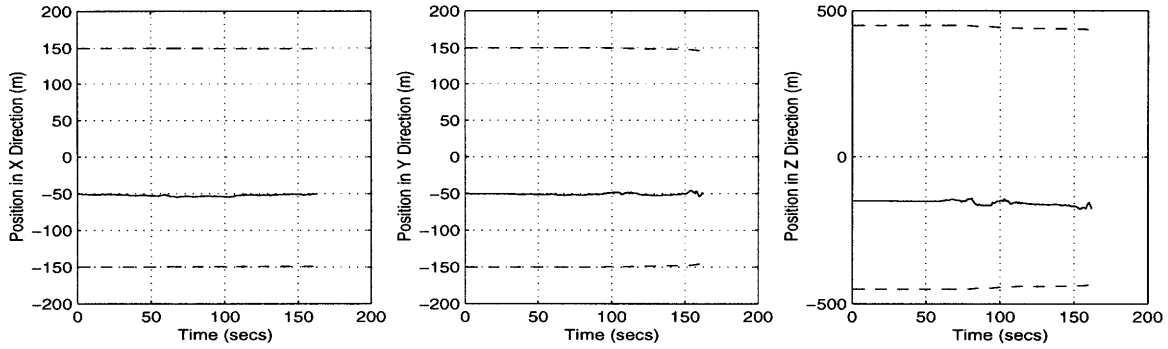

Figure 4.63: All Beac Dopp Meas: Beacon 1 Estimation Errors with 3σ Boundaries

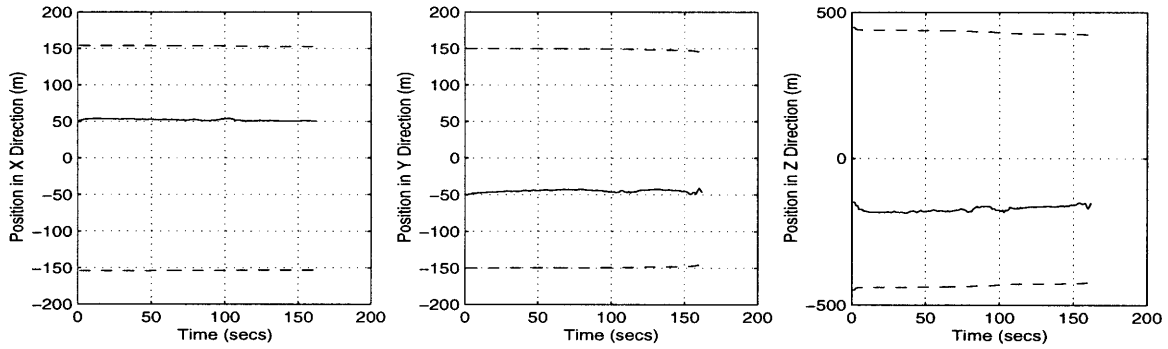

Figure 4.64: All Beac Dopp Meas: Beacon 2 Estimation Errors with 3σ Boundaries

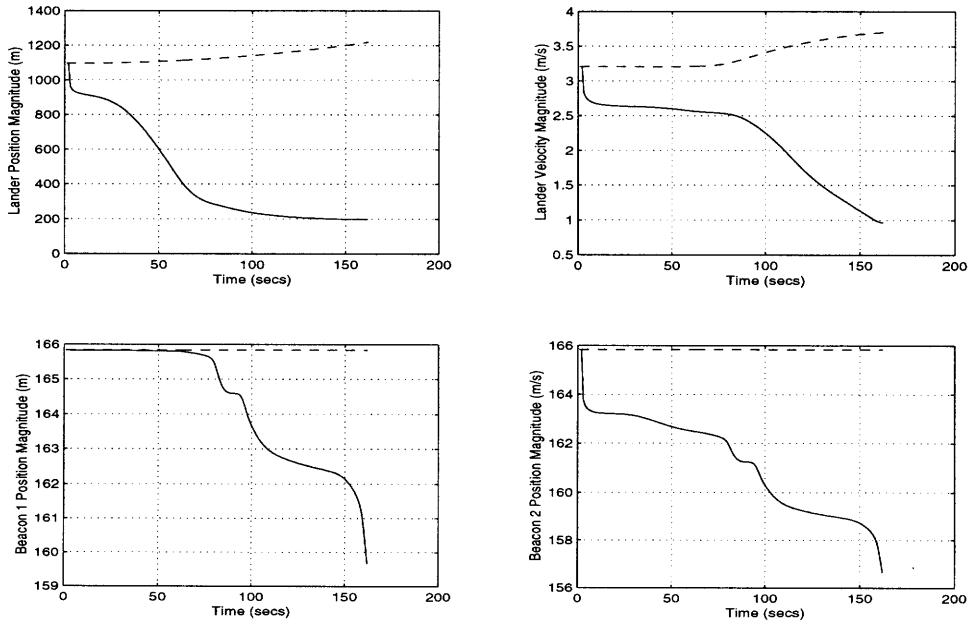

Figure 4.65: All Beac Dopp Meas: Standard Deviation Magnitudes

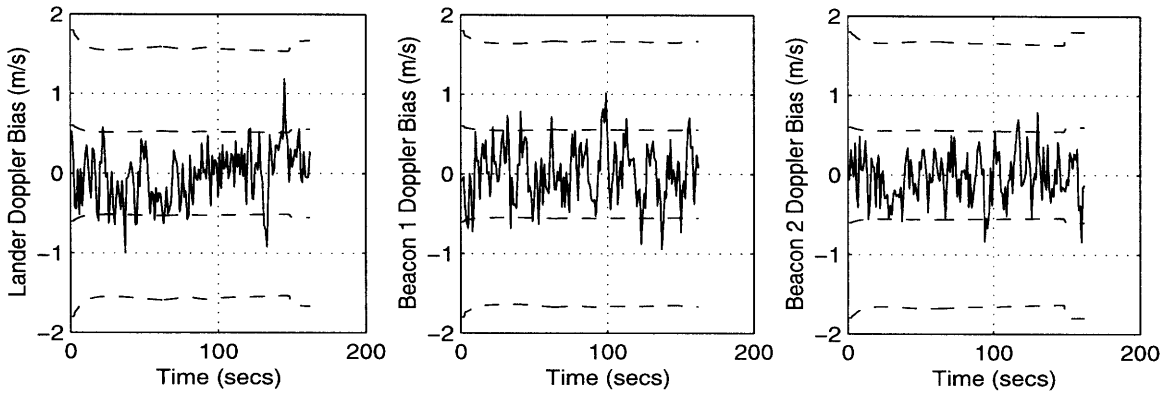

Figure 4.66: All Beac Dopp Meas: Range Bias Estimation Errors with 1σ/3σ Bounds

Table 4.4 lists the final lander state standard deviations of the no measurement case and the three beacon Doppler measurement cases. The best results, i.e. the smallest standard deviations, belong to the measurement profile that uses both beacons. Furthermore, the results of all three measurement cases imply that the filter is the most effective on the lander position and velocity in the Y direction. This suggests that the motion of the range vectors with both beacons is predominantly in this axis. Finally, comparing these results to the satellite Doppler results in Table 4.2 on page 89, Doppler measurement filtering appears to be much more effective when using surface beacons instead of satellites.

Lander State Std. Dev.	Measurement Profile (Doppler Measurements)			
	No Meas	Beacon 1	Beacon 2	All Beacs
X Position	721.3008 m	184.3826 m	542.6147 m	93.3485 m
Y Position	692.3987 m	134.1667 m	156.7710 m	68.8376 m
Z Position	697.0675 m	498.6272 m	230.3988 m	159.6152 m
X Velocity	2.2852 m/s	0.8717 m/s	2.1595 m/s	0.7965 m/s
Y Velocity	1.8635 m/s	0.4365 m/s	1.0717 m/s	0.3271 m/s
Z Velocity	2.2351 m/s	2.1876 m/s	0.6811 m/s	0.4302 m/s

Table 4.4: Final Lander Standard Deviations for Doppler Measurement Profiles

4.3.6 Altitude Measurement Case

Only one measurement profile is used to analyze the performance of the filter with altitude measurements. This is because the radar altimeter will only take measurements with the planetary surface directly below the lander. In contrast, many measurement profiles can be used to analyze range and Doppler filtering, since the measurements are taken with satellites and beacons and the number of satellites and beacons, as well as their initial state values, can be chosen with much freedom and discretion.

The results of the altitude measurement profile are presented with the help of three figures. Figure 4.67 displays the estimation errors with 3σ bounds of the lander states while Figure 4.68 shows the magnitudes of the lander position and velocity standard deviations. The last plots, in Figure 4.69 demonstrate the estimation errors with 1σ and 3σ bounds of the bias states relevant to the altimeter: the scalar altimeter bias state and terrain first-order Markov process (FOMP) bias state, and the three-dimensional terrain plane misalignment states. Finally, Table 4.5 on page 114 compares the final lander standard deviations of the no measurement profile and this altitude measurement profile. Also, it is important to note that the radar altimeter cannot take measurements until the lander is at a set maximum height above the surface of Mars and the lander reaches this height (20,000 metres) at the 130 second time step.

The lander estimation errors and standard deviations in Figure 4.67 show immediate responses to the filter after 130 seconds. However, these responses are mostly confined to the X and Y axis states. As was discussed previously in this chapter and can also be visualized in Figure 4.42, the altitude vector of the lander is predominantly in the X direction throughout the simulation. A component in the Y direction also develops as the trajectory develops. Therefore, the discrimination with measurement vector components that takes place in range filtering can also be found in altitude filtering. This is quite reasonable

since, in basic terms, the altitude measurement behaves like a one-way range measurement to the planet surface directly below the lander. As was also the case with the range measurement results, the lander estimation errors fall well within the 3σ bounds. In addition, the filter appears to influence both the position and velocity states.

Some of these characteristics are also reflected in Figure 4.68, which plots the lander position and velocity standard deviation magnitudes. The immediate lander state responses to the filter are well illustrated, as is the fact that the filter affects both the lander position and velocity estimates. Furthermore, these plots show no sharp increases caused by the accelerometer bias, despite the fact that the filter is only effective for X axis states. However, it is known that the velocity standard deviations are most vulnerable to accelerometer bias effects in the X and Z directions. Thus, reducing the velocity error standard deviation in the X axis, via altitude measurement filtering, is good enough to counter these effects.

The bias state estimation errors in Figure 4.69 all display very distinctive results. This is because the bias states all have different dynamics models. The scalar altimeter bias is modeled as first-order Markov process with a fixed time constant. Its estimation error results are bounded quite well, with transients almost always within 1σ. The terrain FOMP bias is also a scalar modeled as a first order Markov process but it uses a time constant dependent on planetary angular momentum, which causes estimation error transients to decrease in time. In turn, these decreasing transients make the estimation error susceptible to biases, which is accounted for in the standard deviation. The three-dimensional terrain plane misalignment is modeled as a constant and has relatively small measurement sensitivities in the Kalman gain matrix. Likewise, its estimation errors and standard deviations show very little reaction to the filter.

Table 4.5, which compares the final lander state standard deviations of the no measurement case and the altitude measurement case, makes it very clear that the filter is most effective on the position and velocity in the X axis. In addition, these results are similar to the Satellite 1 range results (which also show predominant minimization of the standard deviations in the X direction) in Table 4.1 on page 77. This is especially favourable for altitude filtering, since measurements are only processed in the filter for the last 33 time steps.

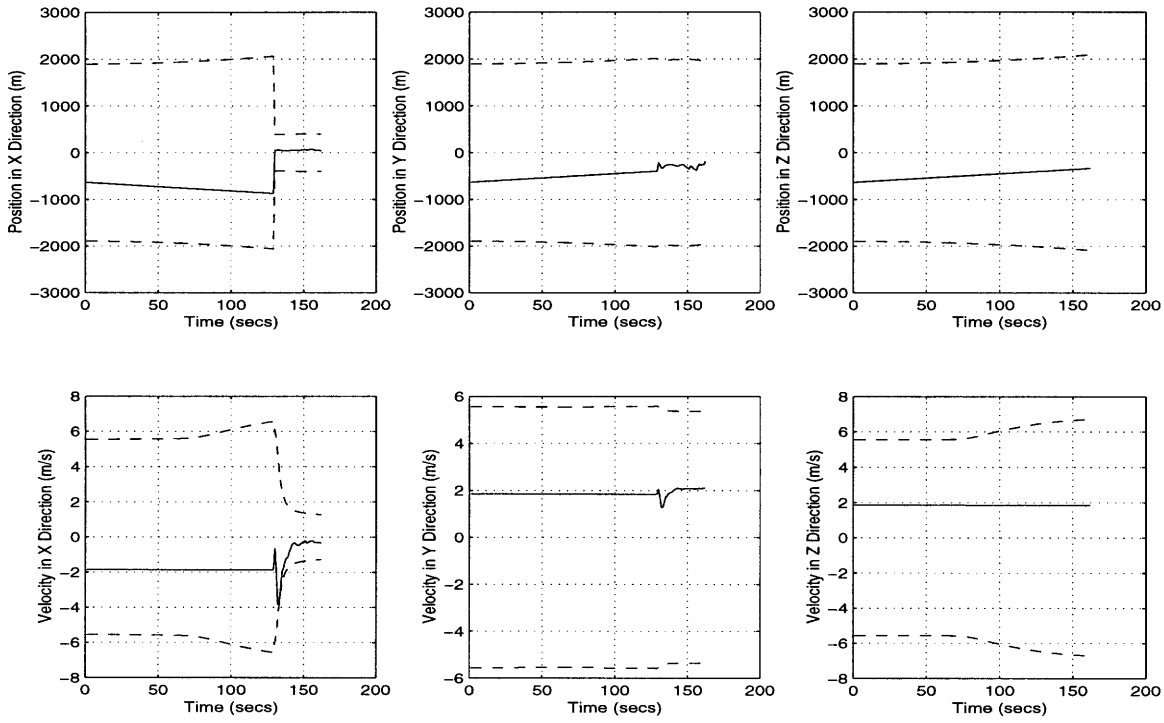

Figure 4.67: Altitude Meas: Lander Estimation Errors with 3σ Boundaries

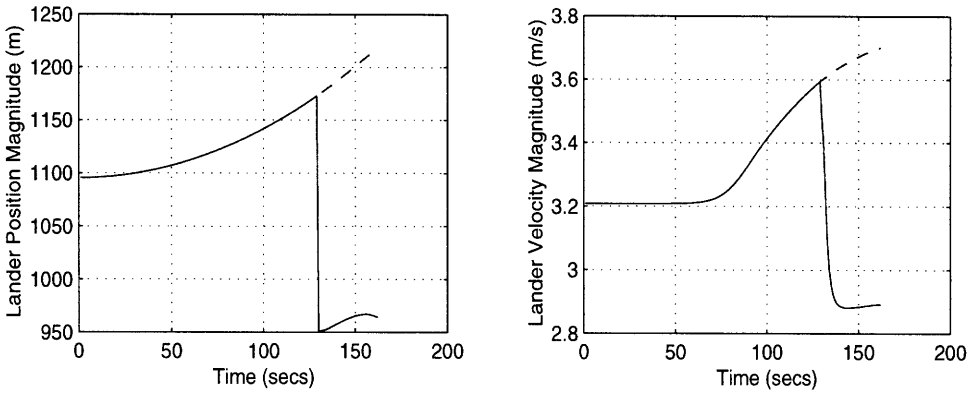

Figure 4.68: Altitude Meas: Lander Standard Deviation Magnitudes

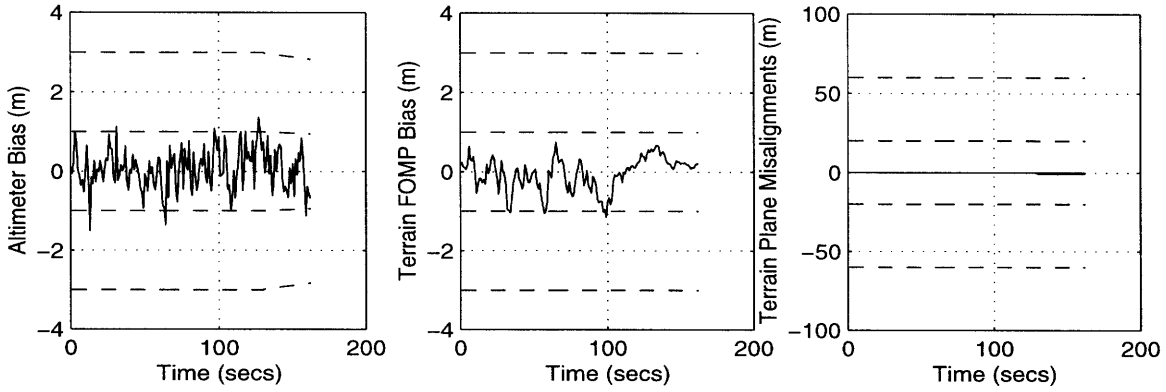

Figure 4.69: Altitude Meas: Altimeter Bias Estimation Errors with 1σ/3σ Bounds

Lander State Std. Dev.	Measurement Profile	
	No Meas	Altitude Meas
X Position	721.3008 m	132.9006 m
Y Position	692.3987 m	653.0039 m
Z Position	697.0675 m	697.0619 m
X Velocity	2.2852 m/s	0.4250 m/s
Y Velocity	1.8635 m/s	1.7845 m/s
Z Velocity	2.2351 m/s	2.2351 m/s

Table 4.5: Final Lander Standard Deviations for Altitude Measurement Profile

4.3.7 Surface Velocity Measurement Case

EKF performance analysis with surface velocity measurements is also presented for one measurement profile. This is because the surface radar velocimeter, like the radar altimeter, only takes measurements relative to the planetary surface. Performance results are shown in Figures 4.70 to 4.72. Estimation errors with 3σ bounds of the lander states are portrayed in Figure 4.70 while the lander standard deviation magnitudes are illustrated in Figure 4.71. Figure 4.72 shows estimation errors with 1σ and 3σ bounds of bias states relevant to the velocimeter: the three dimensional velocimeter bias and velocimeter misalignment bias. A comparison of the final lander standard deviations of the no measurement profile and this surface velocity measurement profile is presented in Table 4.6. In addition, like the altimeter, the lander must be within a maximum altitude for the velocimeter to be able to take measurements. This altitude is also set to 20,000 metres and is reached at 130 seconds.

Figure 4.70 demonstrates that the lander velocity estimates and standard deviations respond very well to surface velocity measurement filtering in all directions. In fact, the filter seems to have equal effect on the velocity states in all three directions. Referring to the surface velocity measurement filtering models in Section 2.5.4, it is seen that the measurement sensitivity ($\underline{H}_k$) model weights all velocity states in each axis equally, regardless of the lander position or velocity in relation to the planet surface. This is quite different from the other measurement types, which weight the lander state sensitivities in correspondence to the components of a range or delta-range vector. Also, it is clear from the figure that the filter has much more effect on the lander velocity states than on the lander position states.

Some of these effects are further illustrated in Figure 4.71, which displays the magnitudes of the lander position and velocity error standard deviations. The lander velocity error magnitude is greatly and immediately reduced in time, while the position magnitude shows only meager effects in comparison. In addition, since the filter controls the velocity errors such a great deal, the accelerometer bias does not have a chance to increase the velocity error standard deviations in its usual fashion.

Figure 4.72 displays the estimation errors of the velocimeter bias and velocimeter misalignment bias in all three dimensions. Both biases are modeled as first-order Markov processes with fixed time constants. Indeed, the resulting estimation errors of both biases in each direction are all well bounded. Furthermore, the standard deviations of the velocimeter bias shows slight decreases in time after 130 seconds, while the standard deviations of the misalignment bias reflect initial decreases followed by sharp increases. These increases are largest in the X and Z directions, which suggests that the filter is tying the accelerometer bias increases to the misalignment bias standard deviations as well as the lander velocity standard deviations.

The final lander state standard deviations of the no measurement case and this surface velocity measurement case are compared in Table 4.6. This table illustrates that filtering with surface velocity measurements will influence the lander velocity states very favourably. In addition, this influence is distributed almost evenly among the velocity states in each direction. On the other hand the lander position states are barely affected at all, thus validating that surface velocity filtering cannot be relied upon to improve the knowledge in these states.

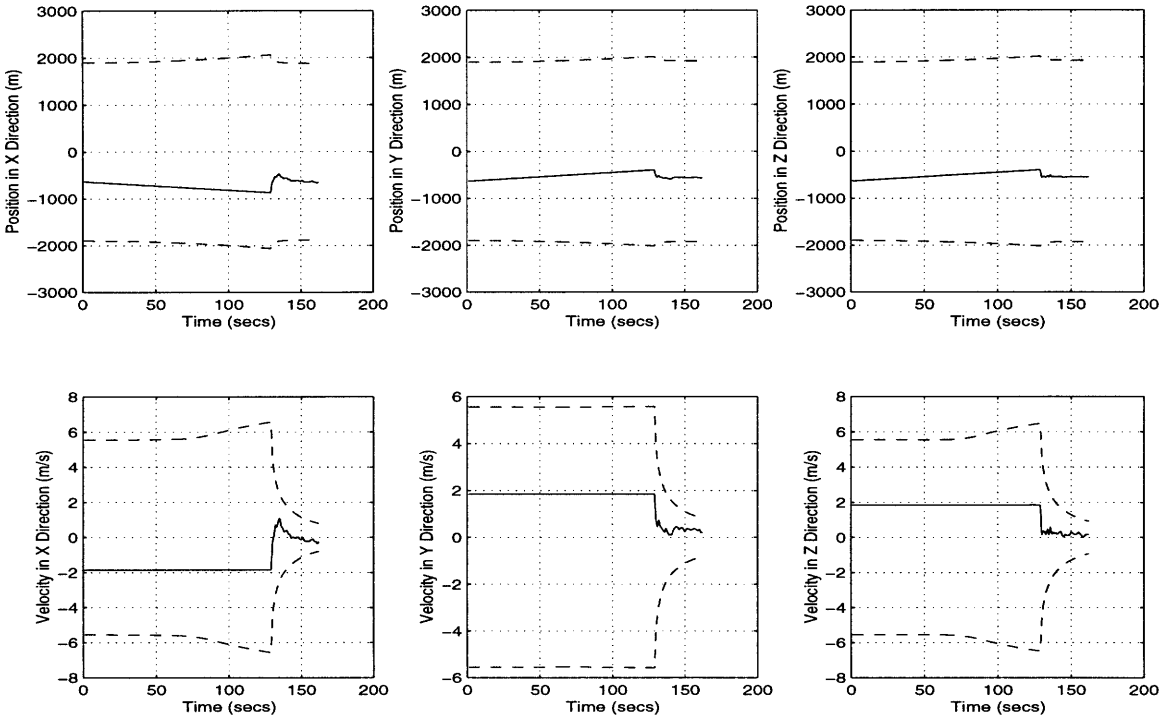

Figure 4.70: Surface Vel Meas: Lander Estimation Errors with 3σ Boundaries

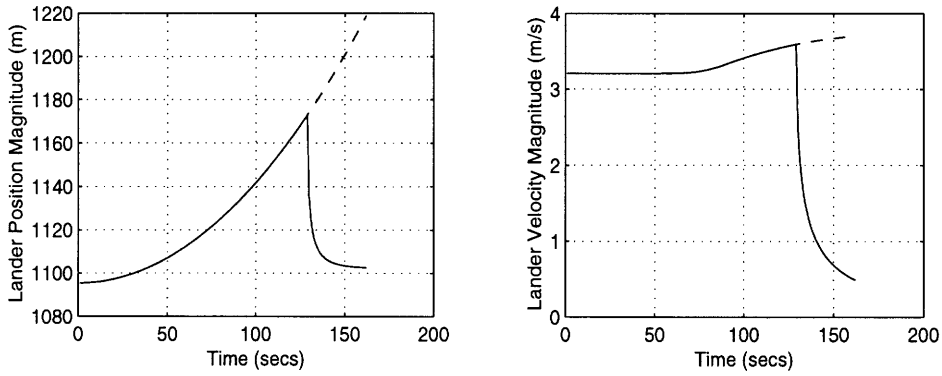

Figure 4.71: Surface Vel Meas: Lander Standard Deviation Magnitudes

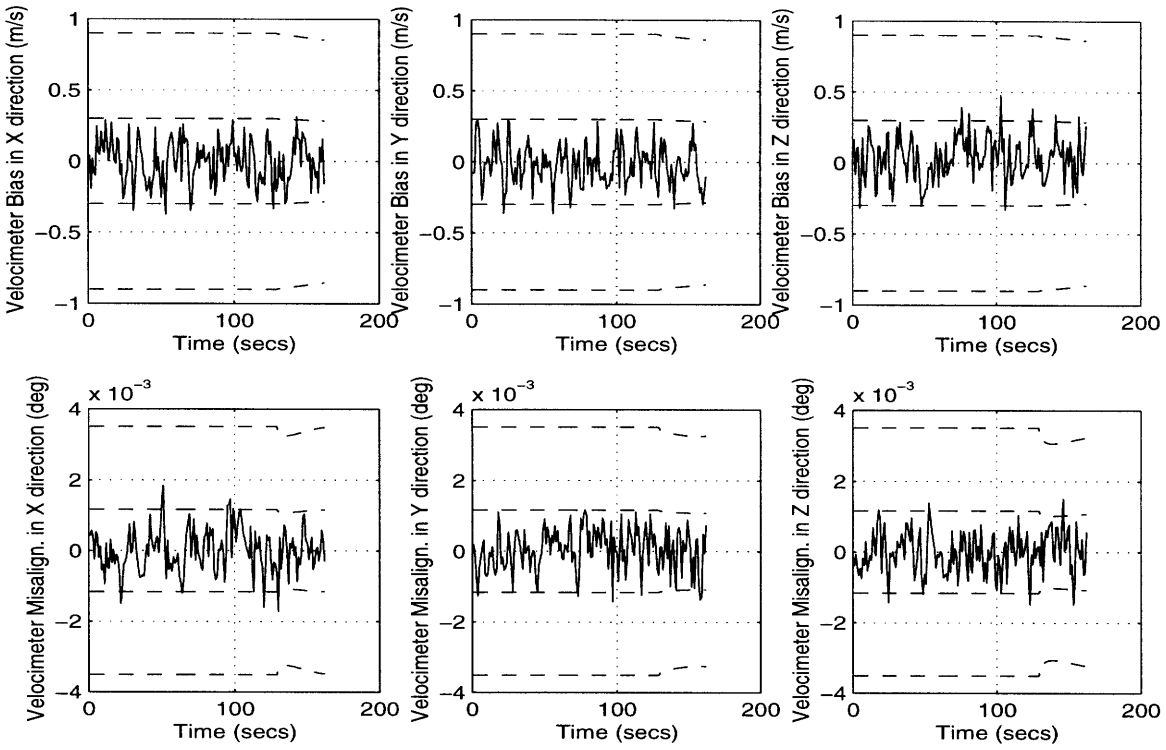

Figure 4.72: Surface Vel Meas: Velocimeter Bias Est. Errors with 1σ/3σ Bounds

Lander State Std. Dev.	Measurement Profile	
	No Meas	Surf Vel Meas
X Position	721.3008 m	625.9934 m
Y Position	692.3987 m	640.6060 m
Z Position	697.0675 m	643.0497 m
X Velocity	2.2852 m/s	0.2653 m/s
Y Velocity	1.8635 m/s	0.2733 m/s
Z Velocity	2.2351 m/s	0.3086 m/s

Table 4.6: Final Lander Standard Deviations for Surface Vel. Measurement Profile

4.4 Measurement Type Sequencing

After all measurement types of the simulation have been individually evaluated, it is useful to examine the aggregate case that uses a combination of measurement types to attain the best overall results. However, the order in which measurements are sequentially processed in an extended Kalman filter algorithm can be a factor in reducing estimation errors. Thus, the sequence of measurement types in this simulation was examined in order to evaluate this effect.

This sequence examination is based on two key assumptions. First, it is assumed that the best results are achieved when all measurement types are incorporated, where the best results are defined as the lowest final state standard deviations with appropriate (i.e. well bounded) state responses. It is further assumed that only lander position and velocity states are important, so other states are not considered. Second, range and Doppler measurements will be available with all three satellites and both surface beacons at all time steps.

4.4.1 Final Results

After running a series of simulations using various measurement sequences, the corresponding results do not appear to differ to any significant degree. Thus, the sequence in which measurements are processed in this filter is irrelevant.

To further illustrate this, the results of the final two test simulations are presented. The measurement sequences in these simulations are designed to test the order of the surface-based measurements (altitude, surface velocity) against the satellite/surface beacon-based measurements (satellite range, satellite Doppler, beacon range, beacon Doppler) and incorporate all measurement types.

These measurement sequences are as follows:

1. Altitude, surface velocity, Satellite 1, Satellite 2, and Satellite 3 range, Satellite 1, Satellite 2, and Satellite 3 Doppler, Beacon 1 and Beacon 2 range, Beacon 1 and Beacon 2 Doppler,
2. Satellite 1, Satellite 2, and Satellite 3 range, Satellite 1, Satellite 2, and Satellite 3 Doppler, Beacon 1 and Beacon 2 range, Beacon 1 and Beacon 2 Doppler, altitude, surface velocity,

The final standard deviations of the lander position and velocity states from the two simulations are presented in Table 4.7 below:

Final Lander Std. Dev.	**Measurement Profiles**	
	Surface, Satellite/Beacon	**Satellite/Beacon, Surface**
X Position	18.9152 m	18.9253 m
Y Position	34.4513 m	34.4593 m
Z Position	97.6397 m	98.5855 m
X Velocity	0.0673 m/s	0.0672 m/s
Y Velocity	0.0682 m/s	0.0682 m/s
Z Velocity	0.1373 m/s	0.1374 m/s
Magnitudes		
Position σ	105.2529 m	106.1354 m
Velocity σ	0.1675 m/s	0.1674 m/s

Table 4.7: Satellite/Beacon and Surface Measurement Sequencing Simulation Results

Indeed, these results show very little difference in the lander position and velocity standard deviations. However, these *are* the final two test simulations, and the position uncertainties of the first simulation are smallest. Thus, the corresponding sequence (altitude measurements, satellite/beacon measurements) is selected as the 'optimal' sequence.

In addition, the lander state estimation errors of this 'optimal' simulation are well bounded. These estimation errors with 3σ bounds are shown below.

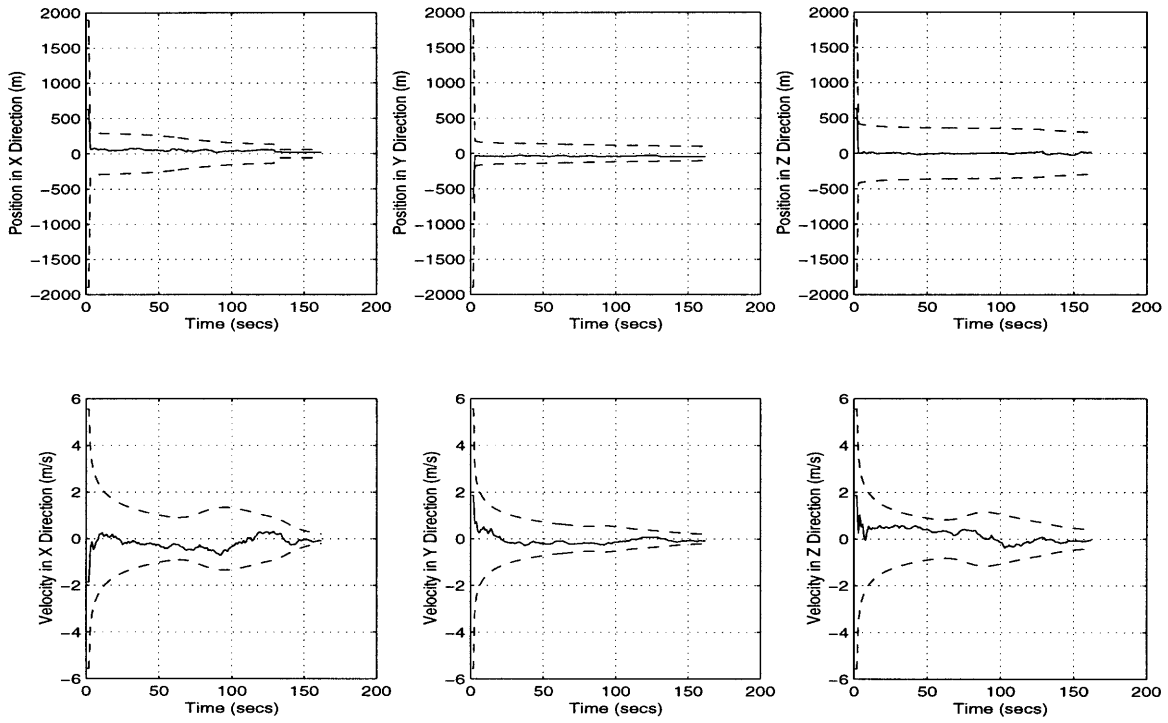

Figure 4.73: Lander Estimation Errors for Final Measurement Sequence Simulation

Chapter 5

Conclusion

The goal of this thesis was to present a navigation system design for Mars entry. This system uses a series of on-board sensors to take external measurements that are processed in an extended Kalman filter to estimate state variables. These variables include all relevant positions and velocities as well as sensor biases states. Simulation results of the states are presented to analyze the performance of the filter using individual measurement types. In addition, the sequence that the measurements are processed in the filter was considered and found to be irrelevant in the final design.

5.1 Summary of Results

In general, the simulation performance results in Chapter 4 illustrate that the filter in this design is most effective on the error estimates and standard deviations of the lander states. The correct lander state standard deviations are always significantly reduced and the corresponding error estimates are well behaved. However, these error estimates (especially those of the lander position states) can contain noticeable biases. In comparison, the error estimates and standard deviations of the bias states, as well as the satellite and beacon states, display limited effects from the filter in all cases.

Furthermore, the lander state results of each individual case show that the position and velocity estimate responses in each direction to the filter are dependent on the measurements processed in that case. For instance, filtering the satellite range measurements will predominantly affect the lander position estimates in the directions of the largest range

vector components. The lander state responses to the filter using each measurement type individually are presented in Table 5.1.

Measurement Type processed in EKF	State Estimate Responses to EKF	
	Lander Position Responses	**Lander Velocity Responses**
Satellite Range	greatest in directions of largest range vector components	minimal
Satellite Doppler	minimal	greatest in directions of largest range vector components
Beacon Range	greatest in directions of largest range vector components	greatest in directions of largest range vector components
Beacon Doppler	greatest in directions of largest delta-range vector components	greatest in directions of largest range vector components
Altitude	greatest in directions of largest altitude vector components	greatest in directions of largest altitude vector components
Surface Velocity	minimal	even in all directions

Table 5.1: Lander State Responses to EKF using Individual Measurement Types

Furthermore, if the filter is processing two or more of these measurement types, the corresponding state responses are cumulative. For example, filtering satellite range and Doppler measurements will predominantly affect the lander position *and* velocity states in the directions of the largest range vector components. Of course, if all available measurements are processed, then the lander states in all directions are well accounted for and the most favourable results are achieved.

Measurement filtering is also dependent the position of the sensor targets (satellite, beacon, or planet surface) with respect to the lander module in a chosen coordinate system. For instance, while altitude and surface velocity filtering is very effective in this simulation, the corresponding sensors are unable to take measurements until there are 30

seconds left in a 162 second time frame. Likewise, the positions of the satellites and beacons play a role in the impact of range and Doppler measurement filtering. This is especially true with the beacons, which cannot be too far away from the lander trajectory to take range and Doppler measurements. Although they are not bounded on the surface of Mars, the satellites also must be positioned reasonably close for the respective measurement filtering to be effective. In addition, in processing satellite and beacon measurements, the range vectors must collectively account for all directions to ensure that the filter will be effective in all directions. Thus, if satellites and beacons are to be considered for future Mars missions, it would be important to have a number of them in orbit or on the surface to take range and Doppler measurements that will account for all directions at all times.

Finally, it was found that the order in which the measurements are processed does not affect the standard deviations of the state to any great extent. However, the measurement sequence that does yield the most optimal results is: altitude measurement, surface velocity measurement, all satellite range measurements, all satellite Doppler measurements, all beacon range measurements, and all beacon Doppler measurements. Filtering the measurements in this sequence will bring the final lander position standard deviation magnitude from 1218.85 m to 105.25 m, for a reduction of 91.36%, and the final lander velocity standard deviation magnitude from 3.700 m/s to 0.168 m/s, a reduction of 95.47%.

5.2 Suggestions for Future Analysis

There are a numerous paths that one can take to continue this analysis. One possibility would be to apply stability and failure robustness techniques to this filter. The former could be a very important area of study since, although the results in this thesis appear to be stable, the basic extended Kalman filter algorithm does not guarantee stability for sys-

tems with large perturbations [8]. Likewise, failure robustness is important to ensure that the filter can still function properly if one or more sensors cannot deliver a proper measurement, so studies using fewer measurements and/or measurement types could provide information on failure tolerance.

In addition, further analysis in this particular navigation system can be taken by making modifications to the simulation. This can include adding more satellites and beacons to the simulation to take range and Doppler measurements with, in order to determine if the use of too many satellites or beacons is redundant. Another possibility would be to add new measurements from different sensors, such as a stellar tracker. A final suggestion is to compare the results of simulations with measurements processed at various frequencies.

References

[1] "Advanced Tactical Inertial Measurement Unit." *Air Force Research Laboratory Munitions Directorate.* <http://www.wlmn.eglin.af.mil/public/mnag/atimu.html>.

[2] Arabelos, D. "On the possibility to estimate ocean bottom topography from marine gravity and satellite altimeter data: An experiment in the central Mediterranean." <http://sg.topo.auth.gr/~arab/depths-exp.html>.

[3] Battin, R.H. *An Introduction to the Mathematics and Methods of Astrodynamics.* American Institute of Aeronautics and Astronautics, Inc., New York, NY, 1987.

[4] Brown, R.G. and P.Y.C. Huang. *Introduction to Random Signals and Applied Kalman Filtering.* John Wiley & Sons, Inc., New York, NY, 1997.

[5] D'Souza, C.N. Private Communications, Dec 1997-May 1998.

[6] Fuhry, D.P. *A Design Study of Onboard Navigation and Guidance During Aerocapture at Mars.* S.M. Thesis, Department of Aeronautics and Astronautics, MIT, May 1988.

[7] Gelb, A. (Ed.) *Applied Optimal Estimation.* The MIT Press, Cambridge, MA, 1996.

[8] Grunberg, D.B. and M. Athans. "Guaranteed Properties of the Extended Kalman Filter." Cambridge, MA, December 1987.

[9] Hechler, M. and M. Lauer. "Approach Navigation for the Delivery of Small Landers to the Surface of Mars." *1992 AIAA/AAS Astrodynamics Conference* (at Hilton Head, SC), pgs 456-464. American Institute of Aeronautics and Astronautics, 1992.

[10] "Japanese and DSN Orbit Prediction Capability for the VSOP Mission." *Jet Propulsion Laboratory Space Very Long Baseline Interferometry Project.* <http://sgra.jpl.nasa.gov/mosaic_v0.0/JPL_Project_dir/Library_dir/memo/y91/91_72.txt>.

[11] Lear, W. *Navigation at Mars Using Ground Transponders.* National Aeronautics and Space Administration, Lyndon B. Johnson Space Center, Houstion, TX, July 1989.

[12] *Linear Covariance Tool Users' Guide and Description Document.* Version 3.1. © The Charles Stark Draper Laboratory, Cambridge, MA, 1997.

[13] Malin, M.C., Principal Investigator. "Observations of the "Face on Mars" and similar features by the Mars Global Surveyor Orbiter Camera." <http://amadeo.uni-muenster.de/~sohl/solar/facedisc.htm>. Malin Space Science Systems, Inc., 1995.

[14] Melvin, P.J. "A Kalman Filter for Orbit Determination with Applications to GPS and Stellar Navigation." volume 93, part I of *Spaceflight Mechanics 1996*, pgs 719-738. American Astronautical Society, San Diego, CA, 1996.

[15] Puri, V. *Tightly Coupled GPS-Gyro Integration For Spacecraft Attitude Determination.* S.M. Thesis, Department of Aeronautics and Astronautics, MIT, June 1997.

[16] Spencer, D. A. and R.D. Braun. "Mars Pathfinder Entry-Trajectory Design and Dispersion Analysis." *Journal of Spacecraft and Rockets*, vol 33, no. 5, October 1996, pgs 670-676.

[17] Thurman, S.W. and J.A. Estefan. "Mars Approach Navigation Using Doppler and Range Measurements to Surface Beacons and Orbiting Spacecrafts." *Spaceflight Mechanics 1991, Proceedings of the 1st Annual AAS-AIAA Spaceflight Mechanics Meetings*, pgs 227-247, 1991.

[18] "TOPEX/POSEIDON Merged Geophysical Data Record." *Jet Propulsion Laboratory Physical Oceanograhy DAAC Guide Document Catalog.* <http://podaac.jpl.nasa.gov:2031/dataset_docs/topex_mgdr.html>.